UC San Diego
UC San Diego Electronic Theses and Dissertations

## Title

Surface Transformations of Metal Oxide and Metal Sulfide Nanoparticles: Surface Adsorption, Surface Reactions and Surface Oxidation

## Permalink

https://escholarship.org/uc/item/3g21b5sh

## Author

Wu, Haibin

## Publication Date

2020

Peer reviewed|Thesis/dissertation

eScholarship.org Powered by the California Digital Library
University of California

UNIVERSITY OF CALIFORNIA SAN DIEGO

# Surface Transformations of Metal Oxide and Metal Sulfide Nanoparticles: Surface Adsorption, Surface Reactions and Surface Oxidation

A dissertation submitted in partial satisfaction of the requirements for the degree Doctor of Philosophy

in

Chemistry

by

Haibin Wu

Committee in charge:

Professor Vicki Grassian, Chair
Professor Jessie Jokerst
Professor Andrew Kummel
Professor Kim Prather
Professor Alina Schimpf
Professor Donald Sirbuly

2020

Copyright (or ©)

Haibin Wu, 2020

All rights reserved.

The dissertation of Haibin Wu is approved, and it is acceptable in quality and form for publication on microfilm and electronically:

_____

_____

_____

_____

_____

_____

Chair

University of California San Diego

2020

# DEDICATION

This dissertation is dedicated to my beloved family and friends who are always encouraging and supporting me in my life.

TABLE OF CONTENTS

Signature Page ..... iii

Dedication ..... iv

Table of Contents ..... v

List of Figures ..... xi

List of Tables ..... xvii

Acknowledgements ..... xviii

Vita ..... xxi

Abstract of the Dissertation ..... xxii

Chapter 1 Introduction ..... 1

1.1 Nanoparticles ..... 1

1.2 Metal Oxide and Metal Sulfide NPs ..... 3

1.2.1 Titanium Dioxide ..... 3

1.2.2 Copper Sulfide ..... 4

1.3 Surface Chemistry and Transformation ..... 5

1.3.1 Surface Ligand Reactions ..... 6

1.3.2 Reactive Oxygen Species (ROS) ..... 8

1.4 Dissertation Motivation and Objectives ..... 10

1.5 Acknowledgements ..... 12

1.6 References ..... 13

Chapter 2 Experimental Methods and Techniques ..... 21

2.1. ATR–FTIR Spectroscopy ..... 21

2.2. Two-Dimensional Correlation Spectroscopy ..... 25

2.3. Quartz Crystal Microbalance with Dissipation Monitoring ..... 26

2.4. Electron Microscopy ..... 28

2.4.1 Transmission Electron Microscopy ..... 29

2.4.2 Scanning Electron Microscopy ..... 29

2.5.X-ray Photoelectron Spectroscopy ..... 30

2.6. Nanoparticle Characterization ..... 30

2.6.1 Powder X-ray Diffraction Spectrometry ..... 31

2.6.2. Specific Surface Area Analysis ..... 31

2.7. Acknowledgements ..... 32

2.8 References ..... 33

Chapter 3 Displacement Reactions Between Environmentally and Biologically Relevant Ligands on $TiO_2$ Nanoparticles: Insights into the Aging of Nanoparticles in the Environment ..... 36

3.1 Abstract ..... 36

3.2 Introduction ..... 37

3.3 Experimental Methods ..... 39

3.3.1 ATR–FTIR Spectroscopy ..... 39

3.3.2 Analysis of Two-Dimensional Correlation Spectroscopy ..... 40

3.3.3 Quartz Crystal Microbalance with Dissipation (QCM-D) ..... 41

3.3.4 Sedimentation and Dynamic Light Scattering ..... 42

3.4 Results and Discussion ..... 43

3.4.1 Adsorption of AA, CA, HA and BSA on $TiO_2$ NP Surfaces ..... 43

3.4.2 Displacement Reactions ..... 52

3.4.3 Sedimentation and Agglomeration. ..... 59

3.5 Conclusions ..... 60

3.6 Acknowledgements ..... 61

3.7 References ..... 62

Chapter 4 Mechanistic study of oil adsorption onto PVP-coated magnetic nanoparticles: An integrated experimental and molecular dynamics study to inform remediation ..... 72

4.1 Abstract ..... 72

4.2 Introduction ..... 72

4.3 Methods ..... 73

4.3.1 Experimental. ..... 73

4.3.2 Molecular models and simulations ..... 76

4.4 Results and Discussions ..... 77

4.5 References ..... 87

Chapter 5 Impact of Surface Adsorbed Biologically and Environmentally Relevant Ligands on $TiO_2$ Nanoparticle Reactivity ..... 92

5.1 Abstract ..... 92

5.2 Introduction ..... 93

5.3 Experimental Methods ..... 95

5.3.1 Materials ..... 96

5.3.2 ATR–FTIR Spectroscopy ..... 96

5.3.3 Batch Reactor Photochemical Experiments ..... 97

5.3.4 Mass Spectrometry Analyses of Photooxidation Products ..... 97

5.4 Results and Discussion ..... 97

5.4.1 ATR–FTIR Spectroscopy of BSA and FA Adsorption on TiO2 NPs ..... 98

5.4.2 ATR–FTIR Spectra Monitoring Photochemical Processes on $TiO_2$ NPs ..... 100

5.4.3 ATR–FTIR Spectra Monitoring Photochemical Processes of Coating Molecules on $TiO_2$ NPs ..... 101

5.4.4 ATR–FTIR Spectra Monitoring Photochemical Processes of BA on $TiO_2$ NPs. 103

5.5 Conclusions ..... 106

5.6 Acknowledgements ..... 107

5.7 References ..... 109

Chapter 6 CuS Nanoparticles in Humid Environments: Adsorbed Water Enhances the Transformation of CuS to $CuSO_4$ ..... 117

6.1 Abstract ..... 117

6.2 Introduction ..... 117

6.3 Experimental Details ..... 119

6.3.1 Synthesis of Covellite Nanoparticles ..... 119

6.3.2 CuS Nanoparticle Characterization ..... 119

6.3.3 AFM-PTIR Spectroscopy ..... 120

6.3.4 X-Ray Photoelectron Spectroscopy ..... 120

6.3.5 ATR–FTIR Spectroscopy ..... 120

6.4 Results and Discussion ..... 121

6.4.1 Characterization of CuS Nanoparticles ..... 121

6.4.2 ATR–FTIR Spectroscopy ..... 122

6.4.3 X-Ray Photoelectron Spectroscopy in Cu 2p and S 2p Regions ..... 125

6.4.4 Imaging Techniques: Atomic Force Microscopy Coupled to Infrared Spectroscopy and High-Resolution Transmission Electron Microscopy ..... 128

6.4.5 Surface Transformations and Oxidation of CuS in Humid Environments ..... 130

6.5 Conclusions ..... 132

6.6 Acknowledgements ..... 133

6.7 References ..... 134

Chapter 7 Conclusions and Future Directions ..... 140

7.1 Chapter 3 Summary ..... 141

7.2 Chapter 4 Summary ..... 142

7.3 Chapter 5 Summary ..... 143

7.4 Chapter 6 Summary ..... 144

7.5 Future Directions ..... 145

Appendix A Supporting Information for "Displacement Reactions Between Environmentally and Biologically Relevant Ligands on $TiO_2$ Nanoparticles: Insights into the Aging of Nanoparticles in the Environment" ..... 147

A.1 Experimental Details and Additional Experimental Data ..... 147

A.2 References ..... 152

A.3 Acknowledgements ..... 152

Appendix B Supporting Information for "Mechanistic study of oil adsorption onto PVP-coated magnetic nanoparticles: An integrated experimental and molecular dynamics study to inform remediation" ..... 153

B.1 Additional Experimental Data ..... 153

B.2 Acknowledgements ..... 153

Appendix C Supporting Information for "Surface Adsorbed Biologically and Environmentally Relevant Ligands on $TiO_2$ Nanoparticles Transformations: The Influence on Reactivity of Nanoparticles" ..... 154

C.1 Additional Experimental Data ..... 154

C.2 Acknowledgements ..... 154

LIST OF FIGURES

Figure 1.1 Physicochemical Processes occurring at the surface of an inorganic nanoparticle..... 2

Figure 1.2 Possible binding modes of a carboxylic acid to a $TiO_2$ surface.. ..... 6

Figure 1.3 Illustration of ROS generation mechanisms, photoinduced mechanism (left) and chemical redox mechanism (right)..... 9

Figure 2.1 Electromagnetic wave reflection depicting the evanescent wave near the interface in an internal reflection element. ..... 21

Figure 2.2 Schematic of various ATR-FTIR experimental setups. ..... 23

Figure 2.3 Schematic of the ATR-FTIR and gas flow experimental setup used for CuS oxidation. ..... 24

Figure 2.4 (a) common design for a quartz crystal gold electrode for QCM, (b) a diagram depicts frequency change with mass gain on the electrode surface, (c) Frequency and amplitudes for quartz oscillations with different types of adsorbates..... 27

Figure 2.5 (a) cross-sectional SEM image for a $TiO_2$ NP film, (b) FIB-SEM image of a $TiO_2$ NP film..... 31

Figure 3.1 ATR–FTIR spectra of target species adsorbed onto $TiO_2$ and in solution phases. (a) Spectra of adsorbed 10 mM and in solution 100 mM AA; (b) spectra of adsorbed 10 mM and in solution 100 mM CA; (c) spectra of adsorbed 0.05 g/L and in solution 1 g/L HA; (d) spectra of adsorbed 1 g/L on and in solution 10 g/L BSA. The adsorption spectra shown were collected at 5 min (black), 30 min (red), 60 min (green), 90 (blue), 120 min (magenta). ..... 44

Figure 3.2 The adsorption and desorption processes of (a) 10 mM AA, (b) 10 mM CA, (c) 0.05 g/L HA and (d) 1 g/L BSA. The intensity was normalized using the absorbance at 1385 $cm^{-1}$ for AA, 1570 $cm^{-1}$ for CA, 1570 $cm^{-1}$ for HA, and 1545 $cm^{-1}$ for BSA, respectively. ..... 46

Figure 3.3 Shifts in frequency and dissipation, normalized by overtone number, for the adsorption of ascorbic acid (a), citric acid (b), humic acid (c) and bovine serum albumin (d) onto a $TiO_2$ coated surface with QCM–D. Blue and red lines represents changes in frequency and dissipation, respectively. Data are shown for overtones 5, 7, 9, and 11 in a color gradient, in which the darker colors are for smaller overtones. ..... 48

Figure 3.4 ATR-FTIR of the displacement reactions of AA-(a), CA-(b), and BSA-(c) pre-coated $TiO_2$ NPs by HA. The initial coating spectra are on the left, the time dependent displacement spectra are in the middle, and the difference spectra are on the right. The displacement spectra were collected at 5 min (black), 30 min (red), 60 min (green), 90 (blue), 120 min (magenta). The difference spectra were obtained by subtracting the initial spectra from displacement spectra... 51

Figure 3.5 A schematic representation of displacement reactions and co-adsorption by HA on pre-coated $TiO_2$ surfaces with AA (a), CA (b), and BSA (c), respectively. HA is represented here as a macromolecular structure..... 53

Figure 3.6 Synchronous (left) and asynchronous (right) 2D correlation maps following introduction of HA to a $TiO_2$ surface covered with (a) AA, (b) CA, and (c) BSA. ..... 56

Figure 3.7 The effects of displacement reactions on sedimentation behavior of $TiO_2$NPs. The displacement reactions on the AA– (a), CA– (b) coated $TiO_2$ NPs with HA make the particles more stable (top) and smaller (bottom). However, HA is not able to displace BSA– (c) and it is shown not to affect the stability of the nanoparticle solution..... 59

Figure 4.1 (a) PVP Coating Stability. Baseline corrected ATR-FTIR spectra of a thin film of PVP-coated $Fe_3O_4$ NPs before (black) and after (red) exposure to seawater for 4 hrs. (b) PVP-$Fe_3O_4$ complex in water (c) PMF as a function of the distance between PVP-O and Fe. PVP and $(Fe_3O_4)_3$ are shown in CPK model and water molecules shown as lines. ..... 78

Figure 4.2 (a) PVP-coated NP with oil in water (b) PMF as a function of the distance between PVP and oil. NP is shown in VDW model, PVP is shown in licorice model, oil is shown in blue licorice model, $Na^+$, $K^+$ and $Cl^-$ ions are shown as spheres and water molecules shown as red dots. ..... 80

Figure 4.3 (a) ATR-FTIR spectra of various concentrations of fulvic acid in seawater on PVP-$Fe_3O_4$ NP films. The spectra show that absorptions associated with FA carboxylate groups (at 1390 and 1570 $cm^{-1}$) increase with increasing FA concentrations labeled with blue dash lines. Simultaneously, PVP desorbs from the surface as shown by the negative features at 1290 and 1652 $cm^{-1}$ labeled with red dash lines. (b) PVP-coated NP-NOM complex in water (c) PMF as a function of the distance between NOM and PVP. ..... 81

Figure 4.4 (a) NOM-oil complex in water (b) PMF as a function of the distance between NOM and oil. NOM is shown in licorice model, oil is shown in blue licorice model and TIP3P water molecules shown as points. ..... 83

Figure 4.5 Crude oil adsorption on PVP-$Fe_3O_4$ NPs in absence and presence of FA. ATR–FTIR spectra in the region extending from 1200 to 1610 and 2775 to 3000 $cm^{-1}$ of ~1.7 g/L crude oil solution (blue), a dry NP film after adsorption of crude oil on PVP–$Fe_3O_4$ NPs (red), and a dry NP film after adsorption of crude oil on FA –PVP–$Fe_3O_4$ NPs. These spectra show that FA does not impact crude oil adsorption on the NP surface. ..... 84

Figure 4.6 Schematic of surface processes for PVP coated $Fe_3O_4$ NPs in the presence of FA and crude oil. The processes occur in an ion-rich environment representing by blue and dark red dots. Initial PVP is unstable in seawater and can be readily displaced by FA to form new FA-PVP coatings. The adsorbed crude oil on new coating surface aggregate into micron size globules with the help of the ions.[7] ..... 85

Figure 5.1 ATR–FTIR spectra of the molecular adsorption on $TiO_2$ NP film, (a) 0.5 mg/ml BSA, (b) 0.1 mg/ml FA, respectively, as a function of time. The adsorption spectra shown were collected at 5 min (black), 30 min (red), 60 min (blue), 90 (magenta), 120 min (green). ..... 98

Figure 5.2 ATR-FTIR spectra following broadband irradiation of pure water on TiO2 NPs. The spectra shown were collected at 5 min (black), 30 min (red), 60 min (blue), 90 min (magenta), 120 min (green) and are referenced to the initial dark spectrum of the H2O--$TiO_2$ film. ..... 100

Figure 5.3 ATR–FTIR spectra of photochemical process of coated $TiO_2$ NPs, (a) BSA coated $TiO_2$, (b) FA coated $TiO_2$. The spectra shown were collected at 5 min (black), 30 min (red), 60 min (blue), 90 (magenta), 120 min (green)..... 101

Figure 5.4 ATR-FTIR spectra of the photochemical process of 10 mM sodium benzoate on $TiO_2$ NPs. The spectra shown were collected at initial spectrum in the dark (black), 5 min (red), 30 min (blue), 60 min (magenta), 90 min (green), 120 min (orange). ..... 103

Figure 5.5 Mass spectra of benzoate reacted with (a) bare $TiO_2$, (b) BSA-coated $TiO_2$ and (c) FA-coated $TiO_2$. ..... 104

Figure 5.6 The proposed pathway of benzoate oxidation ..... 105

Figure 5.7 ATR-FTIR spectra of photochemical process of coated $TiO_2$ NPs in presence of 2 mM sodium benzoate, (a) BSA coated $TiO_2$, (b) FA coated $TiO_2$. The spectra shown were collected at 5 min (black), 30 min (red), 60 min (blue), 90 (magenta), 120 min (green). ..... 106

Figure 6.1 (a) TEM image of the as-synthesized covellite nanoparticles. (b) Size distribution of the individual nanoparticles within the observed aggregates were determined by measuring the diameter of distinct particles which were typically at the edge of the larger aggregate (e.g. see red circles within the image). (c) powder X-ray diffraction data of as-synthesized covellite NPs to standard diffraction data for the covellite phase. ..... 121

Figure 6.2 ATR-FTIR spectra of oxidized covellite after 2 hrs. at RH 2%, RH 39% and RH 87%, respectively. ..... 122

Figure 6.3 (a) (b) (c) ATR-FTIR spectra of CuS under ambient conditions as a function of time at different RH: 2%, 39% and 87%, respectively. (d) Integrated peak area of sulfate absorption bands (1050 to 1170 $cm^{-1}$). Each spectrum was recorded every five minutes for a total time of 120 minutes. ..... 123

Figure 6.4 ATR-FTIR spectra in the spectral region extending from 2500 to 3600 $cm^{-1}$ as a function of time following. This is the same experiment shown in Figure 6.2 but for a different spectral region. It can be seen that as the surface transforms a broad peak grows in during at RH 87% in this higher wavenumber region. This is associated with adsorbed water on the surface..... 124

Figure 6.5 (a) crystal model of covellite, (b) High-resolution XPS characterization of covellite samples under various condition: Cu 2p region (left) and S 2p region (right). The blue spheres represent Cu and the yellow spheres represent sulfur. The binding models are visualized by VESTA..... 126

Figure 6.6 (a) PTIR spectroscopy for particles, with an inset showing the corresponding AFM height image of oxidized covellite NPs exposed to pure oxygen for 24 hrs at RH 87% with height images. (b) AFM height image and (c) chemical map of the sulfate rich regions of the particle taken at 1098 $cm^{-1}$. ..... 128

Figure 6.7 (a) High resolution TEM image of covellite NPs after oxidation at RH 87%, (b) the selected $CuSO_4$ phase, (c) the FFT pattern of the selected $CuSO_4$ phase, (d) the selected CuS phase, (e) the FFT pattern of the selected CuS phase. ..... 129

Figure 6.8 Simplified schematic of the surface during the transformation of CuS nanoparticles under different relative humidity. The transformation processes are composed of three main steps:

(1) CuS dissolution in adsorbed water, (2) ROS formation initiated by oxygen in presence of water, (3) further sulfide oxidation by ROSs. At RH 87%, $Cu^{+}$ also transforms to $Cu^{2+}$. ..... 131

LIST OF TABLES

Table 3.1 Representation of different molecules used in this study and their different pH dependent properties (protonation and secondary conformation). ..... 43

Table 3.2 Assignments for the vibrational frequencies ($cm^{-1}$) of the main functional groups in the studied molecules. ..... 45

Table 3.3 Summary of the surface coverage assuming a rigid layer. ..... 49

Table 5.1 Assignment of the vibrational frequencies ($cm^{-1}$) ..... 99

ACKNOWLEDGEMENTS

I would like to express my deep appreciation to my advisor Professor Vicki Grassian for her continuous support of my study and research, for her patience and immense knowledge. In the past five years, I got learned a lot from her, like attitude to work and study skills. During dissertation preparation, her guidance has proved to be invaluable.

I would like to thank my mother for all her support and encouragement. Every important decision I made in my life is totally supported by my mother, even though some of them sounded ridicules.

Also, I would like to thank my committee members. Prof. Andrew Kummel, your class was helpful for expanding my professional knowledge and increasing my presentation skills. Prof. Jessie Jokers, Prof. Kim Prather, Prof. Alina Schimpf and Donald Sirbuly, thank you all for your patience and insightful comments for my research.

Next, I appreciate all help from all Grassian group members. Dr. Natalia I Gonzalez-Pech and I worked out my first paper at UC San Diego. Her support in research and life really helped me out the situations. Amber Rose gave me a great help with writing including our paper and my dissertation. Dr. Liubin Huang used to help me with projects and mass spectrometry. Amber, Liubin and I together worked out a manuscript for publication. Victor Or gave me a strong support in preparing our manuscript in both technique and writing. The encouragements and discussion with Dr. Mona Shrestha were really helpful to relax from the frustration in the life. Izaac Sit, I would like to thank you here for your endeavors for our paper. Additionally, I also thank Sabrina Gonzalez-Calzada for her hardworking for our project. Dear Grassian group members, I really

enjoyed working with you all in these years. You guys spent your precious time with me. The discussion among us helped me find new ways to solve problems I met in class and research.

Special thanks to Dr. Shutang Chen and Dr. Jiang Wang, you are great friends and colleagues. I enjoyed being friends with you and your family. I was impressed with your selflessness to your friends. I really appreciate all help and support since I came to the USA.

Last but not the least, I would like to say thank you to my friends here for your encouragement, help, and support. You guys give me five years delight time to live in San Diego.

Chapter 1 & 2, in part, is currently being prepared for submission for publication of the material: Haibin Wu, Izaac Sit, Vicki H. Grassian. The dissertation author was the co-first author of this paper.

Chapter 3, in full, is a reprint of the material as it appears in Environmental Science: Nano 2018. Haibin Wu, Natalia I Gonzalez-Pech, Vicki H Grassian. The dissertation author was the primary investigator and author of this paper.

Chapter 4, in full, has been submitted for publication of the material as it may appear in Nature Nanotechnology, 2020, Linkel K. Boateng, Seyyedali Mirshahghassemi, Haibin Wu, Vicki H. Grassian, Joseph R.V. Flora, Jamie R. Lead. The dissertation author was the investigator and author of this paper. The dissertation author conducted the spectroscopic measurements and analysis. Dr. Linkel Boateng and Dr. Flora conducted the computational simulations. Dr. Seyyedali Mirshahghassemi provided the magnetite NPs for the research. I also acknowledge U of SC Research Cyberinfrastructure for the computational time used for the research.

Chapter 5 is currently being prepared for submission for publication of the material. Haibin Wu, Liubin Huang, Amber Rose, Vicki H. Grassian. The dissertation/thesis author was the primary investigator and author of this material.

Chapter 6 in full, has been submitted for publication of the material as it may appear in Nanoscale. Haibin Wu, Victor Or, Sabrina Gonzalez-Calzada, Vicki H. Grassian. The dissertation author was the primary investigator and author of this paper.

## VITA

2010 Bachelor of Sciences, Lanzhou University, Lanzhou, CN

20010-2012 Working, Changchun Institute of the Applied Chemistry, CAS

2012-2015 Teaching Assistant, University of Arkansas

2015 Master of Science, University of Arkansas

2016-2020 Research Assistant, University of California San Diego

2020 Doctor of Philosophy, University of California San Diego

## PUBLICATIONS

1. Haibin Wu, Liubin Huang, Amber Rose, Vicki H. Grassian, "Surface Adsorbed Biologically and Environmentally Relevant Ligands on $TiO_2$ Nanoparticles Transformations: The Influence on Reactivity of Nanoparticles", submitted.

2. Haibin Wu, Victor Or, Sabrina Gonzalez-Calzada, Vicki H. Grassian, CuS Nanoparticles in Humid Environments: Adsorbed Water Enhances the Transformation of CuS to $CuSO_4$; submitted.

3. Haibin Wu, Izaac Sit, Vicki H. Grassian, Probing Nanoparticle Surface Chemistry in Aqueous Media Under Different Environmental Conditions of pH and Temperature, in preparation, (co-first author).

4. Linkel K. Boateng, Seyyedali Mirshahghassemi, Haibin Wu, Vicki H. Grassian, Joseph R.V. Flora, Jamie R. Lead, Mechanistic study of oil adsorption onto PVP-coated nanoparticles: An integrated experimental and molecular dynamics study; submitted.

5. Haibin Wu, Natalia Gonzalez Pech, Vicki H. Grassian, Displacement Reactions between Environmentally and Biologically Relevant Ligands on $TiO_2$ Nanoparticles: Insights into the Aging of Nanoparticles in the Environment, *Environ. Sci.*: Nano, 2019, 6, 489-504.

6. Sanjaya Jayalath, Haibin Wu, Sarah Larsen, Vicki Grassian, Surface Adsorption of Suwannee River Humic Acid on $TiO_2$ Nanoparticles: A Study of pH and Particle Size, *Langmuir*, 2018, 34, 3136–3145.

## FIELDS OF STUDY

Major Field: Physical Chemistry

Professor Vicki H. Grassian

ABSTRACT OF THE DISSERTATION

Surface Transformations of Metal Oxide and Metal Sulfide Nanoparticles: Surface Adsorption, Surface Reactions and Surface Oxidation

by

Haibin Wu

Doctor of Philosophy in Chemistry

University of California San Diego, 2020

Professor Vicki H. Grassian, Chair

As nanoparticle (NP) surfaces are highly reactive, NPs can interact with environmental and biological systems and undergo complicated surface transformation processes, including ligand adsorption, ligand displacement reactions, surface oxidation. These transformations can significantly alter the physiochemical properties of NPs. Although surface transformations have been proposed in previous studies, information on the details of these mechanisms and the impact on NP behavior remains unclear.

In this dissertation, *in-situ* ATR–FTIR was employed to better understand surface transformation on oxide NPs (i.e. $TiO_2$). Displacement reactions of ascorbic acid, citric acid, and bovine serum albumin by humic acid show three different behaviors ranging from complete displacement, partial displacement, and no displacement, respectively. The detailed chemistry analyzed using two-dimensional correlated spectroscopy indicate the formation of different types of adsorption modes including outer sphere and inner sphere complexation during the reaction. These reactions are important to understand if NPs are to be used for *in-situ* environmental remediation. For example, we through combined *in-situ* ATR–FTIR and molecular dynamic simulations studied how fulvic acid (FA) alters the performance of polyvinylpyrrolidone coated magnetite NPs in crude oil clean-up. Additionally, the effects of surface coatings on $TiO_2$ NP reactivity associated with the formation of reactive oxygen species (ROS) was investigated. The results indicate that the generated ROS on $TiO_2$ NPs under light can be completely quenched by BSA but partially by FA.

Another focal point of this dissertation is on surface oxidation of CuS NPs. The details of oxidation were investigated via *in-situ* ATR–FTIR in oxygen under various relative humidity (RH) and the formation of sulfate on the surface at higher relative humidity was observed. These surface species were confirmed by microscopic methods including high resolution transmission electron

microscope and atomic force microscope infrared-spectroscopy. X-ray photoelectron spectroscopy data suggests that CuS NPs show little oxidation under dry conditions (RH < 2%), while surface oxidation occurs stepwise with increasing RH resulting in distinct products.

Overall, these studies presented in this dissertation provide valuable insights into the details of mechanisms associated with surface transformation and impacts on the reactivity and properties of NPs.

# Chapter 1 Introduction

## 1.1 Nanoparticles

Nanoparticles (NPs) are regarded as zero dimensional nanomaterials with a size in the range of 1 - 100 nm, in which the properties are dramatically different from that of the bulk-scale.[1] These properties are not only related to chemical composition and crystalline structure but also size and morphology at a nanoscale level. At the nanoscale, quantum confinement effects strongly influence electrical, thermal and optical properties of these particles. This effect is evident for particles with a size smaller than their double Bohr radius.[2] In addition, another important consequence of small size is an increased surface-to-volume ratio and a high specific surface area. When the size of particles is reduced to the nanoscale, surface atoms comprising a small proportion in the bulk will play a crucial role in generation of strain and structural perturbations.[3] The asymmetrical force acting on the surface atoms leads to high surface tension leading to bond lengths at the surface differing from that of the bulk. Consequently, the interfacial properties, reactivity and potential toxicity of particles at the nanoscale (especially less than 30 nm), are different from bulk materials.[1] Figure 1.1 shows the diverse physiochemical processes occurring on the surface of NPs, including surface acid-base reactions, redox reactions, and ion dissolution. Due to changes of physicochemical properties caused by size effects, NPs show unique size dependent properties in catalysis, magnetism, optics etc. For example, gold nanoparticles display size-dependent catalytic activities in both product formation and dissociation reactions.[4] Another type of noble metal nanoparticle, 8 nm Pd, exhibits high performance in catalyzing hydrogenation of alkenes at room temperature.[5] The size dependent property of magnetic particles is reflected in the enhancement of magnetization in 12 nm particles more than any other size particles.[6] Numerous metal and semiconductor NPs have been developed as catalysts in solar cells, batteries,

water splitting, fuel cells, and $CO_2$ reduction.[7-12] In addition to applications in catalysis, NPs have been employed for medical diagnostics, imaging and even therapies. For instance, some NPs have been widely employed in MRI imaging as a contrast agent due to their prominent magnetic properties.[13, 14] Plasmonic NPs, such as Au and CuS NPs, are used in tumor imaging and photothermal therapy.[15-18]

Though NPs exhibit wide potential for applications and have prominent properties, the increasing usage of NPs has raised concerns about the potential risks to human health and the

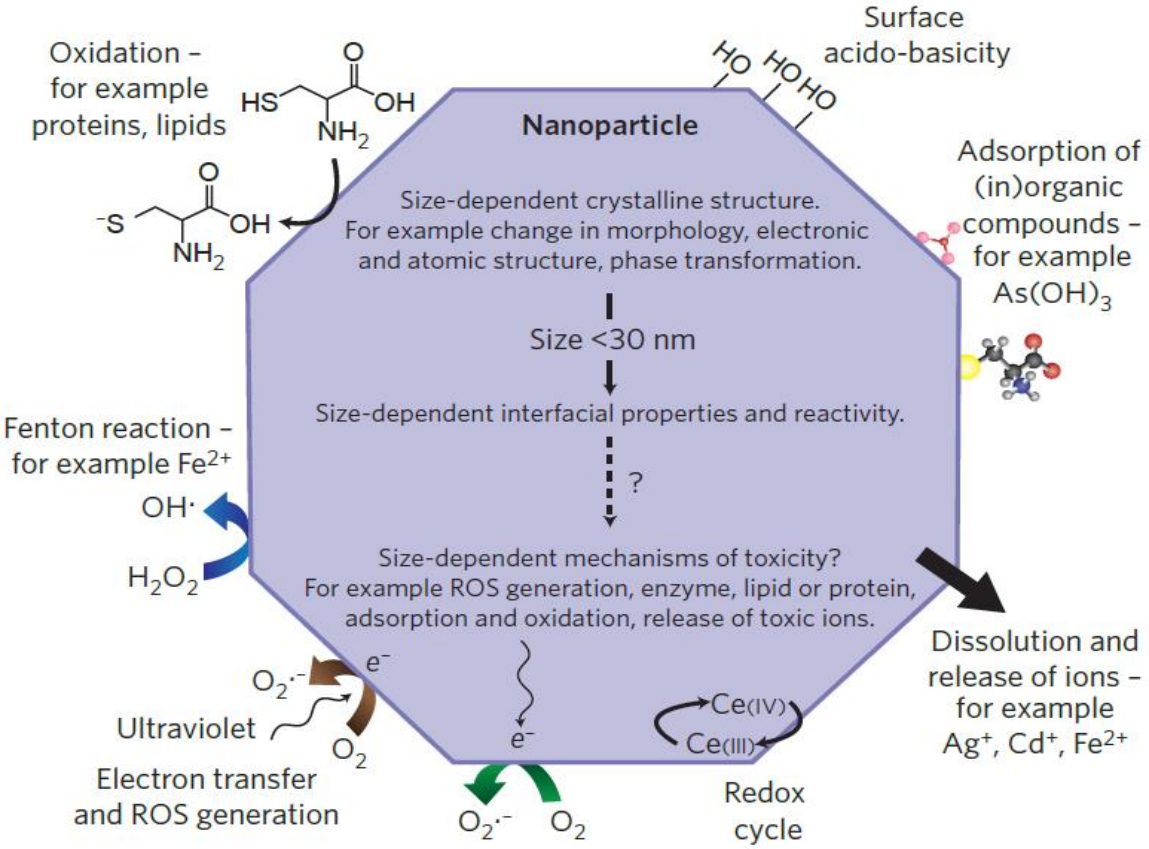


**Figure 1.1** Physicochemical Processes occurring at the surface of an inorganic nanoparticle. (Reprinted and modified from Ref 1 with permission from Nature Publishing Group).

environment.[19-22] The high surface energy turns NPs into very active entities under different circumstances. For example, silver NPs are utilized as antibacterial agents in a wide range of

applications, such as face masks and detergents. Silver NPs released into the environment, however, can undergo different transformations including dissolution, surface aging and precipitation.[23] These transformations promote the release of toxic silver ions into the environment, which can cause ecotoxicity. As implied by previous studies, gold NPs may not have an immediate negative impact on cell viability for short-term exposure but can cause unpredicted DNA damage for longer-term exposure.[24, 25] Furthermore, uptake of NPs has caused significant research attention focused on the impact of NPs on human health. Recent reports show that metal oxide nanoparticles have been found in human brain cells and this is believed to be a positive correlation with certain disease occurrence.[26, 27]

### 1.2 Metal Oxide and Metal Sulfide NPs

Based on composition, inorganic NPs can be primarily classified as metal, oxide, sulfide, nitride, phosphide, silica and carbon based. Because of their potential widespread applications and unique physiochemical properties, studies on these NPs have spiked in recent decades. Among those materials, oxides and sulfides have attracted much research interest as semiconductors.[28, 29] Engineered metal oxide and metal sulfide NPs represent a wide range of compounds on the nanoscale. Among these diverse semiconductor NPs, titanium dioxide and copper sulfide NPs have attracted attention based on their high stability, biocompatibility, and performance in catalysis.

#### 1.2.1 Titanium Dioxide

Titanium dioxide ($TiO_2$), also known as titania, comes in natural forms as anatase, brookite and rutile. For particles greater than 50 nm in size, rutile has been shown to be the most thermodynamically stable form among these natural forms.[30] $TiO_2$ is a semiconductor. Its electrode potential of the conduction band is lower than 0 V vs NHE, and the electrode potential of the valence band is around -3.2 V vs NHE.[31] This unique band structure indicates that $TiO_2$ can be a

good potential catalyst for water splitting and solar energy conversion.[32-36] $TiO_2$ can generate excited electrons when irradiated by UV light, and form positively charged holes in the valence band. The electron-hole pairs (excitons) have high reactivity in catalyzing chemical reactions. The excitons recombine and release energy in other forms e.g. florescence or heat. For catalytic processes, reactions occur mostly on or near the surfaces of the catalysts. Therefore, recombination weakens the catalytic activity and conversion efficiency. For $TiO_2$ NPs, due to its large surface area and defects on the surfaces, the generated charge carriers (e-/h+) can be easily trapped on the surface. Consequently, the lifetime of the electron-pair is elongated, resulting in enhancing catalytic activity and efficiency.

Apart from high reactivity, $TiO_2$ NPs have high crystalline lattice energy and strong chemical bonds between the Ti and O ions; thus, $TiO_2$ is thought to be chemically and photochemically stable. Due to the high reactivity and chemical stability, $TiO_2$ NPs have been widely employed in many aspects, such as biosensors,[37] sunscreen additives,[38] photocatalysts and photovoltaic cells[39, 40 41]. However, with the large scale of $TiO_2$ NP usage, a considerate amount has been released into the environment and the potential impacts of $TiO_2$ NPs on the environment and on human health have arisen. $TiO_2$ NPs in the environment likely undergo surface ligands reactions (e.g. adsorption, desorption, and displacement). Alteration of the surface character can further impact behaviors of $TiO_2$ NPs in the environment, such aggregation, transportation, reactivity, and toxicity.

### 1.2.2 Copper Sulfide

Copper sulfide (CuS) is a diverse family comprising of six domain crystal phases in nature: chalcocite, djurleite, digenite, anilite, roxbyite and covellite. The diversity of the binary Cu-S system is due to various nonstoichiometric compositions, represented as $Cu_{2-x}S$.[42] The vacancies

of Cu in copper sulfide, caused either by oxidation or carbonization, lead to a transition of copper sulfide from semiconductor to metal-like materials. Among these phases, chalcocite and covellite receive more attention than others due to their prominent physiochemical properties.[42] Chalcocite is, however, unstable under ambient conditions despite its potential applications in energy and sensing;[43, 44] whereas covellite is regarded as the more stable form of copper sulfide.[45] Structural analysis indicates that covellite has a hexagonal symmetry (*hcp*) with the cell dimensions: a = 3.976 and c=16.382 Å.[46] Covellite has an unusual structure composed of two layers, $Cu_3S{-}CuS_3$, stitched together by S−S covalent bonds. Cu atoms are located in two different environments i.e. $CuS_3$ units (triangular coordination) and $CuS_4$ units (tetrahedral coordination) along the c-axis.[43] Along with structure, oxidation states of each element in covellite have been the subject of debate for years.[47-50] Much of the published research shows that copper ions in covellite possess a +1charge instead of a +2 charge, while sulfur has various valences and oxidation states. Thus it has been proposed that a better representation of covellite would be $Cu_3S_3$ with the oxidation states as $Cu^{+}{}_3S^{2-}S^{-}{}_2$.[51] It is interesting that covellite possesses unique metallic-like characteristics for its conductivity,[51] with an optical band gap.[52] Vacancies of Cu appearing in the valence band leads to the appearance of localized surface plasmon resonance (LSPR) in the near IR region.[53, 54] The LSPR character of covellite in the NIR makes it as a good photothermal agent for tumor therapy.[55-57] Furthermore, Tang and his co-workers recently explored the usage of CuS NPs as a photothermal switch for TRPV1.[58] In addition, the special layer feature in CuS crystals allows for the intercalation of alkali metal ions (i.e. Na, Li) in between the S−Cu−S layers, thus making CuS a promising electrode material for battery applications.[44, 59] As discussed above, the surface states of CuS NPs have an important effect on its properties, such as dissolution and LSPR.

### 1.3 Surface Chemistry and Transformation

Due to the high surface-to-area ratio, the surface chemistry of these nanoparticles plays an important role in their properties and behavior. In this dissertation research, several different types of surface chemistry and surface transformations have been explored. As discussed in more detail below, we focus on surface oxidation and surface ligand reactions (e.g. adsorption, desorption, and displacement) on metal oxide NPs (i.e. $TiO_2$) and the effects on the reactivity of generating reactive oxygen species.

### 1.3.1 Surface Ligand Reactions

Molecular adsorption onto surfaces can change the surface composition and surface charge. Surface adsorption processes can be either reversible and/or irreversible, sometimes referred to as physisorption and chemisorption. Physisorption interactions are derived from intermolecular forces (e.g. Van der Waals, electrostatics, hydrogen bonding). For chemisorption, stronger bonding interactions between the surface and ligand occur. Chemisorption of organic ligands depends on the nanoparticle composition due to the varying surface affinity between different chemical groups.[60] Molecules with carboxylic, hydroxyl and phosphate groups are easily chemisorbed to

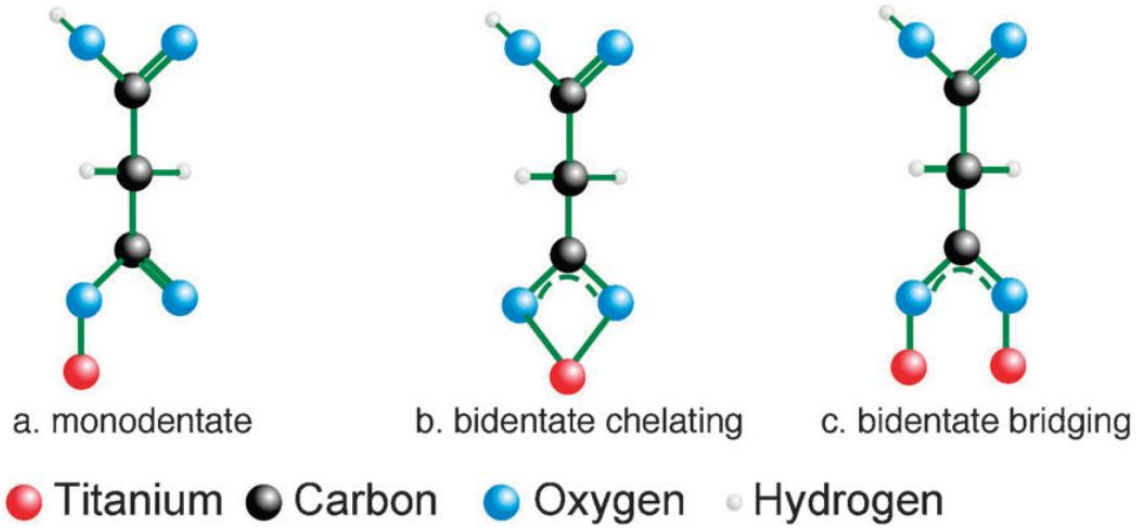


**Figure 1.2** Possible binding modes of a carboxylic acid to a $TiO_2$ surface. (Reprinted and modified from Ref 61 with permission from Royal Chemical Society).

oxide surfaces (e.g. $Fe_3O_4$ and $TiO_2$) through intrinsic surface hydroxyl groups, which are called ligand exchange reactions. The carboxylic group has three main bonding modes with surface cations by forming inner sphere complexes: bidentate bridging, monodentate, and bidentate chelating (as shown in Figure 1.2).[61] The most common ligands on these surfaces are amine, thiol, and hydroxyl groups. Liquid-solid interfaces are important in many biological systems and environmental systems, where water is present. With the assistance of water near the surface, outer sphere complexes of ligand and surface ions are observed under some conditions, which often means a weaker interaction.

For oxide NPs, the surface is covered by surface hydroxyl groups and can range from 1-10 -OH/nm$^2$ depending on particle composition.[62, 63] These hydroxyl groups from the dissociation of water on these surfaces. When oxide NPs are in an aqueous medium, the surface charge arises from the protonation and deprotonation of these surface hydroxyl groups.[64] Protonation and deprotonation is highly influenced by the solution pH. Changes in surface charge for silica, for example, can be described as:[65]

$$\equiv \boldsymbol{SiOH} \leftrightarrow \boldsymbol{SiO^-} + \boldsymbol{H^+} \qquad (\mathbf{1.1})$$

$$\equiv \boldsymbol{SiOH} + \boldsymbol{H^+} \leftrightarrow \boldsymbol{SiOH_2}^+ \qquad (\mathbf{1.2})$$

The pH dependent protonation/deprotonation depends on the particle isoelectric point (IEP). The IEP is defined as the pH at which a molecule or colloid is neutrally charged. For silica this value is about 2. Moreover, intermolecular interactions can also be influenced by pH. A recent study showed that pH affects electron delocalization and promotes $\pi - \pi$ interactions between adsorbed aromatic molecules on gold NPs.[66] The intermolecular interaction can affect molecular orientation that may facilitate a chemical reaction between adsorbed molecules.[67-73]

1.3.2 Reactive Oxygen Species (ROS)

Reactive oxygen species (ROS) are defined as a chemically unstable and reactive molecule containing oxygen. Examples of ROS include superoxide radicals, hydroxyl radicals and hydrogen peroxide. *Superoxides* ($\boldsymbol{O_2^{\bullet -}}$) are important products of one electron reduction reactions of an oxygen molecule, which can be the precursor of other ROS. *Hydroxyl radicals* ($OH^{\bullet}$) are highly reactive ROS as the neutral form of the hydroxide ion. *Hydrogen peroxide* ($H_2O_2$) is the simplest peroxide used as an oxidizer and antiseptic. The chemical reactivity of ROS can be reflected by their half-life and diffusion. The $OH^{\bullet}$ radical is highly reactive, as its half-life is approximately $10^{-9}$ s (1 ns), while the other two have a few orders of magnitude longer half-life than $OH^{\bullet}$: $10^{-6}$ s and $10^{-5}$ s for $\mathbf{O_2^{\bullet -}}$ and $H_2O_2$, respectively.[74] Given the very short half-life of $OH^{\bullet}$, it is very likely that $OH^{\bullet}$ is scavenged a few angstroms (Å) close to its site of formation.[74] In contrast, $\mathbf{O_2^{\bullet -}}$ and $H_2O_2$ have larger values of diffusion distance with upper limits of 0.16 μm and 0.23-0.46 μm, respectively.[74-76] Hydrogen peroxide, compared to the other two ROS, is more stable but decomposes slowly in the presence of light. Apart from these three major ROS, singlet oxygen is a gas phase ROS induced by light. These four are major ROS generated in nature, such as biological system and the atmosphere. Most ROS are found as natural byproducts of normal cell metabolism.[77, 78] Due to high chemical reactivity, controllable amounts of ROS can be utilized for different therapies.[79, 80] However, ROS are harmful to organisms at high concentrations by causing damage to important biological molecules including proteins, fatty acids and DNA.[81]

Many studies have shown that NPs used in catalysis, drug delivery and therapy produce ROS in the process.[80, 82] As primary intermediates of some reactions (e.g. photocatalytic reactions), the mechanism of ROS generation has become crucial to understanding the performance and safety of nanomaterials. The major mechanisms of NP induced ROS are the photoinduced and chemical redox mechanisms. Photoinduced ROS generation mostly occurs on semiconductor NPs under irritation, for example, $TiO_2$, ZnO and quantum dots.[83, 84] The semiconductors are excited, forming excitons that have separated holes and electrons. The excited electrons have the ability to reduce surface adsorbed oxygen molecules to superoxide ions and the holes can oxidize water molecules to hydroxyl radicals, when the energy levels match the redox potential of water oxidation. The chemical redox mechanism is based on the oxygen reduction reaction and water oxidation reaction by active NP surfaces. The process may also involve a Fenton reaction triggered by dissolved ions from the NP surface. The proposed mechanisms are shown in Figure 1.3. Both mechanisms indicate that the generation of ROS mainly occur on the NP surface. Therefore, surface properties,

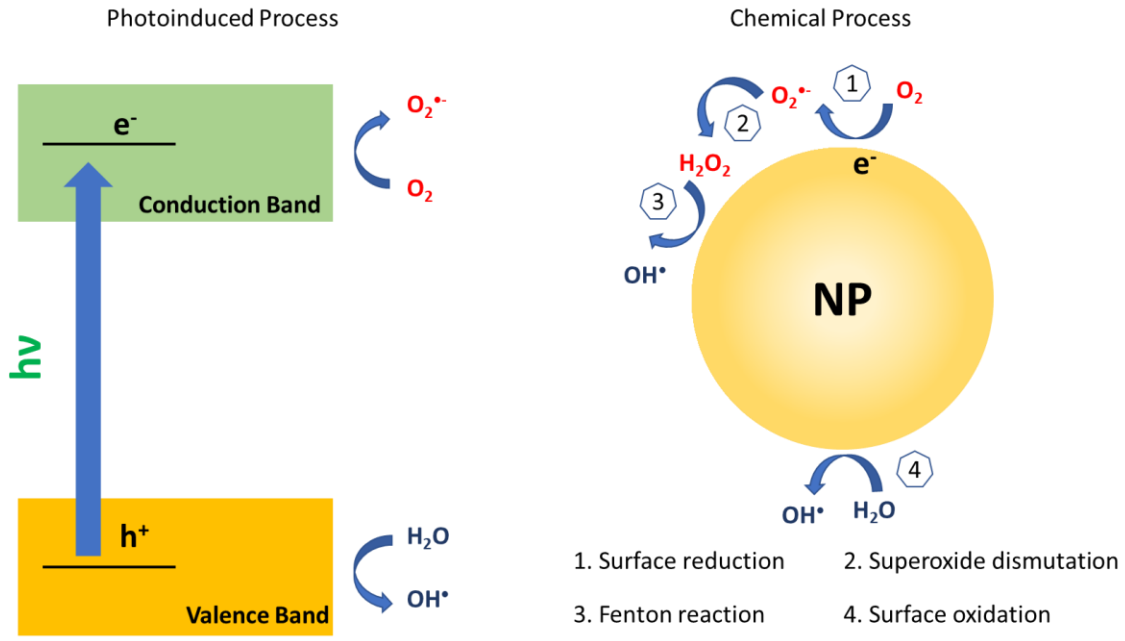


**Figure 1.3** Illustration of ROS generation mechanisms, photoinduced mechanism (left) and chemical redox mechanism (right).

including surface oxidation state, surface ligands and surface charges, play an important role in ROS production.

## 1.4 Dissertation Motivation and Objectives

Due to their large usage and release, it is expected that NPs will make their way into the environment, including soils, waters and even the atmosphere.[21, 22] Most NPs are dynamic entities and their states can be altered significantly over time. It is evident that NPs can undergo aging and transformations when released to the environment. However, the majority of studies concentrate on the environmental impacts of NPs in their native sates, and only a few studies have focused on the dynamic changes at the molecular level in details. These changes would largely impact the properties of NPs including dissolution, reactivity, and aggregation. In addition, aging will affect their behavior and interactions with biomolecules in the environment. Surface coatings of NPs play a key role in their behavior in the environment. NPs with coatings in the environment are expected to undergo ligand displacement processes between environmentally and biologically relevant molecules. This change will lead to new features and properties of NPs in terms of dissolution, aggregation, and reactivity. In addition to ligand reactions, the surface oxidation state is another crucial factor that would influence behaviors of NPs. In the other words, the physiochemical properties of NPs are largely reshaped by the new surface states after transformation. The details of these transformations and its impacts on important properties still need to be further studied. The objective of this dissertation is to explore the surface transformations processes such as ligand reactions and surface oxidation and understand effects of the transformations on the physiochemical properties of NPs. Therefore, we proposed three scientific questions to address in this dissertation:

1. *What are the details of the mechanisms for environmentally and biologically relevant ligand reactions on stable oxide nanomaterials at the molecular level?*

The research presented in Chapter 3 is about the investigation of ligand reactions including adsorption, desorption, and displacement, on $TiO_2$ NPs. The ligand molecules are ascorbic acid, citric acid, humic acid and BSA protein as representatives of molecules in biological and environmental systems. Various techniques (e.g. in-situ ATR–FTIR, QCM-D) were employed to address this science question. The focus of this chapter is on displacement reactions occurring between humic acid with the other three molecules, representing the processes that NPs may undergo when released to the environment. Further analysis by 2DCOS provides more details of the displacement processes for better understanding of ligand processes.

2. *What impacts do these reactions have on the behaviors of nanoparticles in terms of reactivity and performance in environmental applications?*

Studies conducted in chapter 4 and 5 focus on impacts of ligand reactions on NPs. In chapter 4, we combine molecular simulation and ATR–FTIR spectroscopy to study how ligand reactions affect the performance of magnetite NPs in crude oil clean-up in sea water. The principles obtained from displacement reactions in chapter 3 were used to explain how the presence of fulvic acid affects the crude oil adsorption compared to original surface. The simulation results supported the experimental observation.

The reactivity of NPs coated by different ligands was investigated in chapter 5. The study focuses on ROS on $TiO_2$ NPs under irradiation. The process was studied via *in-situ* ATR–FTIR which is powerful to observe the change caused by intermediates. Furthermore, mass spectrometry was also used to provide more information of products after the process.

In addition, sedimentation study carried out in chapter 3 also implies the stability of $TiO_2$ NPs suspension influencing by ligand displacement reactions in natural waters.

3. *How do metal sulfide nanoparticles oxidize in the environment and what environmental factor(s) (such as humidity) significantly contribute to the oxidation?*

The surface oxidation relevant to the stability of sulfide NPs is studied in chapter 4. We focus on CuS NPs (covellite) which show wide potential applications in energy and medical uses. The experiments were carried out under a controllable RH in pure oxygen gas. The conditions were controlled from dry, ambient and humid. The oxidation courses were *in-situ* observed by ATR–FTIR and surface species were analyzed by XPS. Furthermore, advanced microscopic methods (i.e. AFM-IR and HR-TEM) were also utilized for surface imaging.

Ligand displacement reactions will modify the stability of nanomaterials during their transport in the environment. Furthermore, possible generation of ROS during surface transformation of NPs would provide new angles to consider the safety of NPs in their wide variety of applications. The surface oxidation study offers a new understanding of surface transformation of sulfide NPs. Additionally, the mechanisms of the oxidation processes suggest potential toxicity to biological and environmental systems. Overall, the insights of this dissertation are of significant relevance to the fate of nanomaterials and impacts on their properties.

## 1.5 Acknowledgements

Chapter 1, in part, is currently being prepared for submission for publication of the material: Haibin Wu, Izaac Sit, Vicki H. Grassian. The dissertation author was the co-first author of this paper.

## 1.6 References


1. Auffan M, Rose J, Bottero J-Y, Lowry GV, Jolivet J-P, Wiesner MR. Towards a definition of inorganic nanoparticles from an environmental, health and safety perspective. *Nature Nanotechnology* 2009, 4(10): 634-641.

2. Einevoll GT. Confinement of excitons in quantum dots. *Physical Review B* 1992, 45(7): 3410-3417.

3. Kumar S, Saralch S, Jabeen U, Pathak D. 14 - Metal oxides for energy applications. In: Thomas S, Tresa Sunny A, Velayudhan P (eds). *Colloidal Metal Oxide Nanoparticles*. Elsevier, 2020, pp 471-504.

4. Zhou X, Xu W, Liu G, Panda D, Chen P. Size-Dependent Catalytic Activity and Dynamics of Gold Nanoparticles at the Single-Molecule Level. *Journal of the American Chemical Society* 2010, 132(1): 138-146.

5. Mondal J, Trinh QT, Jana A, Ng WKH, Borah P, Hirao H, Zhao Y. Size-Dependent Catalytic Activity of Palladium Nanoparticles Fabricated in Porous Organic Polymers for Alkene Hydrogenation at Room Temperature. *ACS Applied Materials & Interfaces* 2016, 8(24): 15307-15319.

6. Patsula V, Moskvin M, Dutz S, Horák D. Size-dependent magnetic properties of iron oxide nanoparticles. *Journal of Physics and Chemistry of Solids* 2016, 88: 24-30.

7. Nie Y, Li L, Wei Z. Recent advancements in Pt and Pt-free catalysts for oxygen reduction reaction. *Chemical Society Reviews* 2015, 44(8): 2168-2201.

8. Bambagioni V, Bianchini C, Marchionni A, Filippi J, Vizza F, Teddy J, Serp P, Zhiani M. Pd and Pt–Ru anode electrocatalysts supported on multi-walled carbon nanotubes and their use in passive and active direct alcohol fuel cells with an anion-exchange membrane (alcohol =methanol, ethanol, glycerol). *Journal of Power Sources* 2009, 190(2): 241-251.

9. Yajima T, Wakabayashi N, Uchida H, Watanabe M. Adsorbed water for the electro-oxidation of methanol at Pt-Ru alloy. *Chemical Communications* 2003(7): 828-829.

10. Park K-W, Choi J-H, Kwon B-K, Lee S-A, Sung Y-E, Ha H-Y, Hong S-A, Kim H, Wieckowski A. Chemical and Electronic Effects of Ni in Pt/Ni and Pt/Ru/Ni Alloy Nanoparticles in Methanol Electrooxidation. *The Journal of Physical Chemistry B* 2002, 106(8): 1869-1877.

11. Zhu W, Michalsky R, Metin O, Lv H, Guo S, Wright CJ, Sun X, Peterson AA, Sun S. Monodisperse Au nanoparticles for selective electrocatalytic reduction of $CO_2$ to CO. *Journal of the American Chemical Society* 2013, 135(45): 16833-16836.

12. Chen S, Jenkins SV, Tao J, Zhu Y, Chen J. Anisotropic Seeded Growth of Cu–M (M = Au, Pt, or Pd) Bimetallic Nanorods with Tunable Optical and Catalytic Properties. *The Journal of Physical Chemistry C* 2013, 117(17): 8924-8932.

13. Kobayashi H, Brechbiel MW. Nano-sized MRI contrast agents with dendrimer cores. *Advanced Drug Delivery Reviews* 2005, 57(15): 2271-2286.

14. Shin T-H, Choi Y, Kim S, Cheon J. Recent advances in magnetic nanoparticle-based multi-modal imaging. *Chemical Society Reviews* 2015, 44(14): 4501-4516.

15. Huang X, El-Sayed IH, El-Sayed MA. Applications of gold nanorods for cancer imaging and photothermal therapy. *Methods Mol Biol* 2010, 624: 343-357.

16. Zhou M, Zhang R, Huang M, Lu W, Song S, Melancon MP, Tian M, Liang D, Li C. A Chelator-Free Multifunctional [64Cu]CuS Nanoparticle Platform for Simultaneous Micro-PET/CT Imaging and Photothermal Ablation Therapy. *Journal of the American Chemical Society* 2010, 132(43): 15351-15358.

17. Yang R-M, Fu C-P, Fang J-Z, Xu X-D, Wei X-H, Tang W-J, Jiang X-Q, Zhang L-M. Hyaluronan-modified superparamagnetic iron oxide nanoparticles for bimodal breast cancer imaging and photothermal therapy. *International journal of nanomedicine* 2016, 12: 197-206.

18. Yin D, Li X, Ma Y, Liu Z. Targeted cancer imaging and photothermal therapy via monosaccharide-imprinted gold nanorods. *Chemical Communications* 2017, 53(50): 6716-6719.

19. Khan I, Saeed K, Khan I. Nanoparticles: Properties, applications and toxicities. *Arabian Journal of Chemistry* 2019, 12(7): 908-931.

20. Gnach A, Lipinski T, Bednarkiewicz A, Rybka J, Capobianco JA. Upconverting nanoparticles: assessing the toxicity. *Chemical Society Reviews* 2015, 44(6): 1561-1584.

21. Bundschuh M, Filser J, Lüderwald S, McKee MS, Metreveli G, Schaumann GE, Schulz R, Wagner S. Nanoparticles in the environment: where do we come from, where do we go to? *Environmental Sciences Europe* 2018, 30(1): 6.

22. Giese B, Klaessig F, Park B, Kaegi R, Steinfeldt M, Wigger H, von Gleich A, Gottschalk F. Risks, Release and Concentrations of Engineered Nanomaterial in the Environment. *Scientific Reports* 2018, 8(1): 1565.

23. Dos Santos CA, Seckler MM, Ingle AP, Gupta I, Galdiero S, Galdiero M, Gade A, Rai M. Silver Nanoparticles: Therapeutical Uses, Toxicity, and Safety Issues. *Journal of Pharmaceutical Sciences* 2014, 103(7): 1931-1944.

24. Senut M-C, Zhang Y, Liu F, Sen A, Ruden DM, Mao G. Size-Dependent Toxicity of Gold Nanoparticles on Human Embryonic Stem Cells and Their Neural Derivatives. *Small* 2016, 12(5): 631-646.

25. Alkilany AM, Murphy CJ. Toxicity and cellular uptake of gold nanoparticles: what we have learned so far? *Journal of nanoparticle research : an interdisciplinary forum for nanoscale science and technology* 2010, 12(7): 2313-2333.

26. D'Agata F, Ruffinatti FA, Boschi S, Stura I, Rainero I, Abollino O, Cavalli R, Guiot C. Magnetic Nanoparticles in the Central Nervous System: Targeting Principles, Applications and Safety Issues. *Molecules* 2017, 23(1): 9.

27. Teleanu DM, Chircov C, Grumezescu AM, Volceanov A, Teleanu RI. Impact of Nanoparticles on Brain Health: An Up to Date Overview. *Journal of clinical medicine* 2018, 7(12): 490.

28. Chavali MS, Nikolova MP. Metal oxide nanoparticles and their applications in nanotechnology. *SN Applied Sciences* 2019, 1(6): 607.

29. Metal Sulfide Nanoparticles. *Design of Nanostructures*, pp 227-257.

30. Zhang H, Banfield JF. Understanding Polymorphic Phase Transformation Behavior during Growth of Nanocrystalline Aggregates: Insights from $TiO_2$. *The Journal of Physical Chemistry B* 2000, 104(15): 3481-3487.

31. Beranek R. (Photo)electrochemical Methods for the Determination of the Band Edge Positions of $TiO_2$-Based Nanomaterials. *Advances in Physical Chemistry* 2011, 2011: 786759.

32. Murphy AB. Band-gap determination from diffuse reflectance measurements of semiconductor films, and application to photoelectrochemical water-splitting. *Solar Energy Materials and Solar Cells* 2007, 91(14): 1326-1337.

33. Khan SUM, Al-Shahry M, Ingler WB. Efficient Photochemical Water Splitting by a Chemically Modified n-$TiO_2$. *Science* 2002, 297(5590): 2243.

34. Peng B, Jungmann G, Jäger C, Haarer D, Schmidt H-W, Thelakkat M. Systematic investigation of the role of compact $TiO_2$ layer in solid state dye-sensitized $TiO_2$ solar cells. *Coordination Chemistry Reviews* 2004, 248(13): 1479-1489.

35. Campbell WM, Burrell AK, Officer DL, Jolley KW. Porphyrins as light harvesters in the dye-sensitised $TiO_2$ solar cell. *Coordination Chemistry Reviews* 2004, 248(13): 1363-1379.

36. Fujishima A, Honda K. Electrochemical photolysis of water at a semiconductor electrode. *Nature* 1972, 238(5358): 37-38.

37. Jang HD, Kim SK, Chang H, Roh KM, Choi JW, Huang Jx. A glucose biosensor based on $TiO_2$–Graphene composite. *Biosensors and Bioelectronics* 2012, 38(1): 184-188.

38. Jacobs JF, van de Poel I, Osseweijer P. Sunscreens with Titanium Dioxide (TiO(2)) Nano-Particles: A Societal Experiment. *Nanoethics* 2010, 4(2): 103-113.

39. Zhou Q, Zhong YH, Chen X, Liu JH, Huang XJ, Wu YC. Adsorption and photocatalysis removal of fulvic acid by $TiO_2$–graphene composites. *Journal of Materials Science* 2014, 49(3): 1066-1075.

40. Dolamic I, Bürgi T. In situ ATR-IR study on the photocatalytic decomposition of amino acids over Au/$TiO_2$ and $TiO_2$. *The Journal of Physical Chemistry C* 2011, 115(5): 2228-2234.

41. Jose R, Thavasi V, Ramakrishna S. Metal oxides for dye-sensitized solar cells. *Journal of the American Ceramic Society* 2009, 92(2): 289-301.

42. Coughlan C, Ibáñez M, Dobrozhan O, Singh A, Cabot A, Ryan KM. Compound Copper Chalcogenide Nanocrystals. *Chemical Reviews* 2017, 117(9): 5865-6109.

43. Karikalan N, Karthik R, Chen S-M, Karuppiah C, Elangovan A. Sonochemical Synthesis of Sulfur Doped Reduced Graphene Oxide Supported CuS Nanoparticles for the Non-Enzymatic Glucose Sensor Applications. *Scientific Reports* 2017, 7(1): 2494.

44. Jiang K, Chen Z, Meng X. CuS and $Cu_2S$ as Cathode Materials for Lithium Batteries: A Review. *ChemElectroChem* 2019, 6(11): 2825-2840.

45. Roberts WMB, Buchanan AS. The effects of temperature, pressure, and oxygen on copper and iron sulphides synthesised in aqueous solution. *Mineralium Deposita* 1971, 6(1): 23-33.

46. Ohmasa M, Suzuki M, Tak, Eacute, Uchi Y. A refinement of the crystal structure of covellite, CuS. *Mineralogical Journal* 1977, 8(6): 311-319.

47. Goh SW, Buckley AN, Lamb RN. Copper(II) sulfide? *Minerals Engineering* 2006, 19(2): 204-208.

48. Xie Y, Riedinger A, Prato M, Casu A, Genovese A, Guardia P, Sottini S, Sangregorio C, Miszta K, Ghosh S, Pellegrino T, Manna L. Copper Sulfide Nanocrystals with Tunable Composition by Reduction of Covellite Nanocrystals with $Cu^{+}$ Ions. *Journal of the American Chemical Society* 2013, 135(46): 17630-17637.

49. Saito S-h, Kishi H, Nié K, Nakamaru H, Wagatsuma F, Shinohara T. $^{63}$Cu NMR studies of copper sulfide. *Physical Review B* 1997, 55(21): 14527-14535.

50. Li B, Xie Y, Xue Y. Controllable Synthesis of CuS Nanostructures from Self-Assembled Precursors with Biomolecule Assistance. *The Journal of Physical Chemistry C* 2007, 111(33): 12181-12187.

51. Liang W, Whangbo MH. Conductivity anisotropy and structural phase transition in Covellite CuS. *Solid State Communications* 1993, 85(5): 405-408.

52. Achimovičová M, Dutková E, Tóthová E, Bujňáková Z, Briančin J, Kitazono S. Structural and optical properties of nanostructured copper sulfide semiconductor synthesized in an industrial mill. *Frontiers of Chemical Science and Engineering* 2019, 13(1): 164-170.

53. Xu W, Liu H, Zhou D, Chen X, Ding N, Song H, Ågren H. Localized surface plasmon resonances in self-doped copper chalcogenide binary nanocrystals and their emerging applications. *Nano Today* 2020, 33: 100892.

54. Luther JM, Jain PK, Ewers T, Alivisatos AP. Localized surface plasmon resonances arising from free carriers in doped quantum dots. *Nature Materials* 2011, 10(5): 361-366.

55. Tian Q, Tang M, Sun Y, Zou R, Chen Z, Zhu M, Yang S, Wang J, Wang J, Hu J. Hydrophilic Flower-Like CuS Superstructures as an Efficient 980 nm Laser-Driven Photothermal Agent for Ablation of Cancer Cells. *Advanced Materials* 2011, 23(31): 3542-3547.

56. Liu X, Li B, Fu F, Xu K, Zou R, Wang Q, Zhang B, Chen Z, Hu J. Facile synthesis of biocompatible cysteine-coated CuS nanoparticles with high photothermal conversion efficiency for cancer therapy. *Dalton Transactions* 2014, 43(30): 11709-11715.

57. Liu X, Fu F, Xu K, Zou R, Yang J, Wang Q, Liu Q, Xiao Z, Hu J. Folic acid-conjugated hollow mesoporous silica/CuS nanocomposites as a difunctional nanoplatform for targeted chemo-photothermal therapy of cancer cells. *Journal of Materials Chemistry B* 2014, 2(33): 5358-5367.

58. Gao W, Sun Y, Cai M, Zhao Y, Cao W, Liu Z, Cui G, Tang B. Copper sulfide nanoparticles as a photothermal switch for TRPV1 signaling to attenuate atherosclerosis. *Nature Communications* 2018, 9(1): 231.

59. Park JY, Kim SJ, Yim K, Dae KS, Lee Y, Dao KP, Park JS, Jeong HB, Chang JH, Seo HK, Ahn CW, Yuk JM. Pulverization-Tolerance and Capacity Recovery of Copper Sulfide for High-Performance Sodium Storage. *Advanced Science* 2019, 6(12): 1900264.

60. Guerrini L, Alvarez-Puebla RA, Pazos-Perez N. Surface Modifications of Nanoparticles for Stability in Biological Fluids. *Materials* 2018, 11(7): 1154.

61. Thomas AG, Syres KL. Adsorption of organic molecules on rutile $TiO_2$ and anatase $TiO_2$ single crystal surfaces. *Chemical Society Reviews* 2012, 41(11): 4207-4217.

62. Du P, Moulijn JA, Mul G. Selective photo(catalytic)-oxidation of cyclohexane: Effect of wavelength and $TiO_2$ structure on product yields. *Journal of Catalysis* 2006, 238(2): 342-352.

63. Nakamura R, Imanishi A, Murakoshi K, Nakato Y. In Situ FTIR Studies of Primary Intermediates of Photocatalytic Reactions on Nanocrystalline $TiO_2$ Films in Contact with Aqueous Solutions. *Journal of the American Chemical Society* 2003, 125(24): 7443-7450.

64. Lagström T, Gmür TA, Quaroni L, Goel A, Brown MA. Surface Vibrational Structure of Colloidal Silica and Its Direct Correlation with Surface Charge Density. *Langmuir* 2015, 31(12): 3621-3626.

65. Barisik M, Atalay S, Beskok A, Qian S. Size Dependent Surface Charge Properties of Silica Nanoparticles. *The Journal of Physical Chemistry C* 2014, 118(4): 1836-1842.

66. Phan HT, Haes AJ. Impacts of pH and Intermolecular Interactions on Surface-Enhanced Raman Scattering Chemical Enhancements. *The Journal of Physical Chemistry C* 2018, 122(26): 14846-14856.

67. Li S, Zhou Q, Chu W, Zhao W, Zheng J. Surface-enhanced Raman scattering behaviour of 4-mercaptophenyl boronic acid on assembled silver nanoparticles. *Physical Chemistry Chemical Physics* 2015, 17(27): 17638-17645.

68. Givens BE, Diklich ND, Fiegel J, Grassian VH. Adsorption of bovine serum albumin on silicon dioxide nanoparticles: Impact of pH on nanoparticle–protein interactions. *Biointerphases* 2017, 12(2): 02D404.

69. Givens BE, Xu Z, Fiegel J, Grassian VH. Bovine serum albumin adsorption on $SiO_2$ and $TiO_2$ nanoparticle surfaces at circumneutral and acidic pH: A tale of two nano-bio surface interactions. *Journal of Colloid and Interface Science* 2017, 493: 334-341.

70. Jayalath S, Larsen SC, Grassian VH. Surface adsorption of Nordic aquatic fulvic acid on amine-functionalized and non-functionalized mesoporous silica nanoparticles. *Environmental Science: Nano* 2018, 5(9): 2162-2171.

71. Jayalath S, Wu H, Larsen SC, Grassian VH. Surface Adsorption of Suwannee River Humic Acid on $TiO_2$ Nanoparticles: A Study of pH and Particle Size. *Langmuir* 2018, 34(9): 3136-3145.

72. Wu H, Gonzalez-Pech NI, Grassian VH. Displacement reactions between environmentally and biologically relevant ligands on $TiO_2$ nanoparticles: insights into the aging of nanoparticles in the environment. *Environmental Science: Nano* 2019, 6(2): 489-504.

73. Xu Z, Grassian VH. Bovine serum albumin adsorption on $TiO_2$ nanoparticle surfaces: Effects of ph and coadsorption of phosphate on protein–surface interactions and protein structure. *The Journal of Physical Chemistry C* 2017, 121(39): 21763-21771.

74. Valko M, Leibfritz D, Moncol J, Cronin MT, Mazur M, Telser J. Free radicals and antioxidants in normal physiological functions and human disease. *Int J Biochem Cell Biol* 2007, 39(1): 44-84.

75. Forkink M, Smeitink JAM, Brock R, Willems PHGM, Koopman WJH. Detection and manipulation of mitochondrial reactive oxygen species in mammalian cells. *Biochimica et Biophysica Acta (BBA) - Bioenergetics* 2010, 1797(6): 1034-1044.

76. Giorgio M, Trinei M, Migliaccio E, Pelicci PG. Hydrogen peroxide: a metabolic by-product or a common mediator of ageing signals? *Nat Rev Mol Cell Biol* 2007, 8(9): 722-728.

77. Panieri E, Santoro MM. ROS homeostasis and metabolism: a dangerous liason in cancer cells. *Cell Death & Disease* 2016, 7(6): e2253-e2253.

78. Bell EL, Klimova TA, Eisenbart J, Schumacker PT, Chandel NS. Mitochondrial Reactive Oxygen Species Trigger Hypoxia-Inducible Factor-Dependent Extension of the Replicative Life Span during Hypoxia. *Molecular and Cellular Biology* 2007, 27(16): 5737.

79. Perillo B, Di Donato M, Pezone A, Di Zazzo E, Giovannelli P, Galasso G, Castoria G, Migliaccio A. ROS in cancer therapy: the bright side of the moon. *Experimental & Molecular Medicine* 2020, 52(2): 192-203.

80. Kim SJ, Kim HS, Seo YR. Understanding of ROS-Inducing Strategy in Anticancer Therapy. *Oxidative Medicine and Cellular Longevity* 2019, 2019: 5381692.

81. Manke A, Wang L, Rojanasakul Y. Mechanisms of Nanoparticle-Induced Oxidative Stress and Toxicity. *BioMed Research International* 2013, 2013: 942916.

82. Abdal Dayem A, Hossain MK, Lee SB, Kim K, Saha SK, Yang G-M, Choi HY, Cho S-G. The Role of Reactive Oxygen Species (ROS) in the Biological Activities of Metallic Nanoparticles. *International journal of molecular sciences* 2017, 18(1): 120.

83. Ancona A, Dumontel B, Garino N, Demarco B, Chatzitheodoridou D, Fazzini W, Engelke H, Cauda V. Lipid-Coated Zinc Oxide Nanoparticles as Innovative ROS-Generators for Photodynamic Therapy in Cancer Cells. *Nanomaterials (Basel, Switzerland)* 2018, 8(3): 143.

84. Fu PP, Xia Q, Hwang H-M, Ray PC, Yu H. Mechanisms of nanotoxicity: Generation of reactive oxygen species. *Journal of Food and Drug Analysis* 2014, 22(1): 64-75.

Chapter 2 Experimental Methods and Techniques

A variety of techniques were employed for the research presented in this dissertation. These include basic structural characterization (e.g. surface area, crystalline structure), *in- situ* vibrational spectroscopy, electron microscopy, surface sensitive spectroscopy, and quartz crystal microbalance with dissipation. In addition, two-dimensional correlation spectroscopy (2DCOS) was also conducted to further analyze the infrared data and to understand ligand displacement processes. Experimental details of each of these methods and analyses are given below.

## 2.1. ATR–FTIR Spectroscopy

Reflection Infrared (IR) spectroscopy is developed by combining conventional transmittance IR spectroscopy with reflection theories.[1] Reflection IR spectroscopy can be employed for samples that are difficult to measure with conventional transmission Fourier

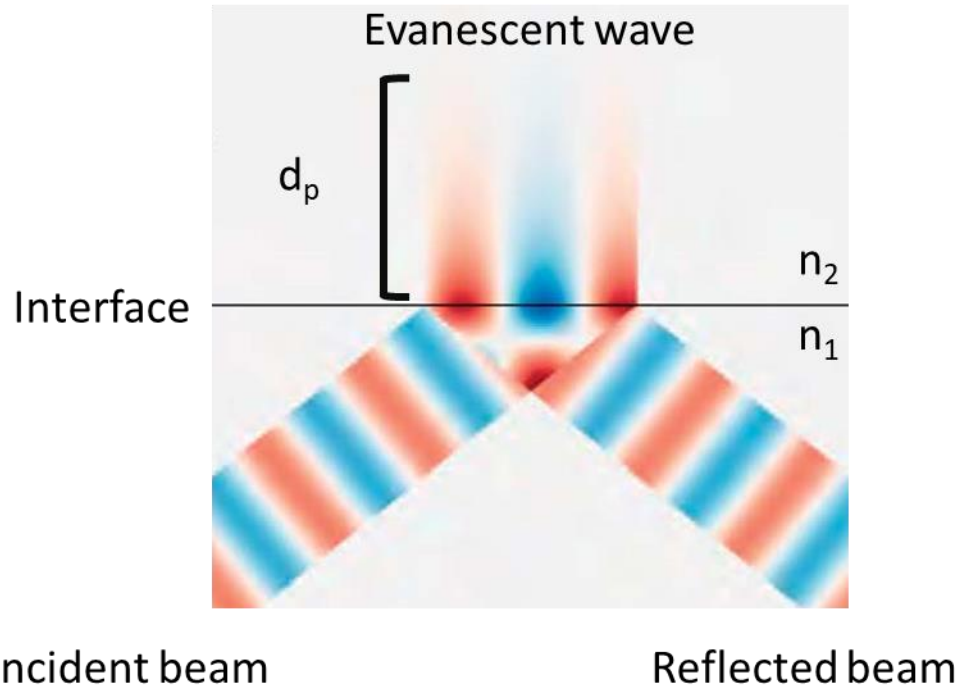


**Figure 2.1** Electromagnetic wave reflection depicting the evanescent wave near the interface in an internal reflection element. (Reprinted and modified from Ref 2 with permission from Royal Society of Chemistry)

transform IR (FTIR) spectroscopy. One of the main internal reflection spectroscopic techniques is Attenuated Total Reflectance Fourier Transform Infrared (ATR–FTIR) spectroscopy. ATR–FTIR is developed based on the total internal reflection phenomenon that occurs at an interface when a light beam propagates from a medium of high refractive index ($n_1$, optically denser medium) to a medium of low refractive index ($n_2$, optically rarer medium). For total internal reflection to occur, the incidence angle of the infrared beam must be greater than the critical angle.

The reflection of the propagating beam at the boundary between the two media generates an evanescent electric field in the direction perpendicular to the interface as illustrated in Figure 2.1.[2] The electric field amplitude exponentially decays with distance from the interface, as shown in Equation.2.1:

$$\boldsymbol{E = E_0 e^{-z/d_p}} \qquad (\mathbf{2.1})$$

where E represents the electric field amplitude of the evanescent wave, $E_0$ is the electric field amplitude at the interface, z is the distance from the interface, and $d_p$ is the depth of penetration. It is useful to note that the penetration depth is not constant but dependent on the incident wavelengths of the beam and the refractive indices of the interfacial media (as shown by Equation 2.2):

$$\boldsymbol{d_p = \frac{\lambda}{2\pi\left(n_1^2 sin^2\theta - n_2^2\right)^{1/2}} = \frac{\lambda_1}{2\pi\left(sin^2\theta - n_{21}^2\right)^{1/2}}} \qquad (\mathbf{2.2})$$

where λ is the incident light wavelength, $n_1$ is the refractive index of the denser medium, $n_2$ is the refractive index of rarer medium, $n_{21}$ is the relative index of refraction, and θ is the incident angle which is greater than the critical angle. ATR spectra are obtained by measuring absorption of the evanescent wave from IR active moieties in the interfacial region. This feature of ATR makes it a

more sensitive technique than conventional transmittance FTIR to probe the interfacial region even in the presence of strong absorbing solvents, like water. Therefore, *in-situ* ATR–FTIR can be applied to examine adsorption kinetics and molecular structural change associated with adsorption.

In addition to qualitative analysis, ATR–FTIR also offers semi-quantitative information. Reflections in the internal reflecting element can be single bounce or multi-bounce. The relationship between absorbance and interfacial concentrations follows Beer's law. The modified Beer's law for quantitative ATR–FTIR is shown below in Equation 2.3:

$$\mathbf{A} = -\log \boldsymbol{R} = \boldsymbol{\varepsilon} \mathbf{n} \boldsymbol{d_e} \mathbf{c} \qquad (\mathbf{2.3})$$

where R is reflectivity of ATR, ε is the molar absorption coefficient, n is the number of active internal reflections in the reflection element (for multi-bounce ATR) and $d_e$ is the effective evanescent wave penetration depth. For practical applications of analyzing molecules on nanoparticles (NPs), a film of NPs is placed on an ATR element (which is ~1-2 μm thick). The effective penetration depth in this case is (Equation 2.4):[3, 4]

$$\boldsymbol{d_e} = \frac{\boldsymbol{n_{21} d_p}}{\boldsymbol{2 cos\, \theta}} \left( \boldsymbol{e}^{-2z_1/d_p} - \boldsymbol{e}^{-2z_2/d_p} \right) (\boldsymbol{E_{02}^r})^2 \qquad (\mathbf{2.4})$$

where $z_1$ and $z_2$ are two distances from the interface of ATR element, $\boldsymbol{E_{02}^r}$ is the relative electric field amplitude at z = 0 in medium 2.

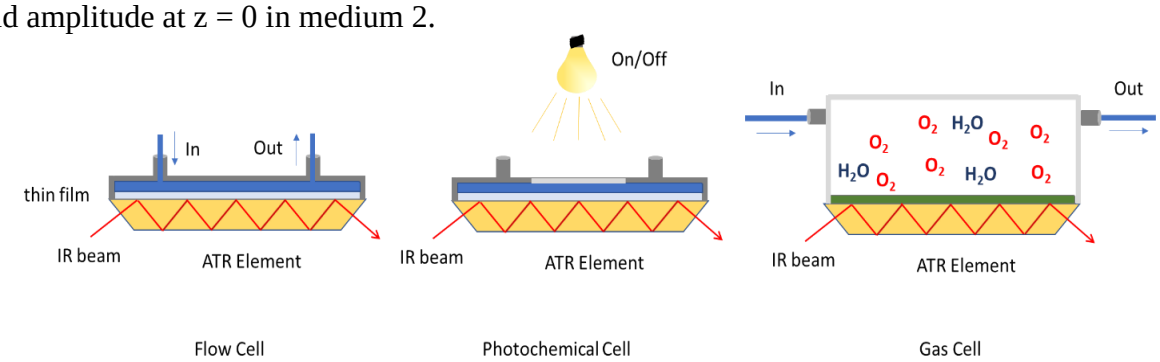


**Figure 2.2** Schematic of various ATR-FTIR experimental setups.

The ATR–FTIR experimental setup used in this dissertation is shown in Figure 2.2. This setup is based on a flow cell ATR crystal and is modified by using different flow cell covers for different studies. Adsorption and displacement reactions were carried out in a flow cell. The cover used for photochemical reactions was modified with a quartz window in the middle of the cover to allow the light to reach the film surface. For gas phase reactions, the cover was specially designed with Teflon material and a directly connected humidity sensor to *in-situ* monitor RH during the reaction. The gases used for this research were ultrahigh purity $O_2$ and $N_2$. The RH was controlled by adjusting the ratios of humid gas and dry gas. The schematic of the setup is shown in Figure 2.3. In this work, an AMTIR (amorphous material transmitting IR radiation) crystal was chosen because it possesses high chemical resistance in acidic and neutral environments and a good depth of penetration compared to other popular materials for ATR such as ZnSe and Ge.

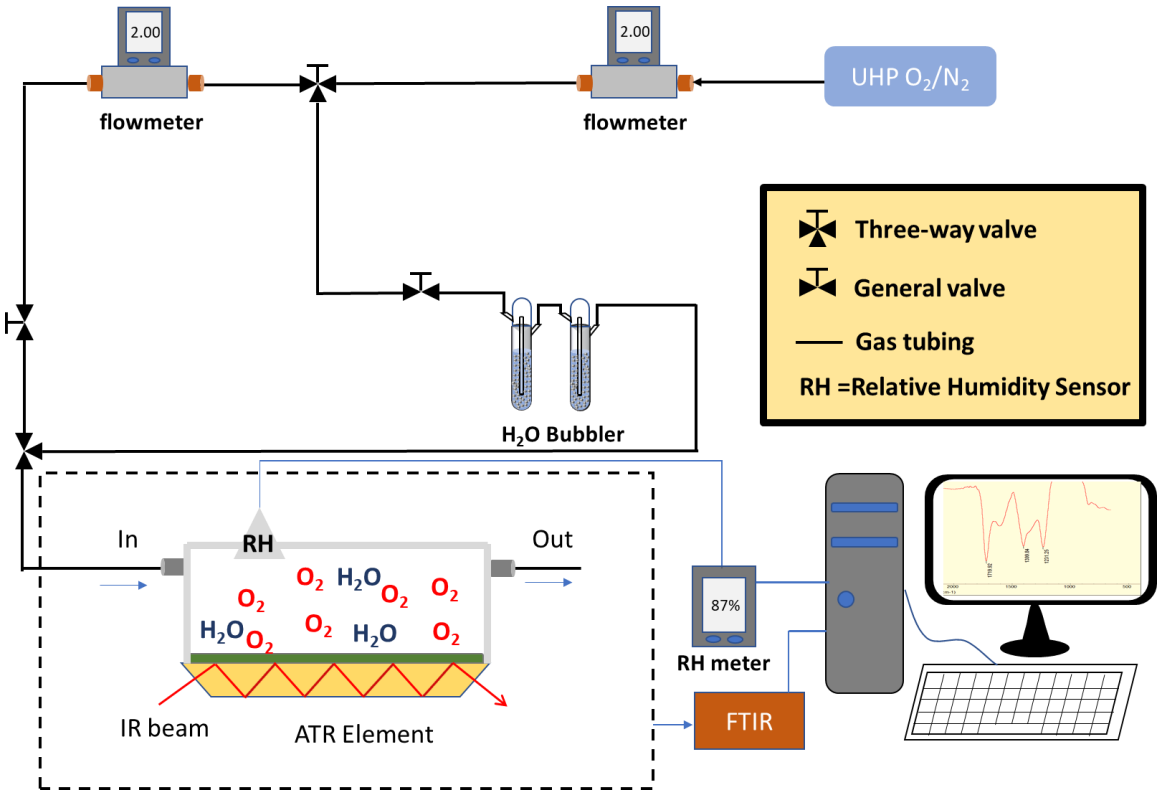


**Figure 2.3** Schematic of the ATR-FTIR and gas flow experimental setup used for CuS oxidation.

## 2.2. Two-Dimensional Correlation Spectroscopy

Two-Dimensional Correlation Spectroscopy (2DCOS) has been well characterized as an analytical method used to study changes induced by external perturbations such as temperature, surface reactions, pH, and concentration.[5-8] In typical 1D spectroscopic experiments, an electromagnetic probe is used to investigate the interaction of the probe and system. However, once an external perturbation is used to stimulate the system, spectral intensity changes can occur. 2DCOS is a way of analyzing spectra to determine whether intensity fluctuations are correlated and to determine the sequence of spectral changes. These transient spectral fluctuations are called dynamic spectra $\tilde{\boldsymbol{y}}(\boldsymbol{v},\boldsymbol{t})$ and is defined by Equations 2.5 and 2.6:

$$\tilde{\boldsymbol{y}}(\boldsymbol{v},\boldsymbol{t}) = \begin{cases} \boldsymbol{y}(\boldsymbol{v},\boldsymbol{t}) - \bar{\boldsymbol{y}}(\boldsymbol{v}), & \boldsymbol{T_{min}} \leq \boldsymbol{t} \leq \boldsymbol{T_{max}} \\ \mathbf{0}, & \boldsymbol{otherwise} \end{cases} \tag{2.5}$$

$$\bar{\boldsymbol{y}}(\boldsymbol{v}) = \frac{\mathbf{1}}{\boldsymbol{T_{max}} - \boldsymbol{T_{min}}} \int_{\boldsymbol{T_{min}}}^{\boldsymbol{T_{max}}} \boldsymbol{y}(\boldsymbol{v},\boldsymbol{t})\mathbf{dt} \tag{2.6}$$

where $\boldsymbol{v}$ is the spectral variable (wavenumber in FTIR spectra) and t is the perturbation variable. $\bar{\boldsymbol{y}}(\boldsymbol{v})$ is considered the reference spectrum which could be the initial state before perturbation but is customary to be equal to the averaged spectrum.

2D-COS can be thought of as a quantitative intensity comparison of two spectra between some perturbation interval. This is a way to visualize how similar or dissimilar the correlation between intensity fluctuations are. The similarity between two spectra as the perturbation variable is changed, is measured by the synchronous spectrum, $\boldsymbol{\Phi}(\boldsymbol{v_1},\boldsymbol{v_2})$. Likewise, the out-of-phase or dissimilarity between two spectra is measured by the asynchronous spectrum, $\boldsymbol{\Psi}(\boldsymbol{v_1},\boldsymbol{v_2})$. For a set of m equally spaced spectra between the interval of $T_{min}$ and $T_{max}$, along the perturbation variable t, the synchronous and asynchronous 2D correlations are given by Equations 2.7-2.9:

$$\boldsymbol{\Phi}(\boldsymbol{v_1}, \boldsymbol{v_2}) = \frac{\mathbf{1}}{\boldsymbol{m} - \mathbf{1}} \tilde{\boldsymbol{y}}(\boldsymbol{v_1})^{\mathsf{T}} \tilde{\boldsymbol{y}}(\boldsymbol{v_2}) \tag{2.7}$$

$$\boldsymbol{\Psi}(\boldsymbol{v_1}, \boldsymbol{v_2}) = \frac{\mathbf{1}}{\boldsymbol{m} - \mathbf{1}} \tilde{\boldsymbol{y}}(\boldsymbol{v_1})^{\mathsf{T}} \boldsymbol{N_{ij}} \tilde{\boldsymbol{y}}(\boldsymbol{v_2}) \tag{2.8}$$

$$\tilde{\boldsymbol{y}}\,(\boldsymbol{v}) = \begin{bmatrix} \boldsymbol{y}\,(\boldsymbol{v}, \boldsymbol{t_1}) \\ \boldsymbol{y}\,(\boldsymbol{v}, \boldsymbol{t_2}) \\ \vdots \\ \boldsymbol{y}\,(\boldsymbol{v}, \boldsymbol{t_m}) \end{bmatrix} \tag{2.9}$$

The $N_{ij}$ term refers to the ith row and jth column element in the Hilbert-Noda transformation matrix ($N_{ij}$) which is defined by Equation 2.10:

$$\mathbf{N_{ij}} = \begin{cases} \mathbf{0} & , \ \boldsymbol{if\ i = j} \\ \frac{\mathbf{1}}{\boldsymbol{\pi(j-i)}}, & \boldsymbol{otherwise} \end{cases} \tag{2.10}$$

The synchronous and asynchronous correlation maps can be analyzed by following Noda's rules. If $\boldsymbol{\Phi}(\boldsymbol{v_1}, \boldsymbol{v_2})$ is positive, then $\nu_1$ and $\nu_2$ intensity values are changing in the same direction, whether increasing or decreasing. On the other hand, if $\boldsymbol{\Phi}(\boldsymbol{v_1}, \boldsymbol{v_2})$ is negative, then $\nu_1$ and $\nu_2$ intensity values are changing in opposite directions, i.e. one is increasing and the other decreasing. The sequential order spectral variations can be determined by the signs of both asynchronous and synchronous correlation maps. If $\boldsymbol{\Phi}(\boldsymbol{v_1}, \boldsymbol{v_2})$ and $\boldsymbol{\Psi}(\boldsymbol{v_1}, \boldsymbol{v_2})$ are the same, the change to $\nu_1$ occurs before changes to $\nu_2$. If the signs are negative, then the change to $\nu_1$ occurs after changes to $\nu_2$. If there is a zero value for the correlation map, then there the bands have no correlation. Recently, FTIR generalized 2DCOS experiments have been used investigate metal oxide surface interactions such as oxyanion adsorption,[9, 10] protein conformational change,[5, 11-13] and displacement reactions.[6]

## 2.3. Quartz Crystal Microbalance with Dissipation Monitoring

Quartz Crystal Microbalance with Dissipation monitoring (QCM-D) is based on the converse piezoelectric effect that a material is able to generate internal stress in response to an

externally applied electric field.[14] A QCM sensor (shown in Figure 2.4a) is composed of a piece of quartz disc coated by a pair of metal electrodes on the top and bottom. When an electric field is applied to the quartz disc, it will oscillate at its resonance frequency. The resonance frequency of the sensor is related to the total oscillating mass including adsorbed molecules. QCM measures the change in frequency of the quartz crystal resonator when molecules are adsorbed compared to the initial state. The adsorbed mass for a rigid surface has a relationship with the change of frequency which is described by the Sauerbrey relationship (Equation 2.11):[15]

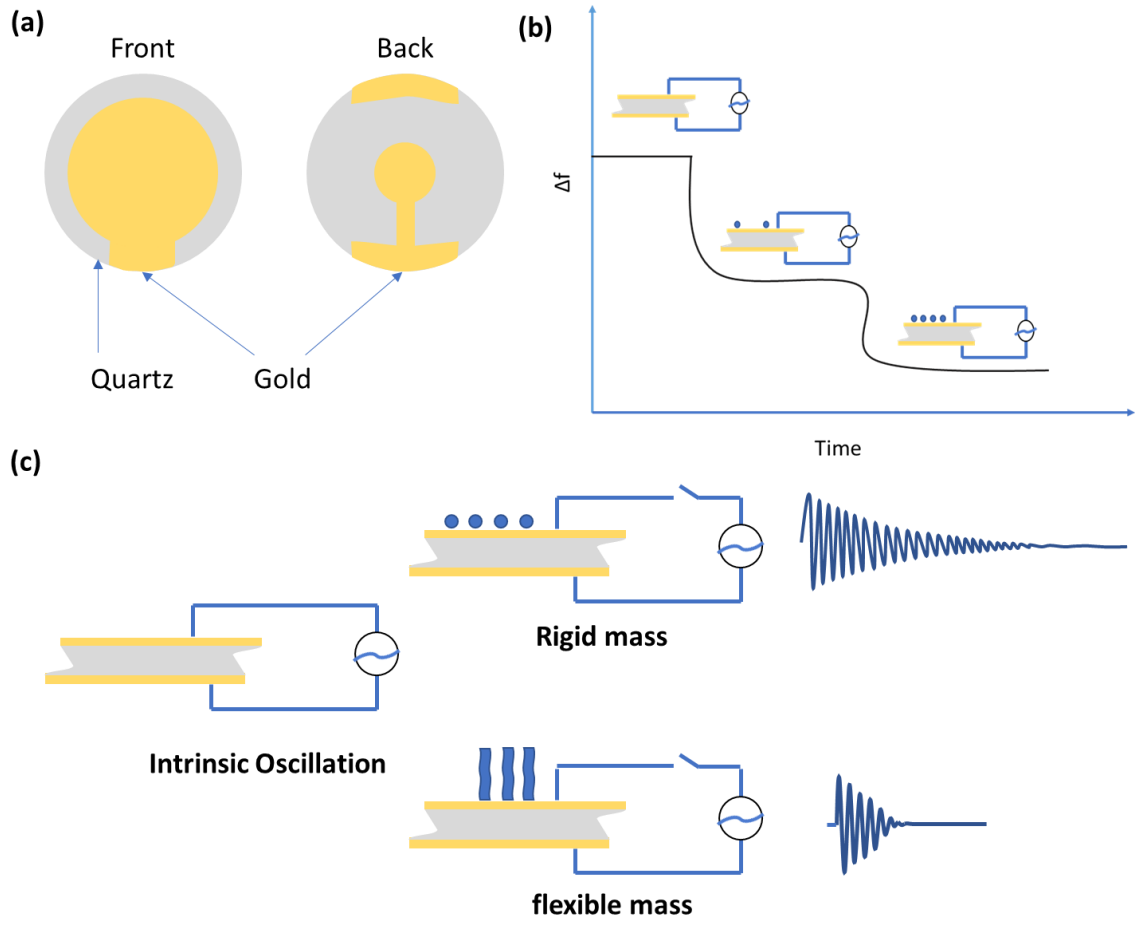


**Figure 2.4** (a) common design for a quartz crystal gold electrode for QCM, (b) a diagram depicts frequency change with mass gain on the electrode surface, (c) Frequency and amplitudes for quartz oscillations with different types of adsorbates. (Reprinted and modified from Ref 17 with permission from Royal Society of Chemistry)

$$\boldsymbol{\Delta m} = -\boldsymbol{C} \times \frac{\Delta \boldsymbol{f}}{\boldsymbol{n}} \qquad (\mathbf{2.11})$$

where $\boldsymbol{\Delta m}$ is adsorbed mass, C is the mass sensitivity constant related to the properties of quartz (usually 17.7 ng/(cm$^2$•Hz) for 5 MHz crystal), $\Delta \boldsymbol{f}$ is the change of frequency, and n is the overtone number. The Sauerbrey relationship fails to describe the mass gain for a viscoelastic or soft film. Dissipation of oscillation energy on a soft surface becomes more evident than on a rigid surface.[16] Dissipation is expressed by Equation 2.12:

$$\mathbf{D} = \frac{\boldsymbol{E_{lost}}}{\mathbf{2}\boldsymbol{\pi} \times \boldsymbol{E_{stored}}} \qquad (\mathbf{2.12})$$

where $E_{lost}$ is the energy lost during one oscillation cycle and $E_{stored}$ is the total energy stored in the oscillator. In the operation of QCM-D, the applied electric field is shut off, and the energy of the oscillator decays as a function of time as described by Equation 2.13:[17, 18]

$$\boldsymbol{A(t)} = \boldsymbol{A_0 e^{-\frac{t}{\tau}}} \mathbf{sin}(\mathbf{2}\boldsymbol{\pi f t} + \boldsymbol{\varphi}) \qquad (\mathbf{2.13})$$

where A is the amplitude, τ is the decay time constant, f is the frequency and φ is the phase. The dissipation factor, D, is related to the decay time constant by Equation 2.14:[17, 18]

$$\boldsymbol{D} = \frac{\mathbf{1}}{\boldsymbol{\pi f} \boldsymbol{\tau}} \qquad (\mathbf{2.14})$$

As indicated by the equations above, soft or viscoelastic surface would have greater dissipation than a rigid surface. Previous studies have shown that the dissipation energy is able to reflect intermolecular interactions and conformational changes for large and biological molecules.[19, 20]

## 2.4. Electron Microscopy

### 2.4.1 Transmission Electron Microscopy

Transmission Electron Microscopy (TEM) is a powerful tool for the analysis and characterization of nanomaterials. In TEM, an electron beam is accelerated stepwise by high voltage electric fields and transmitted through a specimen. In this work, TEM was used to image nanoparticles and analyze the d spacing of the crystalline material. For TEM analysis, the preparation of samples would vary. For $TiO_2$, a dilute suspension of $TiO_2$ NPs in water was sonicated for 10 minutes and a droplet was cast on carbon-coated Cu grids. CuS NPs after oxidation were prepared in a different way. In this case, the dry powder sample was first placed on the grid and a few drops of ethanol were used to flush the excess powder. The grid was then immediately transferred to a vial filled with inert gas. Once completely dry, the sample grid was sent for TEM analysis. The acquired TEM images were processed by DigitalMicrograph and ImageJ software for the further analysis, such as lattice spacing measurement, FFT pattern etc.

### 2.4.2 Scanning Electron Microscopy

Scanning Electron Microscopy (SEM) is another imaging technique with a focused beam of electrons scanning the surface. The signals from the interaction of the electrons and sample surface include secondary electrons, backscattered electrons, diffracted backscattered electrons, X-ray photons etc. Secondary electrons and backscattered electrons are mostly used for imaging.[21] The energy of secondary electrons is usually lower than 50 eV so that the mean free path is limited in solid matter.[22] As a result, the secondary electrons can only escape from the sample surface. SEM combined with other detectors has become a very useful tool for nanoscience and material science. For this work, SEM was primarily used to image the profile of thin films made of $TiO_2$ NPs. As discussed in previous section, the thickness of a film is crucial for ATR–FTIR to understand the interaction and adsorption of molecules on the NP surface. To prepare a film, 1 mL

of a 1 mg/mL $TiO_2$ NP suspension was cast onto the ATR element to dry (the density of the $TiO_2$ NP film is 0.13 mg/cm$^2$ on a 7.5*1 cm ATR element). To simulate a film on an ATR element, 32 μL of a 1 mg/mL $TiO_2$ suspension was placed on a 0.5*0.5 cm silicon wafer to dry. The sample was mounted on a cross-section sample holder to image the thickness of the film. In addition to traditional SEM, focused ion beam SEM (FIB-SEM) was also employed, the results of which corroborated SEM results, namely, the thickness of a film is around 1 μm as shown in Figure 2.5.

## 2.5.X-ray Photoelectron Spectroscopy

X-ray Photoelectron Spectroscopy (XPS) is a surface sensitive technique that measures the kinetic energy of photoelectrons induced by incident x-ray photons. Electron binding energy can be determined by photoelectron kinetic energy as described by Equation 2.15:

$$\mathbf{E_{binding} = E_{photon} - (E_{kinetc} + \Phi)} \qquad (\mathbf{2.15})$$

where $\mathbf{E_{binding}}$ is the binding energy (BE) of the electron, $\mathbf{E_{photon}}$ is the energy of the x-ray photons, $\mathbf{E_{kinetc}}$ is the measured kinetic energy of photoelectrons and $\mathbf{\Phi}$ is the work function of the material and the instrument. The binding energy is subject to the oxidation state of the atoms and the local chemical and physical environment. Thus, XPS can be used qualitatively and semi-quantitatively to analyze surface states and chemical bonding. In this work, XPS was used to analyze the surface oxidation states of CuS NPs before and after oxidation reactions. The CuS NP powder was placed on a silicon wafer (pre-cleaned by ethanol and acid). The samples were then kept in vacuum desiccator before mounting on XPS sample holders.

## 2.6. Nanoparticle Characterization

2.6.1 Powder X-ray Diffraction Spectrometry

In powder X-ray diffraction spectrometry, incident X-ray waves interact with an atom resulting in electronic cloud movement. This movement then re-radiates the same frequency waves, called elastic scattering. These diffracted waves can interfere to produce a diffraction maximum at certain incident angles. The lattice planes separated by the interplanar distance, d, in a solid has a relationship with the incident angle given by Bragg's law (Equation 2.16):

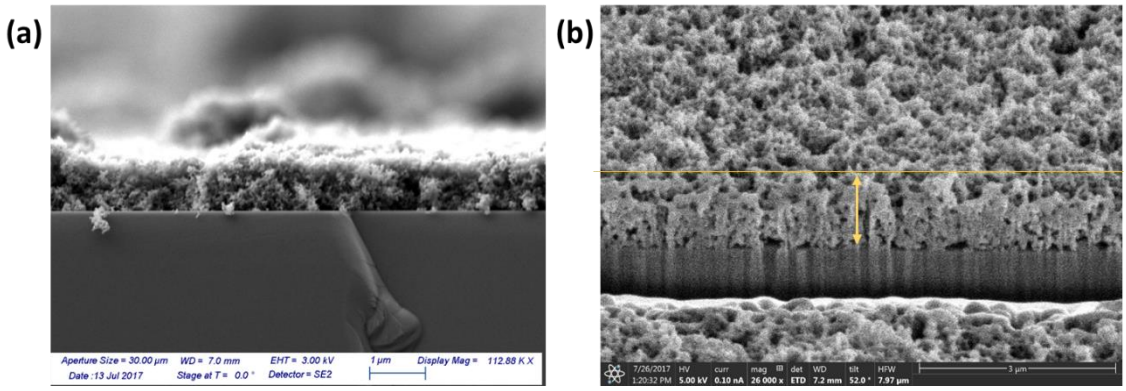


**Figure 2.5** (a) cross-sectional SEM image for a $TiO_2$ NP film, (b) FIB-SEM image of a $TiO_2$ NP film.

$$\boldsymbol{2dsin\theta = n\lambda} \qquad (\mathbf{2.16})$$

where $\boldsymbol{\theta}$ is the incident angle, $\boldsymbol{\lambda}$ is the wavelength of the incident wave and n is a positive integer representing the order of the diffraction. The crystalline phases of nanoparticles in this dissertation were characterized by Powder X-ray Diffraction (PXRD).

2.6.2. Specific Surface Area Analysis

Specific surface area (SSA) is an important parameter for nanomaterials. In this work, the SSA was calculated by Brunauer-Emmett-Teller (BET) theory. SSA of NP dry powders was analyzed using a Quantachrome Nova 4200e surface analyzer. Clean and dry sample tubes were weighed prior to adding any sample. Then, a certain mass of NP powder was placed in the bulb of the glass sample tube and vacuum-degassed at 120℃ for 8 hours to remove any pre-adsorbed

molecules on the sample surface. After degassing, the total mass (sample and tube) were measured. The accurate mass of the sample was obtained by subtracting the tube mass from the total mass.

Next, a total 20-point $N_2$ adsorption-desorption isotherm was acquired in the relative pressure range of 0.05-0.99 in a liquid nitrogen bath at 77.3 K. The specific surface area ($m^2/g$) was determined based on the BET equations shown below (Equations 2.17-2.19):[23]

$$\frac{1}{v\left[\left({P_0}/{P}\right)-1\right]}=\frac{1}{v_m C}+\frac{C-1}{v_m C}\left(\frac{P}{P_0}\right) \tag{2.17}$$

$$S_{total}=\frac{(v_m N s)}{V} \tag{2.18}$$

$$S_{BET}=\frac{S_{total}}{m} \tag{2.19}$$

ν is the quantity of adsorbed $N_2$ molecules, $\nu_m$ is the monolayer adsorbed quantity, C is the BET constant, P and $P_0$ are the equilibrium and saturation pressure, $S_{total}$ is the total surface area, $S_{BET}$ is the specific surface area, N is Avogadro's number, s is the adsorption cross section of $N_2$, V is the molar volume of $N_2$ and m represents sample mass.

## 2.7. Acknowledgements

Chapter II, in part, is currently being prepared for submission for publication of the material: Haibin Wu, Izaac Sit, Vicki H. Grassian. The dissertation author was the co-first author of this paper.

2.8 References


1. Larkin P. Chapter 5 - Origin of Group Frequencies. In: Larkin P (ed). *Infrared and Raman Spectroscopy*. Elsevier: Oxford, 2011, pp 63-72.

2. Woods DA, Bain CD. Total internal reflection spectroscopy for studying soft matter. *Soft Matter* 2014, 10(8): 1071-1096.

3. *Internal Reflection Spectroscopy: Theory and Applications*. MARCEL DEKKER, INC: New York, 1992.

4. Hug SJ, Sulzberger B. In situ Fourier Transform Infrared Spectroscopic Evidence for the Formation of Several Different Surface Complexes of Oxalate on $TiO_2$ in the Aqueous Phase. *Langmuir* 1994, 10(10): 3587-3597.

5. Sit I, Xu Z, Grassian VH. Plasma protein adsorption on TiO2 nanoparticles: Impact of surface adsorption on temperature-dependent structural changes. *Polyhedron* 2019, 171: 147-154.

6. Wu H, Gonzalez-Pech NI, Grassian VH. Displacement reactions between environmentally and biologically relevant ligands on $TiO_2$ nanoparticles: insights into the aging of nanoparticles in the environment. *Environmental Science: Nano* 2019, 6(2): 489-504.

7. Chen W, Qian C, Liu X-Y, Yu H-Q. Two-Dimensional Correlation Spectroscopic Analysis on the Interaction between Humic Acids and $TiO_2$ Nanoparticles. *Environmental Science & Technology* 2014, 48(19): 11119-11126.

8. Jin P, Song J, Wang XC, Jin X. Two-dimensional correlation spectroscopic analysis on the interaction between humic acids and aluminum coagulant. *Journal of Environmental Sciences* 2018, 64: 181-189.

9. Liu J, Zhu R, Liang X, Ma L, Lin X, Zhu J, He H, Parker SC, Molinari M. Synergistic adsorption of Cd(II) with sulfate/phosphate on ferrihydrite: An in situ ATR–FTIR /2D-COS study. *Chemical Geology* 2018, 477: 12-21.

10. Han J, Ro H-M. Characterizing Preferential Adsorption of Phosphate on Binary Sorbents of Goethite and Maghaemite using in situ ATR–FTIR and 2D Correlation Spectroscopy. *Scientific Reports* 2019, 9(1): 6130.

11. Gomaa AI, Sedman J, Ismail AA. An investigation of the effect of microwave treatment on the structure and unfolding pathways of β-lactoglobulin using FTIR spectroscopy with

the application of two-dimensional correlation spectroscopy (2D-COS). *Vibrational Spectroscopy* 2013, 65: 101-109.

12. Schmidt MP, Martínez CE. Kinetic and conformational insights of protein adsorption onto montmorillonite revealed using in situ ATR–FTIR /2D-COS. *Langmuir* 2016, 32(31): 7719-7729.

13. Liu F, Li X, Sheng A, Shang J, Wang Z, Liu J. Kinetics and Mechanisms of Protein Adsorption and Conformational Change on Hematite Particles. *Environmental Science & Technology* 2019, 53(17): 10157-10165.

14. Ward MD, Buttry DA. In Situ Interfacial Mass Detection with Piezoelectric Transducers. *Science* 1990, 249(4972): 1000.

15. Sauerbrey G. Verwendung von Schwingquarzen zur Wägung dünner Schichten und zur Mikrowägung. *Zeitschrift fur Physik* 1959, 155(2): 206-222.

16. Sohna Sohna JE, Cooper MA. Does the Sauerbrey equation hold true for binding of peptides and globular proteins to a QCM?: A systematic study of mass dependence of peptide and protein binding with a piezoelectric sensor. *Sensing and Bio-Sensing Research* 2016, 11: 71-77.

17. Rodahl M, Kasemo B. A simple setup to simultaneously measure the resonant frequency and the absolute dissipation factor of a quartz crystal microbalance. *Review of Scientific Instruments* 1996, 67(9): 3238-3241.

18. Surface Plasmon Resonance and Quartz Crystal Microbalance Methods for Detection of Molecular Interactions. *Chemosensors*, pp 329-344.

19. Zhang B, Wang Q. Quartz crystal microbalance with dissipation. *Nanotechnology research methods for foods and bioproducts*. Wiley-Blackwell, 2012, pp 181-194.

20. Sun L, Frykholm K, Fornander LH, Svedhem S, Westerlund F, Åkerman B. Sensing Conformational Changes in DNA upon Ligand Binding Using QCM-D. Polyamine Condensation and Rad51 Extension of DNA Layers. *The Journal of Physical Chemistry B* 2014, 118(41): 11895-11904.

21. Principles of SEM. *Principles and Practice of Variable Pressure/Environmental Scanning Electron Microscopy (VP -ESEM)*, pp 17-62.

22. Modinos A. Secondary Electron Emission Spectroscopy. *Field, Thermionic, and Secondary Electron Emission Spectroscopy*. Springer US: Boston, MA, 1984, pp 327-345.

23. Brunauer S, Emmett PH, Teller E. Adsorption of Gases in Multimolecular Layers. *Journal of the American Chemical Society* 1938, 60(2): 309-319.

# Chapter 3 Displacement Reactions Between Environmentally and Biologically Relevant Ligands on $TiO_2$ Nanoparticles: Insights into the Aging of Nanoparticles in the Environment

## 3.1 Abstract

Coatings on nanoparticle (NP) surfaces play a key role in dictating their behavior in the environment. For metal oxide NPs, the physicochemical processes of dissolution, aggregation, and reactivity are all impacted by surface coatings. The current study focuses on adsorption and displacement reactions of different molecular and biological species representative of different coatings on $TiO_2$ NP surfaces. These different species include ascorbic acid (AA), citric acid (CA), humic acid (HA) and bovine serum albumin (BSA) protein. Surface adsorption, desorption, and displacement reactions of these four species on 20 nm $TiO_2$ NPs were investigated using attenuated total reflectance–Fourier transform infrared spectroscopy. Further insights of these reactions and on the behavior of $TiO_2$ with these coatings were gained from quartz crystal microbalance with dissipation measurements, dynamic light scattering and sedimentation studies to investigate nanoparticle stability. Our results show that HA adsorbs strongly onto $TiO_2$ NP surfaces at neutral pH. In contrast, smaller acidic molecules such as AA and CA bind more weakly and, as a result, HA can displace these molecules from the $TiO_2$ surface as determined by two-dimensional correlation spectroscopy. In the case of BSA, HA does not displace the protein but instead co-adsorbs on the nanoparticle surface. Our results show that the relative binding affinity to the surface depends on the ability of different functional groups to interact with the surface and through non-specific surface interactions that become important for larger species with higher molar mass. To our knowledge, this is the first time that these types of displacement reactions on $TiO_2$ NPs have been investigated and probed with *in situ* techniques. The insights that this work provide are of relevance in understanding the fate of nanomaterials as ligand displacement

reactions will modify the stability of these nanoparticles during their transport in the environment, nanoparticle agglomeration and their interactions with biological systems.

## 3.2 Introduction

Metal oxide nanomaterials and their composites have been extensively studied and developed, due to their vast potential applications as photocatalysts,[1, 2] solar cells,[3] biosensors,[4] diagnostic,[5] and drug delivery.[6, 7] Because of these developments, it is expected that these nanomaterials will be released into the environment.[8] Once in the environment, nanomaterials will undergo a variety of different aging and transformation processes, involving reactivity, dissolution, and both hetero- and homo- agglomeration, thus altering the properties of the nanomaterials over time.[9-14] Among various metal oxide nanomaterials, $TiO_2$-based products are some of the most widely used,[15] due to their unique photocatalytic properties[16-18] and biocompatibility.[19-23] However, modeling studies have indicated that an increased concentration of nanomaterials in the environment can create potential risks to various organisms.[24-27] Therefore, the fate of $TiO_2$ NPs in the environment has attracted much attention over the past decade. Several factors play a role in the fate of nanomaterials with the surface being an important one due to surface functionalization and surface ligand reactions.[28-31]

Natural organic matter (NOM) is expected to adsorb onto $TiO_2$ NPs released into the environment, and impact their agglomeration and stability,[32-36] thus affecting the mobility of $TiO_2$ NPs.[37] Humic acid (HA) is used as a typical model for NOM as it is widely distributed in soil, sediments, and water in the environment with concentrations that vary from 0.1 to 50 mg/L.[38] HA refers to a category of natural substances derived from the decomposition of plants and animals. HA is a collection of large macromolecular structures with high aromatic conjugated structures containing amino, hydroxyl, ketone, phenolic, and carboxylic functional groups.[39] Previous studies

of metal-HA interactions show that HA can bind metal ions.[40, 41] Among the different interaction mechanisms by which NOM adsorbs on NPs, surface ligand exchange between NP surface and a variety of groups of NOM is the dominant interaction.[42] This interaction has two main steps:[43] (1) the outer-sphere complexation between polar functional groups and surface hydroxyl group, and (2) the ligand exchange resulting in formation of an inner-sphere complex. The spectroscopic studies suggest that the adsorption of HA on $TiO_2$ NPs involves various functional groups, such as phenol and carboxyl groups.[44, 45] In addition, the adsorption process is significantly modified by the pH: the hydroxyl groups on the surface are protonated favoring ligand exchange.[42, 44] Furthermore, studies have shown that interactions between NOM or HA have significant impacts on the properties of NPs, such as chemical reactivity,[46, 47] dissolution,[48] and toxicity.[49] HA as a surface ligand can significantly influence the fate and properties of nanomaterials in the environment.

Attenuated total reflectance–Fourier transform infrared (ATR–FTIR) spectroscopy allows the *in-situ* monitoring of adsorbed species by measuring spectral changes during the adsorption of ligands onto surfaces. Although adsorption of ligands on nanomaterials has been intensively studied by this technique,[44, 50-55] most of these studies focus on the adsorption processes on hydroxylated $TiO_2$ NPs surface. However, $TiO_2$ NPs are often coated by ligands because surfactants and surface ligands are used in the wet chemical synthesis of nanomaterials. As such, it is expected that the released $TiO_2$ NPs in the environment undergo diverse surface ligand reactions, especially ligand displacement reactions. It is crucial to understand the displacement reactions that $TiO_2$ NPs may undergo in the environment, since surface coatings can significantly affect the physiochemical properties. Nevertheless, there are few reports about mechanisms of displacement reactions and the impact of these reactions on the fate of $TiO_2$ NPs. Herein, ATR–

FTIR spectroscopy is used to explore the mechanism of displacement reactions between environmentally and biologically relevant ligands including ascorbic acid (AA), citric acid (CA), and bovine serum albumin (BSA) by HA. AA and CA were selected due to their common use as molecular coatings.[56] Moreover, they are also found in various biologically relevant systems with different concentrations (e.g. 0.1 mM CA in blood plasma[52] and 40 – 770 mg/kg AA in fruits[57]). BSA is used as a model of human serum albumin (typical concentration in blood is 3.5-5 g/dL)[58] and other proteins that NPs interact with in the environment.[59] In order to get a better understanding of the effect of NOM on $TiO_2$ NPs in the environment, HA is chosen as a model to show how NOM displacement reactions may impact NP surfaces and NP sedimentation behavior.

## 3.3 Experimental Methods

### 3.3.1 ATR–FTIR Spectroscopy

ATR–FTIR spectra were recorded using a 500 µl horizontal ATR flow cell with an AMTIR window (Pike Technologies Inc.) in a Nicolet iS 10 FTIR spectrometer equipped with an MCT-A detector. Spectra were collected with 264 scans at an instrument resolution of 4 $cm^{-1}$ in the AMTIR window range (750 to 4000 $cm^{-1}$). In order to control pH, all solutions were prepared by dissolving the corresponding solutes (e.g. AA, CA, HA, and BSA) in 25 mM 4-(2-hydroxyethyl)-1-piperazineethanesulfonic acid (HEPES, Fisher Scientific) buffered solutions. Unless otherwise indicated, all solutions contain HEPES to maintain a pH of 7.5.

Solution phase spectra were collected for 100 mM citric acid (CA), 100 mM ascorbic acid (AA), 10 g/L bovine serum albumin (BSA) and 1 g/L humic acid (HA). For these adsorption studies, the following concentrations were used: 10 mM AA, 10 mM CA, 1 g/L BSA, and 0.05 g/L HA solutions. The adsorption studies were carried out by flowing solutions over $TiO_2$ NP thin films at a fixed flow rate (~ 0.4 mL/min). The morphology and crystalline phase of $TiO_2$ NPs are

shown in Appendix A Figure A1, indicating that $TiO_2$ NPs have an average size of 23 ± 8 nm and their crystalline in nature containing mostly anatase with a small amount of rutile. The thin film was prepared by drying 1 mL of 1 g/L $TiO_2$ NPs on AMTIR crystal overnight (Figure A2). After the adsorption study, the HA solution (0.05 g/L) was immediately introduced to the same $TiO_2$ NP thin film for the displacement reaction. All spectra were recorded every five minutes to monitor the process. To avoid the interference from the buffer, the range below 1200 $cm^{-1}$ was not included in the analysis as the HEPES buffer showed strong absorptions in this region.

### 3.3.2 Analysis of Two-Dimensional Correlation Spectroscopy

Two-dimensional correlation spectroscopy (2D-COS) is a well-established analytical method used to investigate changes that occur following an external perturbation e.g. time and pH.[45, 60] Furthermore, the sequential order of functional band intensity changes in the displacement process can be analyzed by synchronous and asynchronous maps of 2D-COS, thus revealing the mechanism of displacement processes involving HA on $TiO_2$ NPs first coated with other adsorbates. For the 2D-COS, pretreatments of data (e.g. baseline correction and smoothing) are recommended to avoid artificial peaks in 2D maps. The baseline correction was carried out by a simple offset and the smoothing function uses the Savitzky-Golay algorithm. All spectra used for 2D-COS were baseline corrected and smoothed using the OMNIC 9 software (Thermo Fisher). 2D-COS was performed on a set of dynamic ATR–FTIR spectra at intervals of 5 min collected during the displacement process. The computation of 2D-COS was performed by Matlab R 2017b (MathWorks Inc.) and 2dshige version 1.3 (Shigeaki Mortita, Kwansei-Gaukuin University, 2004-2005) following the algorithm developed by Noda.[61, 62] The results in the synchronous (Φ) and asynchronous (Ψ) 2D correlation spectral maps can be interpreted as follows, which is also known as Noda's rules.[63] In the synchronous map, a positive value of cross peaks indicates the change of

corresponding spectral variations either increase or decrease in the same direction with the applied external perturbation, whereas a negative value means the changes in two opposite directions: one increases and the other decreases. The sequential order between the two bands $\boldsymbol{\upsilon_1}$ and $\boldsymbol{\upsilon_2}$ can be determined by the signs of synchronous and asynchronous correlation maps: if the signs of $\boldsymbol{\Phi}$ and $\boldsymbol{\Psi}$ are the same, the change of $\boldsymbol{\upsilon_1}$band occurs before the $\boldsymbol{\upsilon_2}$ band and if the signs are opposite, the change of $\boldsymbol{\upsilon_1}$ band occurs after the $\boldsymbol{\upsilon_2}$ band. A zero value suggests the two bands have no correlation.

### 3.3.3 Quartz Crystal Microbalance with Dissipation (QCM-D)

The adsorption behavior was also interrogated by a quartz crystal microbalance with dissipation (QSense Pro, Biolin Scientific) using a commercial $TiO_2$ coated 5 MHz AT-cut quartz sensors (Biolin Scientific, QSX 999). The $TiO_2$ sensors were custom made by Biolin Scientific and the provided characterization is shown in Figure A3. X-ray photoelectron spectroscopy confirms a Ti (IV) oxide. The presence of a shoulder at a binding energy around 532eV in Figure A3b indicates that the $TiO_2$ surface on the sensor is hydroxylated.[64] Frequency and energy dissipation changes were monitored as a function of time. The $TiO_2$ sensors were reused several times for different measurements. Between each measurement, the crystal sensors were cleaned by soaking in 2% sodium dodecyl sulfate solution (SDS, Sigma Aldrich), dried with $N_2$, and then treated in a UV-ozone chamber for 20 min. The baseline was collected with Milli-Q water. A gentle flow of each solution was maintained over the $TiO_2$ surface at a flow rate of 50 µL/min for 60 min. Following this, the flow was stopped, and the solution was kept over the surface for 30 min for equilibration. Reviakine *et al*. proposed a very strict criteria that the ratio of the change in dissipation to the change in frequency should be less than $4\times 10^{-7}$ Hz for a laterally homogeneous film in order to apply the Sauerbrey equation shown in Eq. 3.1.[65] The mass gain can still be

calculated based on the Sauerbrey equation for the surface when there are small changes in dissipation less than 2 ppm,[66]

$$\Delta \boldsymbol{m} = \frac{\boldsymbol{C} \times \Delta \boldsymbol{F}}{\boldsymbol{n}} \qquad (3.1)$$ [67]

where $\Delta \boldsymbol{m}$ is the mass gained per unit area (ng·cm$^{-2}$), $\Delta \boldsymbol{F}$ is frequency shift (Hz$^{-1}$), $C$ is a constant value of 17.7 ng·cm$^{-2}$ ·Hz$^{-1}$ for a 5 MHz AT-cut QCM sensor, and $\boldsymbol{n}$ the overtone number. Overtones 5, 7, 9 and 11 were monitored for all measurements. The QCM-D plots shown herein have all been normalized by the overtone number.

### 3.3.4 Sedimentation and Dynamic Light Scattering

The solutions for sedimentation and dynamic light scattering (DLS) studies were prepared by dispersing $TiO_2$ NP powder in 10 mM AA, 10 mM CA, and 1 g/L BSA solutions, respectively. The pH and ionic strength were kept at 7.5 and 0.03 M (87.6 mg NaCl in 50 mL). $TiO_2$ NP suspensions were sonicated for 10 min for mixing prior to placing on a Cole–Parmer rotator overnight. The concentrations of $TiO_2$ NP suspensions for sedimentation and DLS are 0.5 g/L and 0.1 g/L, respectively. An aliquot was used for the sedimentation and DLS analysis of pre-coated $TiO_2$ NPs. Then, for the displaced coating samples, 15 mL aliquots were transferred to 15 mL centrifuge tubes and then centrifuged at 10000 rpm for 20 min. After carefully removing the supernatant, 15 mL of 0.05g/L HA solution at same pH and ionic strength was added to the centrifuge tubes. The suspensions were sonicated for 10 min and mixed overnight. The samples were then used for the sedimentation and DLS analysis. The sedimentation experiments were performed using a UV–Vis spectrometer (Lambda 35, PerkinElmer), by monitoring the light intensity at a wavelength of 550 nm over time. The DLS measurement was conducted with a Delsa Nano C instrument (Beckman Coulter Inc.).

## 3.4 Results and Discussion

### 3.4.1 Adsorption of AA, CA, HA and BSA on $TiO_2$ NP Surfaces

Table 3.1 shows both molecular and representative structures of the relevant species under study, ascorbic acid (AA), citric acid (CA), humic acid (HA) and bovine serum albumin (BSA), along with information about the pH dependent behavior, including $pK_a$ values and the pH–dependent conformations in the case of BSA. The functional groups within each molecule are relevant for the adsorption on $TiO_2$ NPs, since the adsorption process often involves exchange reactions between molecules and the surface hydroxyl groups and or hydrogen bonding interactions. [42, 61, 62, 68] The ATR–FTIR spectra shown in Figure 3.1 provide the details of the adsorption of AA, CA, HA and BSA onto $TiO_2$ surfaces by monitoring the vibrational frequencies

**Table 3.1** Representation of different molecules used in this study and their different pH dependent properties (protonation and secondary conformation).

| AA | CA | HA | BSA |
|---|---|---|---|
| 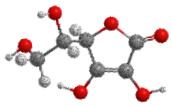 | 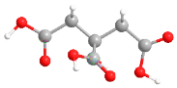 | 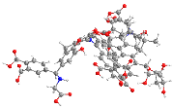 | 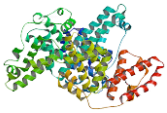 |
| $pK_a$=4.2<br>$H_2Asc \rightleftarrows HAsc^-$<br>$pK_a$=11.8<br>$HAsc^- \rightleftarrows Asc^{2-}$ | $pK_a$=3.1<br>$H_3Cit \rightleftarrows H_2Cit^-$<br>$pK_a$= 4.76<br>$H_2Cit^- \rightleftarrows HCit^{2-}$<br>$pK_a$=5.8 | $pK_a$<br>pH<br>12<br>9<br>7<br>5<br>2<br>Phenolic groups<br>Carboxylic groups | pH<br>9<br>4.5<br>4<br>3.5<br>Normal (N) Form<br>Fast (F) form<br>Extended (E) form |

and intensity of the functional groups. In addition, the solution phase spectra of these are also shown.

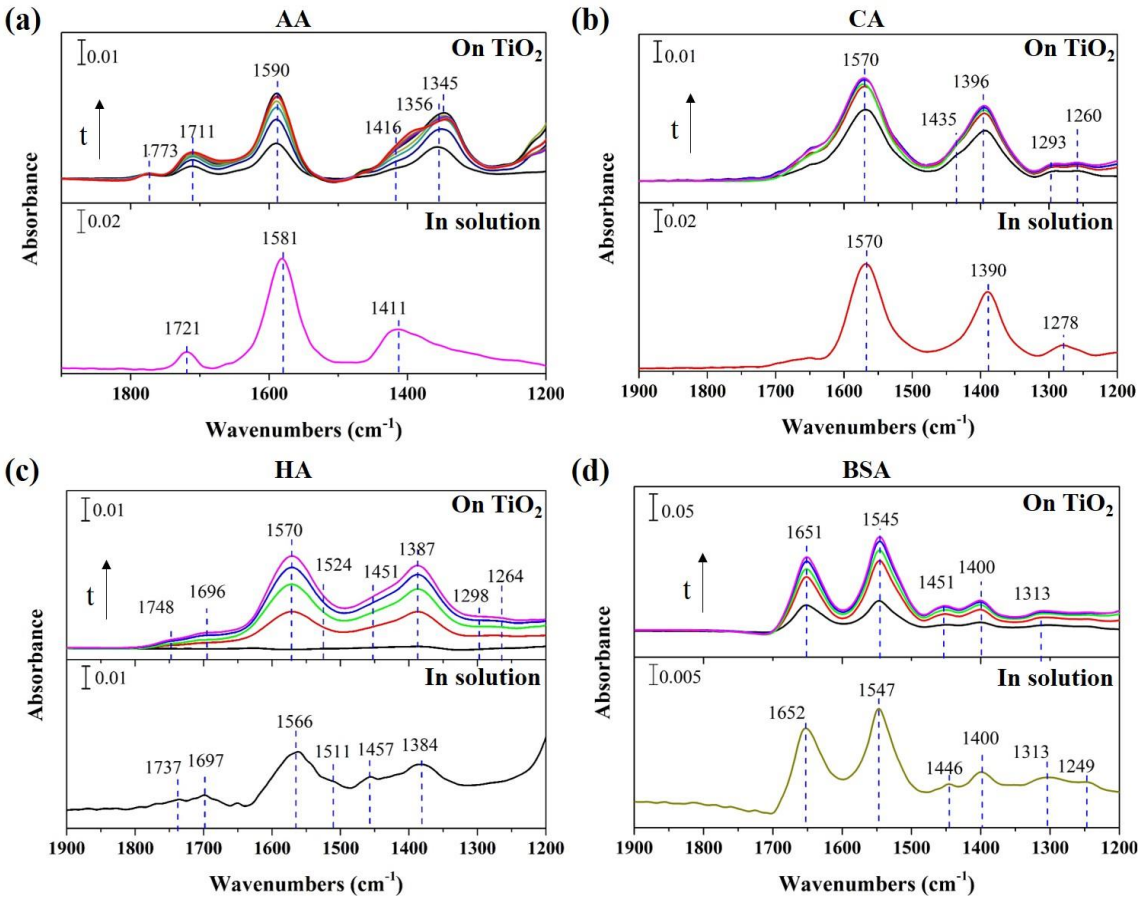


**Figure 3.1** ATR–FTIR spectra of target species adsorbed onto $TiO_2$ and in solution phases. (a) Spectra of adsorbed 10 mM and in solution 100 mM AA; (b) spectra of adsorbed 10 mM and in solution 100 mM CA; (c) spectra of adsorbed 0.05 g/L and in solution 1 g/L HA; (d) spectra of adsorbed 1 g/L on and in solution 10 g/L BSA. The adsorption spectra shown were collected at 5 min (black), 30 min (red), 60 min (green), 90 (blue), 120 min (magenta).

AA is the smallest molecular species amongst the four and its structure is composed of a primary OH, a secondary OH, and an enediol in a lactone. At pH 7.5, one of the enols in AA is deprotonated, and the deprotonation improves the conjugation enediol group and C=O. As seen in Figure 3.1a, the conjugation of the enediolate with the C=O bond causes a shift of the C=C stretching frequency to 1581 $cm^{-1}$ in solution. However, when AA binds to the $TiO_2$ surface, there

is a blue shift to 1590 $cm^{-1}$. The binding mode of AA on $TiO_2$ surface has been reported previously.[69] AA binds to Ti (IV) sites through the enediols. One enolate binds to Ti (IV) directly,

**Table 3.2** Assignments for the vibrational frequencies ($cm^{-1}$) of the main functional groups in the studied molecules.

| molecule | vibrational mode | this work ($cm^{-1}$) | | literature ($cm^{-1}$) [44, 52, 69, 78-86] |
|---|---|---|---|---|
| | | solution | adsorbed | |
| AA | υ (C=O) | 1721 | 1773, 1711 | 1780, 1725, 1702 |
| | υ (C=C) | 1581 | 1590 | 1604, 1595,1594 |
| | υ (enediolate, C-OH) | 1411 | 1416 | 1415, 1345 |
| | δ (C-OH) / δ (C-H) | | 1356 | 1396,1359,1369 |
| | υ (enediolate, C-OH) * | | 1345 | 1345 |
| CA | $υ_{asym}$ ($COO^-$) | 1570 | 1570 | 1580−1569 |
| | $υ_{sym}$ (COO-)/OH def | 1390 | 1396, 1435 | 1436, 1400−1391 |
| | δ(O=C-O-) | 1278 | 1293, 1260 | 1292-1260 |
| HA | υ (C=O) | 1737, 1697 | 1748,1696 | 1720, 1640 |
| | $υ_{asym}$ ($COO^-$) | 1566 | 1570 | 1590−1550 |
| | υ (C=C) | 1511 | 1524 | 1525 |
| | δ (C-H) | 1457 | 1451 | 1450 |
| | $υ_{sym}$ (COO-)/OH def | 1384 | 1387 | 1350 |
| | υ (phenol C-OH) | | 1264 | 1270 |
| BSA | amide I $υ_s$ (c=O) major + $υ_s$ (C-N) minor | 1652 | 1651 | 1695−1630 |
| | amide II $υ_s$ (C-N) +δ (N-H) out of phase | 1547 | 1545 | 1550 |
| | δ (C-H) | 1446 | 1451 | 1500-1400 |
| | amide III or υ (C-O)/ υ (C-O-C)/ υ (C-C) | 1400, 1313, 1249 | 1400,1313 | 1400−1000 |

* the vibration frequency of enediolate forming a 5-membered ring.

and the other enol group assists in chelating to a Ti (IV) ion which then forms a five membered ring structure with Ti (IV) ion. This is supported by the shift in the vibration of C-O from 1356 to 1345 $cm^{-1}$ during the adsorption. A charge transfer occurs between adsorbed AA and Ti (IV) ion.[69] In this structure, the lactone ring in AA is positively charged,[70, 71] possibly resulting in a blue shift of carbonyl vibration mode into from 1721 $cm^{-1}$ and 1773 $cm^{-1}$. Besides, AA can also bind to Ti (IV) through only one enediolate, thus carbonyl vibration shifts from 1721 to 1711 $cm^{-1}$.

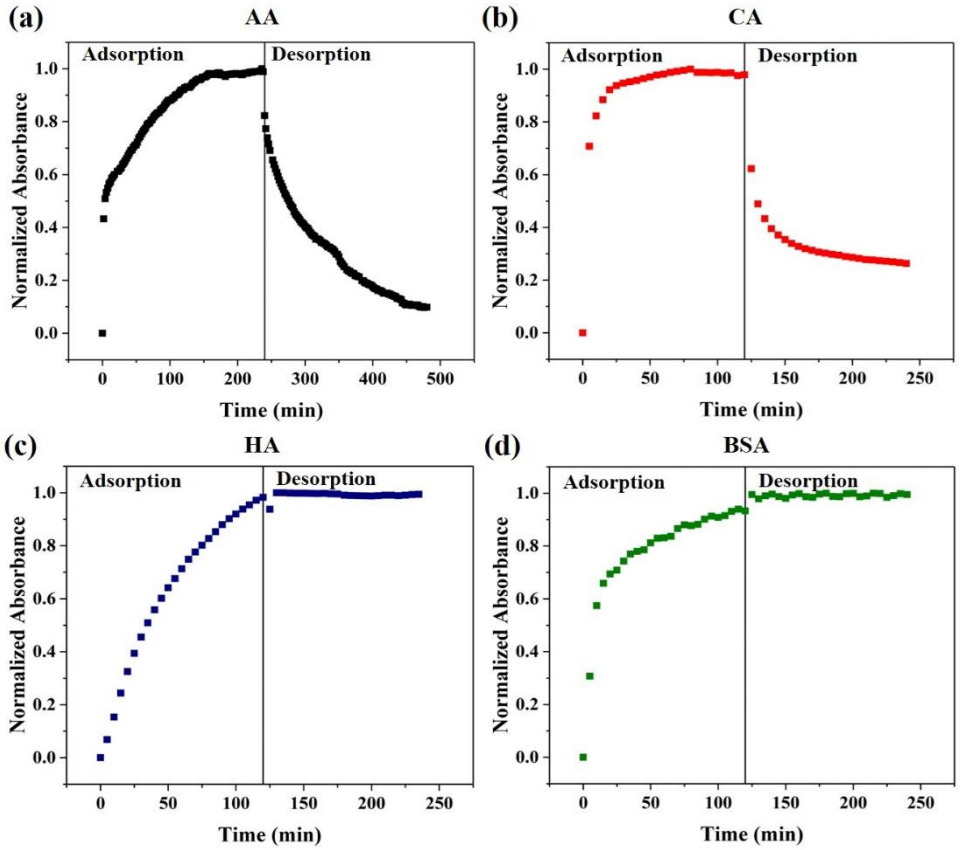


**Figure 3.2** The adsorption and desorption processes of (a) 10 mM AA, (b) 10 mM CA, (c) 0.05 g/L HA and (d) 1 g/L BSA. The intensity was normalized using the absorbance at 1385 $cm^{-1}$ for AA, 1570 $cm^{-1}$ for CA, 1570 $cm^{-1}$ for HA, and 1545 $cm^{-1}$ for BSA, respectively.

For CA, the structure consists of a tertiary alcohol OH and three carboxylic groups that are all deprotonated at pH 7.5.[52] The spectra for the free solution phase and adsorbed molecules are shown in Figure 3.1b. The asymmetric stretching vibration of the carboxylate groups is around

1570 $cm^{-1}$ in both adsorption and solution spectra, but the symmetric vibration shifts from 1390 $cm^{-1}$ in solution to 1396 $cm^{-1}$ when adsorbed on the $TiO_2$ NP surface and a shoulder appears at 1435 $cm^{-1}$. The splitting of carboxylate vibration between asymmetric and symmetric vibrations indicates that some carboxylates interact with surface through a bidentate bridging mode. It is worth noting that the band of the deformation O=C–O at 1278 $cm^{-1}$ in solution phase shifts to higher wavenumbers at ~1293 $cm^{-1}$ for adsorbed species on $TiO_2$ NPs. This is caused by a specific interaction between $COO^-$ and Ti (IV), suggestive of monodentate bonding. Park *et al.* propose that citrate binds on surface through bidentate bridging via the central carboxylate ion and monodentate via one of terminal carboxylates.[72]

HA has multiple functional groups that can participate in the interaction with $TiO_2$, including carbonyl, amide, carboxylate, phenol, polysaccharide, and alcohol hydroxyl.[44, 45] In the spectra for adsorbed HA on $TiO_2$ NPs (Figure 3.1c), the dominant absorption bands appear at 1570 and 1387 $cm^{-1}$, which correspond to the asymmetric and symmetric carboxylate vibrations, respectively. Importantly, these characteristic frequencies shift from 1566 $cm^{-1}$ and 1384 $cm^{-1}$ in solution phase to 1570 $cm^{-1}$ and 1386 $cm^{-1}$ for adsorbed species, respectively. This indicates that HA binds to $TiO_2$ NP surface via carboxylate as suggested by others.[44] Other characteristic absorption bands including 1748 $cm^{-1}$ for the C=O stretching of protonated carboxylic acid group, 1451 $cm^{-1}$ for the C–H bending mode, and 1298 $cm^{-1}$ for –COO–Ti groups are seen. In addition, an absorption at 1264 $cm^{-1}$ possibly comes from the binding mode phenolic C–O–Ti, which is not present in solution phase.[73]

For BSA, the spectra (Figure 3.1d) show an amide I band at near 1650 $cm^{-1}$, which mainly consists of stretching vibration C=O of amide.[74] The other intense band in the spectra is due to the amide II band around 1550 $cm^{-1}$ caused by the bending of N–H and C–N. In previous studies, we have observed information about the small changes in the secondary structures which include α–

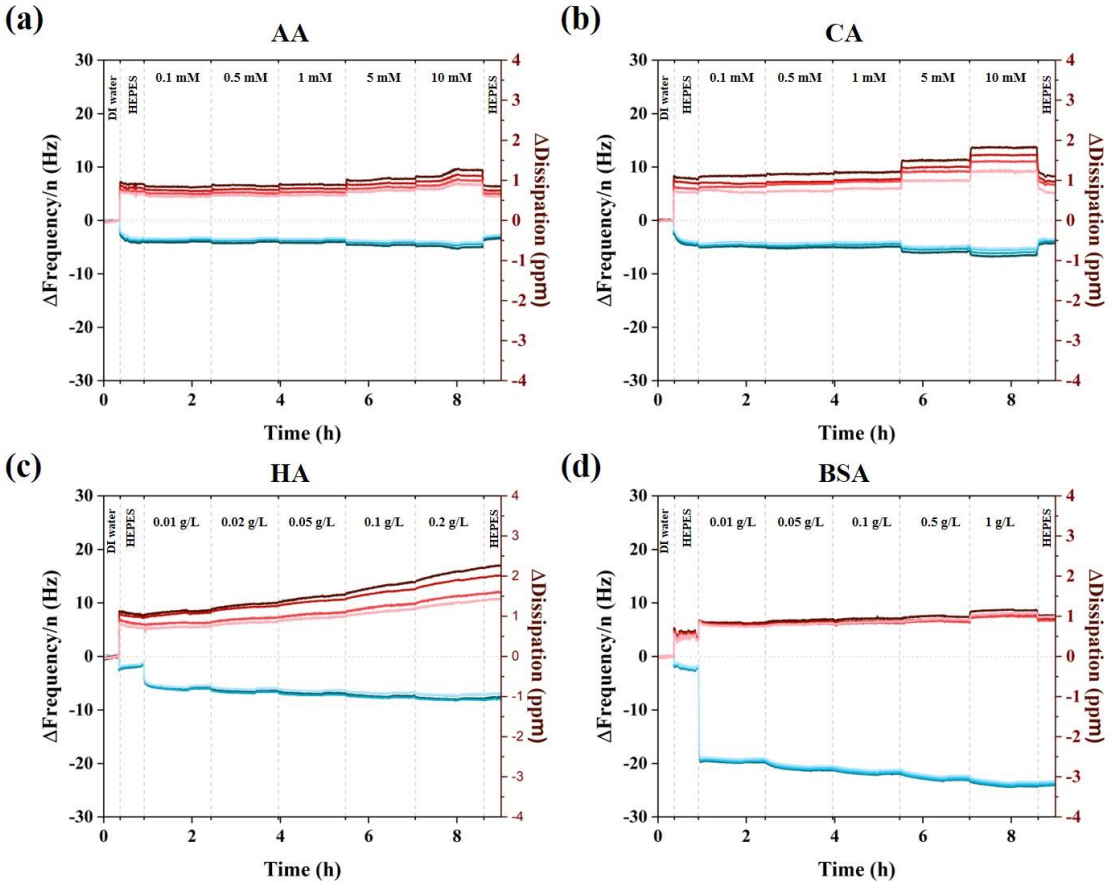


**Figure 3.3** Shifts in frequency and dissipation, normalized by overtone number, for the adsorption of ascorbic acid (a), citric acid (b), humic acid (c) and bovine serum albumin (d) onto a $TiO_2$ coated surface with QCM–D. Blue and red lines represents changes in frequency and dissipation, respectively. Data are shown for overtones 5, 7, 9, and 11 in a color gradient, in which the darker colors are for smaller overtones.

helixes, extended chains and turns during the adsorption of BSA onto $TiO_2$ NPs.[60, 75-77] A summary of these peak assignments are listed in Table 3.2, including comparison to the values reported in the literatures.[44, 52, 69, 78-86]

The adsorption-desorption process was also investigated by ATR–FTIR, shown in Figure 3.2. The desorption behavior of the adsorbed molecules when washing with a buffer solution reveals the nature of the interaction with the surface. This is observed when the maximum intensity reached during the adsorption process for AA and CA decreases upon the desorption process. In addition, Figure 3.2 shows that AA has a slower adsorption and desorption kinetics compared to CA. This discrepancy relates to the binding modes to $TiO_2$ surface. AA tends to form a 5-membered ring with Ti (IV) while CA binds via a simpler bidentate bridging mode. For BSA and HA, the intensity of adsorption spectra approaches the maximum values and its intensity does not change when buffer is introduced suggesting irreversible adsorption and little loss of BSA or HA from the surface. In contrast to AA and CA, macromolecules such as BSA and HA, prefer to adsorb on surface by forming monolayer e.g. BSA[83] and HA.[87]

**Table 3.3** Summary of the surface coverage assuming a rigid layer.

| AA | | CA | | BSA | | HA | |
|---|---|---|---|---|---|---|---|
| **Initial concentration, mM** | **Adsorbed molecules (St. Dev.), x10$^{13}$ molecules/cm$^2$** | **Initial concentration, mM** | **Adsorbed molecules (St. Dev.), x10$^{13}$ molecules/cm$^2$** | **Initial concentration, g/L** | **Adsorbed molecules (St. Dev.), x10$^{13}$ molecules/cm$^2$** | **Initial concentration, g/L** | **Adsorbed molecules (St. Dev.), x10$^{13}$ molecules/cm$^2$** |
| 0.10* | 21.3 (2.06) | 0.10* | 25.4 (1.99) | 0.01* | 0.32 (0.01) | 0.01* | 1.57 (0.06) |
| 0.50 | 21.5 (1.96) | 0.50 | 25.1 (2.27) | 0.05 | 0.34 (0.01) | 0.02 | 1.71 (0.08) |
| 1.00 | 21.8 (2.03) | 1.00 | 24.3 (2.41) | 0.10 | 0.35 (0.01) | 0.05 | 1.81 (0.09) |
| 5.00 | 24.8 (2.26) | 5.00 | 28.9 (2.58) | 0.50 | 0.37 (0.01) | 0.10 | 1.95 (0.10) |
| 10.0 | 27.0 (2.59) | 10.0 | 33.0 (3.78) | 1.00 | 0.39 (0.01) | 0.20 | 2.07 (0.11) |

* At this concentration, the adsorbed mass includes a contribution from HEPES

Following these ATR–FTIR experiments, QCM-D was used to investigate adsorption and desorption processes of these four species by measuring the adsorbed mass and assessing

conformation changes of the molecules by monitoring changes in frequency (ΔF) and dissipation (ΔD), respectively. Although the QCM experiment uses a deposited $TiO_2$ surface but not NPs, it is expected that these measurements can provide additional insights into the interactions of these molecules with $TiO_2$ surfaces and thus complementing the ATR–FTIR measurements. It is important to note that the QCM will not consider the curvature effect on the adsorption onto NPs but can verify in a quantitative manner the qualitative observations from the ATR–FTIR. In particular, it will show if the surface is fully covered with the adsorbate at the concentration used in the ATR–FTIR experiments. The sensors are first exposed to the buffer solution, and a small amount of HEPES is adsorbed. Then, the corresponding adsorbate is introduced. Solutions with 5 increasing concentrations were introduced to calculate the surface coverage (Table 3.3, molecules/$cm^2$). However, due to the similarity in the molar mass, the displacement between HEPES and AA or CA on surface do not exhibit a discernible frequency shift at low concentrations. Thus, AA (Figure 3.3a) and CA (Figure 3.3b) gained mass, can be only associated to the adsorbate when concentrations are higher than 5 mM. As shown in Table 3.3, for the small molecules AA and CA with relatively weak interaction with the surface, the number of adsorbed molecules is not greatly affected at low solution concentrations (smaller than 5 mM), indicating at such concentrations the small molecules form a stable interface like a monolayer. In contrast, a noticeable gain is observed at higher concentrations (larger than 5 mM), which is associated with an increase in dissipation. AA and CA have relatively weak interaction with the surface so that they are reversibly or partially reversibly adsorbed on the surface. However, this increase in mass and dissipation is diminished when the surface is washed with buffer solution. The removal of the loosely bonded molecules when flowing the buffer solution, is in good agreement with adsorption-desorption study by ATR–FTIR (Figure 3.2). In contrast, larger macromolecular species such as

HA (Figure 3.3c) and a protein such as BSA (Figure 3.3d) show a significant decrease in ΔF at low concentrations that is far larger than that observed for the HEPES buffer solution. The surface coverage (molecules/cm$^2$) observed for the different concentrations of the analyzed solutions are summarized in Table 3.3.

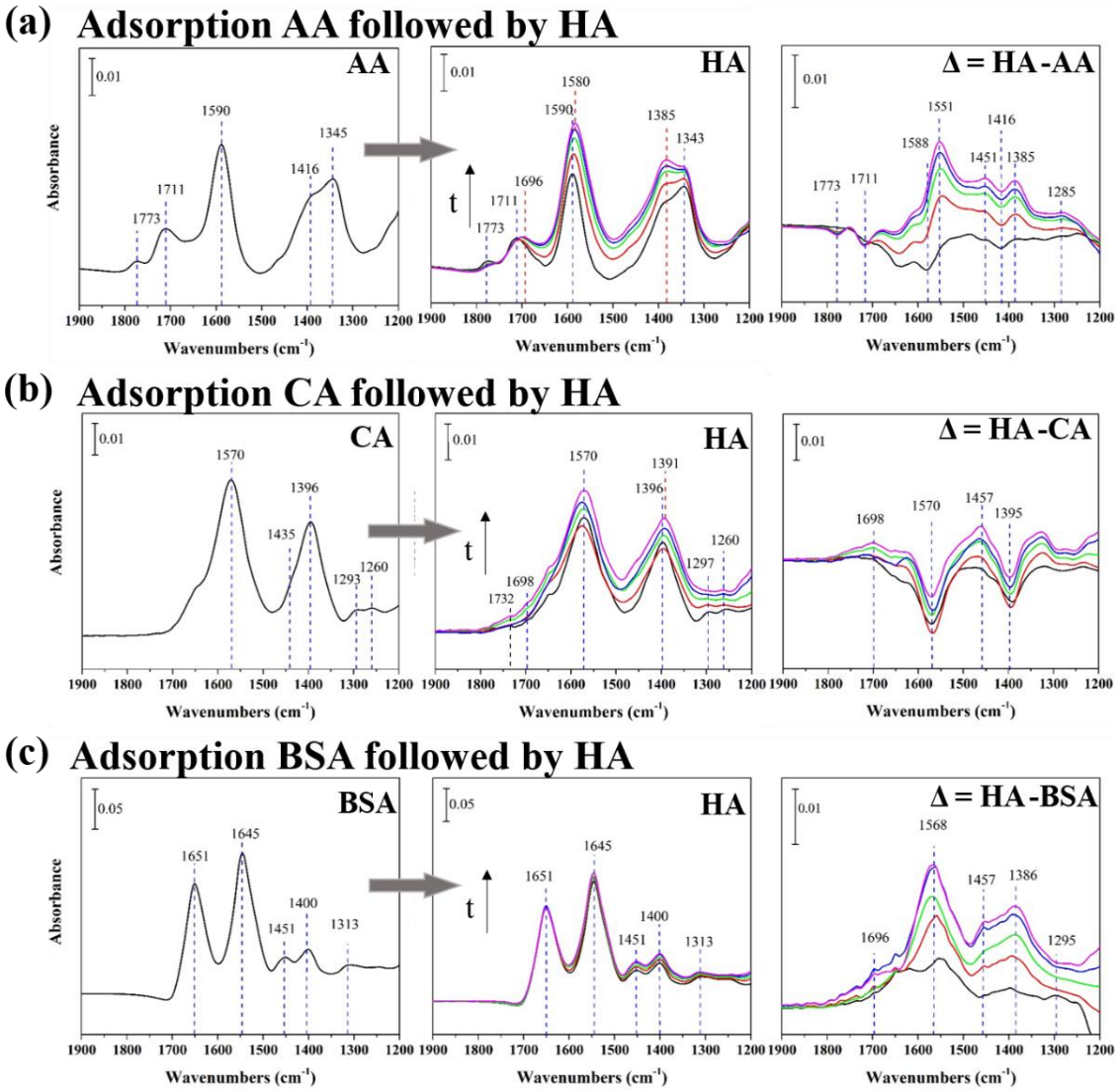


**Figure 3.4** ATR-FTIR of the displacement reactions of AA-(a), CA-(b), and BSA-(c) pre-coated $TiO_2$ NPs by HA. The initial coating spectra are on the left, the time dependent displacement spectra are in the middle, and the difference spectra are on the right. The displacement spectra were collected at 5 min (black), 30 min (red), 60 min (green), 90 (blue), 120 min (magenta). The difference spectra were obtained by subtracting the initial spectra from displacement spectra.

For AA, CA, and BSA, the adsorption process at each condition would reach the equilibrium very quickly revealing that ΔD and ΔF quickly level off and become constant values. However, HA never exhibits a plateau phase in the ΔD plot which is different from other molecules, suggesting that HA alters its conformation in order to adsorb onto the $TiO_2$ surface. In addition, the shifts in dissipation provide insights into the viscoelasticity of the adhered layers.[65, 88, 89] The change in dissipation (ΔD) relates to how much the added layer deforms (soft surface) and how much the added layer resists deformation (rigid surface) when the crystal shears.[90] A rigid surface, such as monolayer of adsorbed molecules, typically has a value of ΔD less than 1 ppm ($10^{-6}$), while values larger than 1 ppm imply a soft surface.[91] The discrepancy on the dissipation plots of the different overtones supports the formation of a softer film,[65, 89] which in the case of HA, suggests the changes on conformation is caused by intermolecular interactions and by the different adsorption modes generated for the multiple functional groups in the macromolecule, which is in a good agreement with the ATR–FTIR results.

### 3.4.2 Displacement Reactions

In these experiments, the displacement process was recorded by introducing 0.05 g/L HA solution on the $TiO_2$ NP film that was pre-coated with AA, CA, and BSA in the adsorption process, respectively. As seen in Figure 3.4a, the profile of the AA-coated $TiO_2$ NP spectra significantly changes during the displacement process. The main adsorption band shifts from 1590 to 1580 $cm^{-1}$ when introducing HA to the $TiO_2$ film, and the other main adsorption band at 1385 $cm^{-1}$ increases during the displacement process (Figure 3.4a middle). In addition, the band shifts from 1711 cm to 1696 $cm^{-1}$ which is assigned to carbonyl vibration from HA. To confirm the presence of HA on the surface, the initial spectrum was subtracted from the displacement spectra, shown in Figure 3.4a right. The progressive decrease in time for the bands at 1773 and 1711 $cm^{-1}$ from carbonyl

vibrations due to adsorbed AA, indicates HA displaces AA. Also, two new peaks appear at 1551 and 1385 $cm^{-1}$, which correspond to the $–COO^{–}$ vibrations of HA. In addition, the asymmetric vibration of $–COO^{–}$ of HA appears to be shifted to 1551 $cm^{-1}$ instead of 1570 $cm^{-1}$ due to a negative contribution of the peak at 1590 $cm^{-1}$ caused by the displacement. The absorption at 1285 $cm^{-1}$ comes mainly from the deformation of –COO–Ti moiety when binding on the surface. All these changes indicate that HA displaces AA from the surface. Due to the reversible nature of the AA adsorption onto the $TiO_2$ surface, we hypothesize that HA displaces most of the AA as shown in the scheme in Figure 3.5a. However, it is not possible to rule out that some AA molecules are still attached on the surface.

During the displacement of CA, the similarity between carboxylate vibrations are the characteristic IR bands of CA (Figure 3.4b left), and these IR features are very similar to the vibrations observed for HA on $TiO_2$ surface (Figure 3.1d), which makes it difficult to discern the displacement process. However, during the displacement reaction (Figure 3.4b middle), it is seen that the symmetric stretching of COO– band at around 1396 $cm^{-1}$ has around a 5 $cm^{-1}$ red shift, changing from 1396 to 1391 $cm^{-1}$. In addition, the growing band above 1700 $cm^{-1}$ is from the C=O

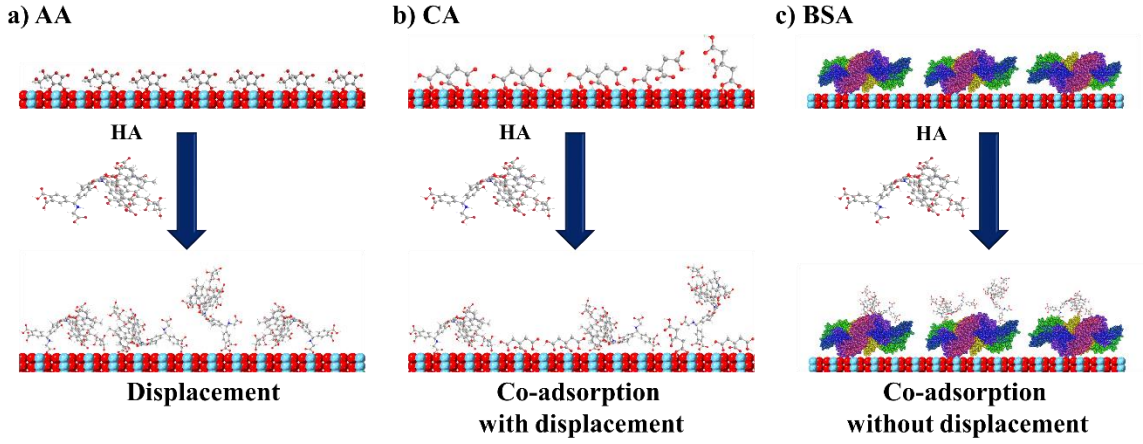


**Figure 3.5** A schematic representation of displacement reactions and co-adsorption by HA on pre-coated $TiO_2$ surfaces with AA (a), CA (b), and BSA (c), respectively. HA is represented here as a macromolecular structure.

of carboxylic acid group in HA. Furthermore, the difference spectra (Figure 3.4b right) corroborates the displacement on $TiO_2$ NPs as it displays the main features of adsorbed HA onto $TiO_2$ NPs, such as carbonyl vibration from HA at 1698 $cm^{-1}$. Additionally, the main bands of CA at 1570 and 1395 $cm^{-1}$ display growing negative values with time in the difference spectra, suggesting the loss of CA from the surface followed by a time dependent HA adsorption. Therefore, we infer that CA is partially displaced by HA as shown in Figure 3.5b. As suggested in the displacement process, when $TiO_2$ NPs fully coated with small molecules e.g. AA and CA are exposed to HA solution, HA tends to displace the pre-coatings. In the case of CA, it is possible that a partial displacement occurs as shown in Figure 3.5b, where HA displaces more weakly bonded CA molecules while co-adsorbing with CA which may be on edge and/or corner sites leading to more strongly bonded CA molecules on the surface of $TiO_2$ NPs.

In the case of BSA, the displacement process in Figure 3.4c (middle panel) shows no significant alteration of vibrational frequency, but an increase of intensity after introducing HA. The difference spectra (Figure 3.4c right) confirm that HA is adsorbing on the surface. A possible explanation is that HA mainly co–adsorbs with BSA rather than displaces it. At neutral pH, due to negative charges on both BSA and HA, electrostatic repulsion is expected, it is therefore concluded that non-specific hydrophobic interactions are the driving force for the co-adsorption of HA and BSA.[92-94] As Zhao *et al.* report,[92] HA can overlap on the top of BSA ring-like aggregates. Figure 3.5c shows both adsorption modes whereby HA stacks on top of the adsorbed BSA. In addition to ATR–FTIR study, the process of displacement of BSA by HA was also studied by QCM-D (Figure A4). Compared to BSA, HA has much lower molecular mass, therefore, if BSA was completely displaced by HA, the mass should decrease. However, the QCM-D result shows that the mass increases when introducing HA and the dissipation quickly reaches a value above two. This all

supports that HA is not able to displace BSA but instead co-adsorb on the surface forming a second layer interacting with mainly adsorbed BSA molecules.

To corroborate the proposed displacement modes in Figure 3.5, the reverse processes were also investigated. In these experiments, NP surfaces were coated first with HA, then AA, CA or BSA was introduced and finally the buffer was flowed over the film after the displacement process. The spectra for each step are shown in Figure A5. The results agree with the expectation that AA weakly binds to the surface and no big change was observed after flowing buffer, therefore AA does not change or displace the HA-coating on the surface. CA is partially able to displace HA as reflected in the shift of the carboxylate symmetric vibration from 1385 to 1395 $cm^{-1}$ corroborating that CA and HA are co-adsorbed. Most interesting is that BSA fully displaces HA from surface due to its strong binding ability. The summary of these processes is represented in Figure A6.

Due to the overlap of some IR bands in the one-dimensional spectra, 2D-COS was employed to investigate the details of the displacement of these initial molecular and protein coatings by HA. In addition, the synchronous (Φ) and asynchronous (Ψ) 2D correlation spectral maps are helpful in discerning the role of the functional groups in these displacement reactions. The synchronous (left) and asynchronous (right) 2D correlation maps shown in Figure 3.6 are for the displacement by HA of NP surface pre-coated by AA (a), CA (b), and BSA (c), respectively.

When HA is introduced to the AA-coated $TiO_2$ NP film, three predominant autopeaks show up on the diagonal in synchronous 2D correlation spectra map (Figure 3.6a left) at near 1560, 1451 and 1386 $cm^{-1}$, which agree with the main bands in the HA spectra (Figure 3.1c), the positive values of the peaks indicate that the band intensity changes in the same direction. There is also a weak autopeak showing at 1277 $cm^{-1}$, which is assigned to δ(O=C-O-) when binding to $TiO_2$

surface.[52] Interestingly, there are a few barely noticeable small negative cross peaks appearing at (1560, 1775), (1560,1721), (1451, 1775), (1451, 1721), (1386, 1775), (1386, 1721). The negative

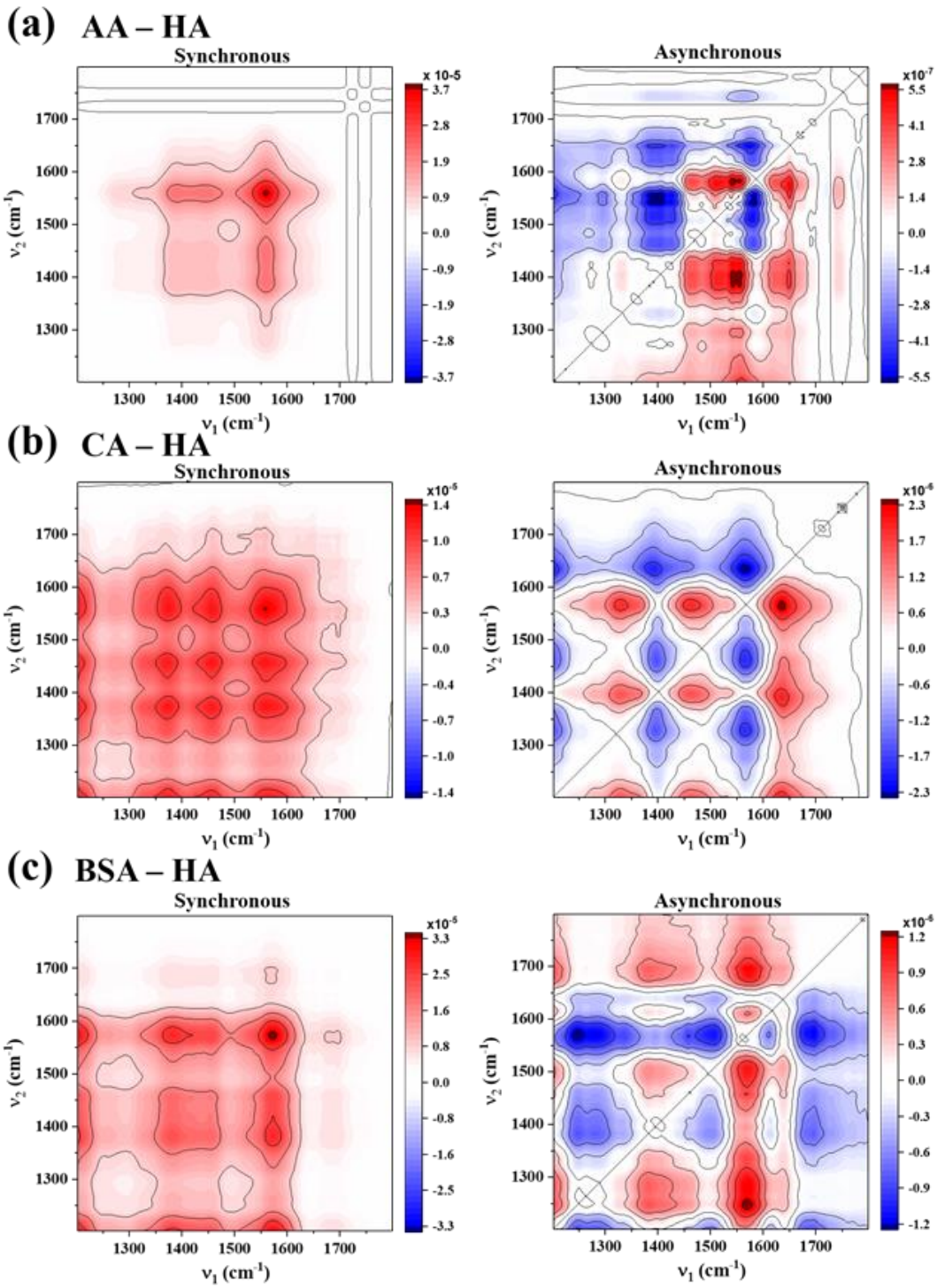


**Figure 3.6** Synchronous (left) and asynchronous (right) 2D correlation maps following introduction of HA to a $TiO_2$ surface covered with (a) AA, (b) CA, and (c) BSA.

peaks indicate that these band intensity changes are in opposite direction. During the displacement process, AA is displaced by HA, and HA adsorbs on surface, which results in a decrease of carbonyl from AA (1775 and 1721 $cm^{-1}$) and increase of carboxylate absorptions from HA (1560 and 1451 $cm^{-1}$). These data agree with the full surface displacement reaction proposed in Figure 3.5a. The asynchronous map (Figure 3.6a right) provides useful information of the sequential order of functional group changes in the adsorption. A series of cross peaks correlated to 1650 $cm^{-1}$ assigned to C=O (ketone, amide) is observed, which merged into the peak of 1590 $cm^{-1}$ in the 1D IR spectra. The relevant cross peaks in asynchronous map are positive, such as (1650, 1560), (1650, 1389), (1650, 1291), (1743, 1560), (1743, 1389), (1560, 1291) (1560, 1269). According to Noda's rules,[95] the main bands changes shown in the asynchronous map follow such order: 1743, 1650 $cm^{-1}$ bands are prior to 1560 and 1389 $cm^{-1}$. This is followed by 1291 and 1269 $cm^{-1.}$ It indicates changes are in the sequence C=O (carboxylic) and C=O (ketone, amide) are earlier than $COO^{-}$, which is followed by COO–Ti (monodentate) and C–O–Ti (phenolic).

In the case of the CA-coated $TiO_2$ NP surface, when introducing HA, the synchronous map (left panel in Figure 3.6b) displays similar autopeaks to AA-coated surface at 1560, 1457 and 1372 $cm^{-1}$. In addition, two weak autopeaks were observed at 1696 and 1274 $cm^{-1}$, which are carbonyl vibration and deformation of carboxylate from HA, respectively. The lack of negative peaks suggest that co-adsorption is the main process during the time-dependent reaction as proposed in Figure 3.5b. The relevant cross peaks in asynchronous map are positive, such as (1638, 1560), (1638, 1390), (1638, 1460), (1696, 1560), (1696, 1460), (1330, 1560), (1330, 1390), (1460, 1560) (1330, 1264). This asynchronous map (Figure 3.6b right) exhibits a slightly different order: 1696, 1638 → 1460, 1330 →1560, 1390, 1264 $cm^{-1}$. The structural changes implied in asynchronous map

follow such a sequence: C=O (carboxylic) and C=O (amide, ketone) are earlier than $COO^-$and C–O–Ti (phenol).

In comparison to the small molecules coated NPs, BSA-coated NPs has two main autopeaks (Figure 3.6c left) on the diagonal at 1572 and 1385 $cm^{-1}$ representing the adsorption of HA. The lack of negative peaks supports the proposed co-adsorption scheme in Figure 3.5c. The relevant cross peaks in asynchronous map are positive, such as (1610, 1505), (1610,1250), (1570,1696), ((1570, 1505), (1570, 1284), (1505,1250). Based on the interpretation of the asynchronous 2D correlation map (Figure 3.6c right), the changes observed on the peaks during sorption follow the order 1570→ 1696, 1610 → 1505→ 1284, 1250 $cm^{-1}$. According to the sequence, the structural changes occur in this sequence: $COO^-$ → C=O (amide, ketone) → C=C→ $COO^-$ (bending), C–OH (phenol). Therefore, HA approaches BSA-coated $TiO_2$ surface through intermolecular interaction of H–bonding between these dangling functional groups ($COO^-$ and C=O). As already noted, in the displacement reaction HA co-adsorbs on the surface mainly through interacting with BSA instead of displacing BSA. It has been reported that HA tends to interact with BSA ring-like aggregates by hydrophobic interaction,[92] thus resulting in the change of C=C vibration. The changes in the bending of carboxylate (1284 $cm^{-1}$) and the phenol vibration (1250 $cm^{-1}$) that show up after the changes in the C=C vibration also suggest that HA keeps changing conformation when adsorbing onto the BSA-coated $TiO_2$, this agrees with the changes on dissipation observed with QCM-D (Figure A4).

Chen *et al.* demonstrate that functional groups changes of HA while adsorbing onto bare $TiO_2$ follow the trend: carboxylate → C–O (phenol or tertiary) → C=O (ketone, amide) at pH 7.[45] In our study, the surface is pre-coated by other adsorbates and it is observed that HA shows a different adsorption pathway for each case compared to adsorption onto the hydroxylated surface.

Therefore, we demonstrated that surface coatings on NP surfaces can modify the behavior of exactly how NPs interact with NOM in the environment.

3.4.3 Sedimentation and Agglomeration.

In order to evaluate the effect of these coatings and displacement reactions on NP agglomeration with HA, the agglomeration was assessed by following the changes in the hydrodynamic size of the agglomerates and their sedimentation behavior. Figure 3.7 shows sedimentation curves of the $TiO_2$ NP suspensions before and after ligand displacement. Any impact would be of great significance for the transport and fate of NPs in the environment.[96, 97] Adsorbates on $TiO_2$ NPs such as AA and CA result in steric repulsion, thus inhibiting the agglomeration of $TiO_2$ suspensions.[52, 69, 72] Therefore, the stability of $TiO_2$ NPs coated by AA or CA shows an increase compared to bare hydroxylated $TiO_2$ NPs in HEPES buffer (Figure 3.7a,b). In comparison to AA and CA, HA carries more polar functional groups such as phenol and carboxylate and has stronger steric hindrance.[44, 98] As expected, the sedimentation rates of the samples after displaced by HA became much slower than those capped with only small molecules. Besides, the hydrodynamic diameters of the agglomerates are reduced in the presence of HA with

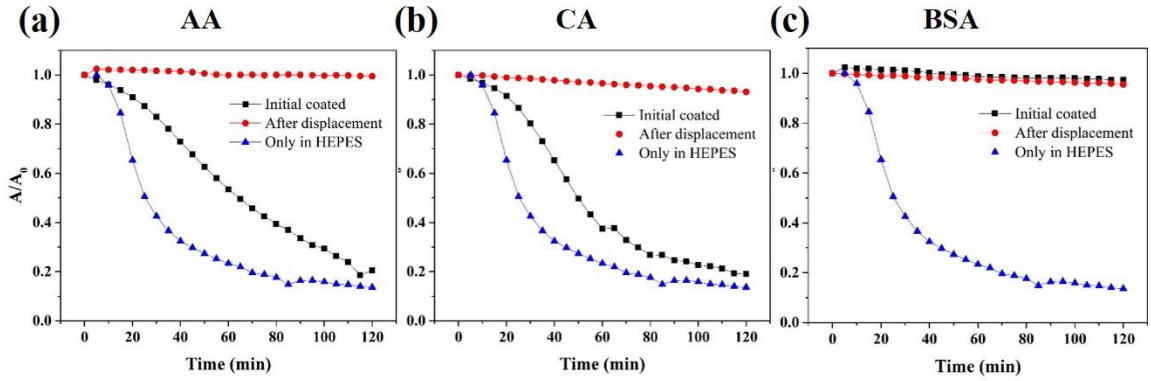


**Figure 3.7** The effects of displacement reactions on sedimentation behavior of $TiO_2$NPs. The displacement reactions on the AA– (a), CA– (b) coated $TiO_2$ NPs with HA make the particles more stable (top) and smaller (bottom). However, HA is not able to displace BSA– (c) and it is shown not to affect the stability of the nanoparticle solution.

agglomerate size decreasing from 350 to 250 nm. However, BSA has a strong interaction with $TiO_2$ NPs and enhance the electrostatic repulsion of $TiO_2$ NPs, resulting in the high stability of $TiO_2$ suspension, shown in Figure 3.7c. Although the stability stays the same for BSA-coated NPs, the addition of HA causes an increase in the hydrodynamic diameters from ca. 275 to 600 nm. At pH 7.5, the ligands on the surface are negatively charged. Therefore, the repulsive force in between each particle promotes the stability of these NPs in aqueous suspensions.[44, 52, 71, 83]

## 3.5 Conclusions

The adsorption of different environmentally and biologically relevant molecules onto $TiO_2$ NP surfaces has been systematically investigated. The ATR–FTIR measurements show that different functional group such as phenol, carboxylate, and enediol are involved in the adsorption process. The desorption data suggest that under the conditions used in this study, AA and CA are able to reversibly and partially reversibly adsorb on $TiO_2$ surface, respectively. In contrast, BSA and HA mostly adsorb on the surface in an irreversible process monolayer, which is supported by the results from QCM-D. An interesting observation is that HA changes its conformation during adsorption process, reflected in the continuous increase of the dissipation. The properties of $TiO_2$ NPs are expected to be changed by NOM in the environment. Therefore, we focused on the displacement of different coatings on $TiO_2$ NPs with HA as it is a model for NOM found in the environment. Based on our study, the interaction between the small molecules and the surfaces of nanomaterials is reversible and HA can easily displace these molecules either fully or partially. However, the protein coated NPs shows no displacement but instead co-adsorbs with HA. Along with different coated $TiO_2$ NPs, 2D-COS provides relevant insights on the mechanism for the displacement reactions. In general, HA interacts with coated molecules first by weak interaction e.g. H-bonding and displaces these molecules by forming strong bonds with phenol and

carboxylate groups. The effects of displacement reactions on sedimentation and agglomeration were studied. The results show that $TiO_2$ NPs with different coatings displayed a slower sedimentation rate in presence of HA. The hydrodynamic diameters of $TiO_2$ NPs were also modified by HA. These all imply that NOM can stabilize released NPs and influence the fate of NPs in the environment. The study shows not only the effect of NOM on sedimentation and agglomeration of coated NPs but also provides a first look on how displacement reactions may occur in the environment.

## 3.6 Acknowledgements

This material is based on the work supported by the National Science Foundation under grant number CHE1606607. This work was performed in part at the San Diego Nanotechnology Infrastructure (SDNI) of UCSD, a member of the National Nanotechnology Coordinated Infrastructure, which is supported by the National Science Foundation (Grant ECCS-1542148). Any opinions, findings, and conclusions or recommendations expressed in this material are those of the authors and do not necessarily reflect the views of the National Science Foundation.

Chapter 3 is in full reproduced with permission from Royal Chemical Society: Haibin Wu, Natalia I Gonzalez-Pech, Vicki H Grassian. "Displacement reactions between environmentally and biologically relevant ligands on $TiO_2$ nanoparticles: insights into the aging of nanoparticles in the environment" Environmental Science: Nano, vol 6, 2019.

3.7 References


1. Zhou Q, Zhong YH, Chen X, Liu JH, Huang XJ, Wu YC. Adsorption and photocatalysis removal of fulvic acid by $TiO_2$–graphene composites. *Journal of Materials Science* 2014, 49(3): 1066-1075.

2. Dolamic I, Bürgi T. In situ ATR-IR study on the photocatalytic decomposition of amino acids over Au/$TiO_2$ and $TiO_2$. *The Journal of Physical Chemistry C* 2011, 115(5): 2228-2234.

3. Jose R, Thavasi V, Ramakrishna S. Metal oxides for dye-sensitized solar cells. *Journal of the American Ceramic Society* 2009, 92(2): 289-301.

4. Jang HD, Kim SK, Chang H, Roh KM, Choi JW, Huang Jx. A glucose biosensor based on $TiO_2$–Graphene composite. *Biosensors and Bioelectronics* 2012, 38(1): 184-188.

5. Olariu CI, Yiu HHP, Bouffier L, Nedjadi T, Costello E, Williams SR, Halloran CM, Rosseinsky MJ. Multifunctional $Fe_3O_4$ nanoparticles for targeted bi-modal imaging of pancreatic cancer. *Journal of Materials Chemistry* 2011, 21(34): 12650-12659.

6. Javed KR, Ahmad M, Ali S, Butt MZ, Nafees M, Butt AR, Nadeem M, Shahid A. Comparison of doxorubicin anticancer drug loading on different metal oxide nanoparticles. *Medicine* 2015, 94(11): e617.

7. Sharma H, Kumar K, Choudhary C, Mishra PK, Vaidya B. Development and characterization of metal oxide nanoparticles for the delivery of anticancer drug. *Artificial Cells, Nanomedicine, and Biotechnology* 2016, 44(2): 672-679.

8. Garner KL, Suh S, Keller AA. Assessing the risk of engineered nanomaterials in the environment: development and application of the nanofate model. *Environmental Science & Technology* 2017, 51(10): 5541-5551.

9. Feng X, Yan Y, Wan B, Li W, Jaisi DP, Zheng L, Zhang J, Liu F. Enhanced dissolution and transformation of ZnO nanoparticles: the role of inositol hexakisphosphate. *Environmental Science & Technology* 2016, 50(11): 5651-5660.

10. Gankanda A, Cwiertny DM, Grassian VH. Role of atmospheric $CO_2$ and $H_2O$ adsorption on ZnO and CuO nanoparticle aging: formation of new surface phases and the impact on nanoparticle dissolution. *The Journal of Physical Chemistry C* 2016, 120(34): 19195-19203.

11. Ma R, Stegemeier J, Levard C, Dale JG, Noack CW, Yang T, Brown GE, Lowry GV. Sulfidation of copper oxide nanoparticles and properties of resulting copper sulfide. *Environmental Science: Nano* 2014, 1(4): 347.

12. Ma R, Levard C, Marinakos SM, Cheng Y, Liu J, Michel FM, Brown GE, Lowry GV. Size-controlled dissolution of organic-coated silver nanoparticles. *Environmental Science & Technology* 2012, 46(2): 752-759.

13. Sendra M, Yeste MP, Gatica JM, Moreno-Garrido I, Blasco J. Homoagglomeration and heteroagglomeration of $TiO_2$, in nanoparticle and bulk form, onto freshwater and marine microalgae. *Science of the Total Environment* 2017, 592: 403-411.

14. Hedberg J, Ekvall MT, Hansson L-A, Cedervall T, Odnevall Wallinder I. Tungsten carbide nanoparticles in simulated surface water with natural organic matter: dissolution, agglomeration, sedimentation and interaction with Daphnia magna. *Environmental Science: Nano* 2017, 4(4): 886-894.

15. Smijs TG, Pavel S. Titanium dioxide and zinc oxide nanoparticles in sunscreens: focus on their safety and effectiveness. *Nanotechnology, science and applications* 2011, 4: 95-112.

16. Daghrir R, Drogui P, Robert D. Modified $TiO_2$ for environmental photocatalytic applications: a review. *Industrial & Engineering Chemistry Research* 2013, 52(10): 3581-3599.

17. Wang Y, Wang Q, Zhan X, Wang F, Safdar M, He J. Visible light driven type II heterostructures and their enhanced photocatalysis properties: a review. *Nanoscale* 2013, 5(18): 8326-8339.

18. Marks R, Yang T, Westerhoff P, Doudrick K. Comparative analysis of the photocatalytic reduction of drinking water oxoanions using titanium dioxide. *Water Research* 2016, 104: 11-19.

19. Li Z, Yang R, Yu M, Bai F, Li C, Wang ZL. Cellular level biocompatibility and biosafety of ZnO nanowires. *The Journal of Physical Chemistry C* 2008, 112(51): 20114-20117.

20. Ji Z, Jin X, George S, Xia T, Meng H, Wang X, Suarez E, Zhang H, Hoek EMV, Godwin H, Nel AE, Zink JI. Dispersion and stability optimization of $TiO_2$ nanoparticles in cell culture media. *Environmental Science & Technology* 2010, 44(19): 7309-7314.

21. Ramani M, Mudge MC, Morris RT, Zhang Y, Warcholek SA, Hurst MN, Riviere JE, DeLong RK. Zinc oxide nanoparticle–poly I:C RNA Complexes: implication as

therapeutics against experimental melanoma. *Molecular Pharmaceutics* 2017, 14(3): 614-625.

22. Singh S, D'Britto V, Bharde A, Sastry M, Dhawan A, Prasad BLV. Bacterial synthesis of photocatalytically active and biocompatible $TiO_2$ and ZnO nanoparticles. *International Journal of Green Nanotechnology: Physics and Chemistry* 2010, 2(2): 80-99.

23. Yang Y, Doudrick K, Bi X, Hristovski K, Herckes P, Westerhoff P, Kaegi R. Characterization of food-grade titanium dioxide: the presence of nanosized particles. *Environmental Science & Technology* 2014, 48(11): 6391-6400.

24. Du W, Sun Y, Ji R, Zhu J, Wu J, Guo H. $TiO_2$ and ZnO nanoparticles negatively affect wheat growth and soil enzyme activities in agricultural soil. *Journal of Environmental Monitoring* 2011, 13(4): 822-828.

25. Ghosh M, Chakraborty A, Mukherjee A. Cytotoxic, genotoxic and the hemolytic effect of titanium dioxide ($TiO_2$) nanoparticles on human erythrocyte and lymphocyte cells in vitro. *Journal of Applied Toxicology* 2013, 33(10): 1097-1110.

26. Fang T, Yu LP, Zhang WC, Bao SP. Effects of humic acid and ionic strength on $TiO_2$ nanoparticles sublethal toxicity to zebrafish. *Ecotoxicology* 2015, 24(10): 2054-2066.

27. Xiong S, Tang Y, Ng HS, Zhao X, Jiang Z, Chen Z, Ng KW, Loo SCJ. Specific surface area of titanium dioxide ($TiO_2$) particles influences cyto- and photo-toxicity. *Toxicology* 2013, 304: 132-140.

28. Zhou Z, Son J, Harper B, Zhou Z, Harper S. Influence of surface chemical properties on the toxicity of engineered zinc oxide nanoparticles to embryonic zebrafish. *Beilstein Journal of Nanotechnology* 2015, 6: 1568-1579.

29. Praetorius A, Scheringer M, Hungerbühler K. Development of environmental fate models for engineered nanoparticles—a case study of $TiO_2$ nanoparticles in the Rhine River. *Environmental Science & Technology* 2012, 46(12): 6705-6713.

30. Labille J, Feng J, Botta C, Borschneck D, Sammut M, Cabie M, Auffan M, Rose J, Bottero J-Y. Aging of $TiO_2$ nanocomposites used in sunscreen. dispersion and fate of the degradation products in aqueous environment. *Environmental Pollution* 2010, 158(12): 3482-3489.

31. Van Ravenzwaay B, Landsiedel R, Fabian E, Burkhardt S, Strauss V, Ma-Hock L. Comparing fate and effects of three particles of different surface properties: nano-$TiO_2$, pigmentary $TiO_2$ and quartz. *Toxicology Letters* 2009, 186(3): 152-159.

32. Gallego-Urrea JA, Perez Holmberg J, Hassellov M. Influence of different types of natural organic matter on titania nanoparticle stability: effects of counter ion concentration and pH. *Environmental Science: Nano* 2014, 1(2): 181-189.

33. Loosli F, Le Coustumer P, Stoll S. Effect of natural organic matter on the disagglomeration of manufactured $TiO_2$ nanoparticles. *Environmental Science: Nano* 2014, 1(2): 154-160.

34. Domingos RF, Tufenkji N, Wilkinson KJ. Aggregation of titanium dioxide nanoparticles: role of a fulvic acid. *Environmental Science & Technology* 2009, 43(5): 1282-1286.

35. Chowdhury I, Cwiertny DM, Walker SL. Combined factors influencing the aggregation and deposition of nano-$TiO_2$ in the presence of humic acid and bacteria. *Environmental Science & Technology* 2012, 46(13): 6968-6976.

36. Domingos RF, Rafiei Z, Monteiro CE, Khan MAK, Wilkinson KJ. Agglomeration and dissolution of zinc oxide nanoparticles: role of pH, ionic strength and fulvic acid. *Environmental Chemistry* 2013, 10(4): 306-312.

37. Chen G, Liu X, Su C. Distinct effects of humic acid on transport and retention of $TiO_2$ rutile nanoparticles in saturated sand columns. *Environmental Science & Technology* 2012, 46(13): 7142-7150.

38. Tang W-W, Zeng G-M, Gong J-L, Liang J, Xu P, Zhang C, Huang B-B. Impact of humic/fulvic acid on the removal of heavy metals from aqueous solutions using nanomaterials: a review. *Science of the Total Environment* 2014, 468–469: 1014-1027.

39. de Melo BAG, Motta FL, Santana MHA. Humic acids: structural properties and multiple functionalities for novel technological developments. *Materials Science and Engineering: C* 2016, 62: 967-974.

40. Kerndorff H, Schnitzer M. Sorption of metals on humic acid. *Geochimica et Cosmochimica Acta* 1980, 44(11): 1701-1708.

41. Hering JG, Morel FMM. Humic acid complexation of calcium and copper. *Environmental Science & Technology* 1988, 22(10): 1234-1237.

42. Yang K, Lin D, Xing B. Interactions of humic acid with nanosized inorganic oxides. *Langmuir* 2009, 25(6): 3571-3576.

43. Sposito G. *The surface chemistry of soils*. Oxford University Press: New York, 1984.

44. Jayalath S, Wu H, Larsen SC, Grassian VH. Surface Adsorption of Suwannee River Humic Acid on $TiO_2$ Nanoparticles: A Study of pH and Particle Size. *Langmuir* 2018, 34(9): 3136-3145.

45. Chen W, Qian C, Liu X, Yu H. Two-dimensional correlation spectroscopic analysis on the interaction between humic acids and $TiO_2$ nanoparticles. *Environmental Science & Technology* 2014, 48(19): 11119-11126.

46. Long M, Brame J, Qin F, Bao J, Li Q, Alvarez PJJ. Phosphate changes effect of humic acids on $TiO_2$ photocatalysis: from inhibition to mitigation of electron–hole recombination. *Environmental Science & Technology* 2017, 51(1): 514-521.

47. Drosos M, Ren M, Frimmel FH. The effect of NOM to TiO2: interactions and photocatalytic behavior. *Applied Catalysis B: Environmental* 2015, 165: 328-334.

48. Bian S-W, Mudunkotuwa IA, Rupasinghe T, Grassian VH. Aggregation and dissolution of 4 nm ZnO nanoparticles in aqueous environments: influence of pH, ionic strength, size, and adsorption of humic acid. *Langmuir* 2011, 27(10): 6059-6068.

49. Lin D, Ji J, Long Z, Yang K, Wu F. The influence of dissolved and surface-bound humic acid on the toxicity of TiO2 nanoparticles to Chlorella sp. *Water Research* 2012, 46(14): 4477-4487.

50. Mudunkotuwa IA, Grassian VH. Biological and environmental media control oxide nanoparticle surface composition: the roles of biological components (proteins and amino acids), inorganic oxyanions and humic acid. *Environ Sci: Nano* 2015, 2(5): 429-439.

51. Mudunkotuwa IA, Minshid AA, Grassian VH. ATR–FTIR spectroscopy as a tool to probe surface adsorption on nanoparticles at the liquid-solid interface in environmentally and biologically relevant media. *Analyst* 2014, 139(5): 870-881.

52. Mudunkotuwa IA, Grassian VH. Citric acid adsorption on $TiO_2$ nanoparticles in aqueous suspensions at acidic and circumneutral pH: surface coverage, surface speciation, and its impact on nanoparticle−nanoparticle Interactions. *Journal of the American Chemical Society* 2010, 132(42): 14986-14994.

53. Bian SW, Mudunkotuwa IA, Rupasinghe T, Grassian VH. Aggregation and dissolution of 4 nm ZnO nanoparticles in aqueous environments: influence of pH, ionic strength, size, and adsorption of humic acid. *Langmuir* 2011, 27(10): 6059-6068.

54. Mudunkotuwa IA, Rupasinghe T, Wu C-M, Grassian VH. Dissolution of zno nanoparticles at circumneutral ph: A study of size effects in the presence and absence of citric acid. *Langmuir* 2012, 28(1): 396-403.

55. Tsai D-H, Davila-Morris M, DelRio FW, Guha S, Zachariah MR, Hackley VA. Quantitative determination of competitive molecular adsorption on gold nanoparticles using attenuated total reflectance–fourier transform infrared spectroscopy. *Langmuir* 2011, 27(15): 9302-9313.

56. Gonzalez-Pech NI, Grassian VH. Surface Chemical Functionalities of Environmental Nanomaterials. In: Wandelt K, editor. *Encyclopedia of Interfacial Chemistry: Surface Science and Electrochemistry*: Elsevier; 2018. pp. 817-828.

57. Szeto YT, Tomlinson B, Benzie IFF. Total antioxidant and ascorbic acid content of fresh fruits and vegetables: implications for dietary planning and food preservation. *British Journal of Nutrition* 2007, 87(1): 55-59.

58. Administration USFaD. FDA investigations operations manual appendix C. Washington, DC; 2015.

59. Nasser F, Lynch I. Secreted protein eco-corona mediates uptake and impacts of polystyrene nanoparticles on Daphnia magna. *Journal of Proteomics* 2016, 137: 45-51.

60. Schmidt MP, Martínez CE. Kinetic and conformational insights of protein adsorption onto montmorillonite revealed using in situ ATR–FTIR /2D-COS. *Langmuir* 2016, 32(31): 7719-7729.

61. Noda I. Generalized two-dimensional correlation method applicable to infrared, raman, and other types of spectroscopy. *Applied Spectroscopy* 1993, 47(9): 1329-1336.

62. Noda I. Two-dimensional infrared (2D IR) spectroscopy: theory and applications. *Applied Spectroscopy* 1990, 44(4): 550-561.

63. Noda I, Ozaki Y. Principle of two-dimensional correlation spectroscopy. *Two-Dimensional Correlation Spectroscopy – Applications in Vibrational and Optical Spectroscopy*. John Wiley & Sons, Ltd, 2005, pp 15-38.

64. Baltrusaitis J, Jayaweera PM, Grassian VH. Sulfur Dioxide Adsorption on TiO2 Nanoparticles: Influence of Particle Size, Coadsorbates, Sample Pretreatment, and Light on Surface Speciation and Surface Coverage. *The Journal of Physical Chemistry C* 2011, 115(2): 492-500.

65. Reviakine I, Johannsmann D, Richter RP. Hearing what you cannot see and visualizing what you hear: Interpreting quartz crystal microbalance data from solvated interfaces. *Analytical Chemistry* 2011, 83(23): 8838-8848.

66. Vogt BD, Lin EK, Wu W-l, White CC. Effect of film thickness on the validity of the Sauerbrey equation for hydrated polyelectrolyte films. *The Journal of Physical Chemistry B* 2004, 108(34): 12685-12690.

67. Sauerbrey G. Verwendung von Schwingquarzen zur Wägung dünner Schichten und zur Mikrowägung. *Zeitschrift fur Physik* 1959, 155(2): 206-222.

68. Philippe A, Schaumann GE. Interactions of Dissolved Organic Matter with Natural and Engineered Inorganic Colloids: A Review. *Environmental Science & Technology* 2014, 48(16): 8946-8962.

69. Rajh T, Nedeljkovic JM, Chen LX, Poluektov O, Thurnauer MC. Improving optical and charge separation properties of nanocrystalline $TiO_2$ by surface modification with vitamin C. *The Journal of Physical Chemistry B* 1999, 103(18): 3515-3519.

70. Xagas AP, Bernard MC, Hugot-Le Goff A, Spyrellis N, Loizos Z, Falaras P. Surface modification and photosensitisation of $TiO_2$ nanocrystalline films with ascorbic acid. *Journal of Photochemistry and Photobiology A: Chemistry* 2000, 132(1–2): 115-120.

71. Ou Y, Lin J-D, Zou H, Liao D. Effects of surface modification of $TiO_2$ with ascorbic acid on photocatalytic decolorization of an azo dye reactions and mechanisms. *Journal of Molecular Catalysis A: Chemical* 2005, 241(1-2): 59-64.

72. Park J-W, Shumaker-Parry JS. Structural study of citrate layers on gold nanoparticles: role of intermolecular interactions in stabilizing nanoparticles. *Journal of the American Chemical Society* 2014, 136(5): 1907-1921.

73. Erhayem M, Sohn M. Stability studies for titanium dioxide nanoparticles upon adsorption of Suwannee River humic and fulvic acids and natural organic matter. *Science of the Total Environment* 2014, 468–469: 249-257.

74. Abrosimova KV, Shulenina OV, Paston SV. FTIR study of secondary structure of bovine serum albumin and ovalbumin. *Journal of Physics: Conference Series* 2016, 769(1): 012016.

75. Turci F, Ghibaudi E, Colonna M, Boscolo B, Fenoglio I, Fubini B. An Integrated Approach to the Study of the Interaction between Proteins and Nanoparticles. *Langmuir* 2010, 26(11): 8336-8346.

76. Xu Z, Grassian VH. Bovine serum albumin adsorption on tio2 nanoparticle surfaces: Effects of ph and coadsorption of phosphate on protein–surface interactions and protein structure. *The Journal of Physical Chemistry C* 2017, 121(39): 21763-21771.

77. Tsai D-H, DelRio FW, Keene AM, Tyner KM, MacCuspie RI, Cho TJ, Zachariah MR, Hackley VA. Adsorption and conformation of serum albumin protein on gold nanoparticles investigated using dimensional measurements and in situ spectroscopic methods. *Langmuir* 2011, 27(6): 2464-2477.

78. Dobson KD, McQuillan AJ. In situ infrared spectroscopic analysis of the adsorption of aliphatic carboxylic acids to $TiO_2$, $ZrO_2$, $Al_2O_3$, and $Ta_2O_5$ from aqueous solutions. *Spectrochimica Acta Part A: Molecular and Biomolecular Spectroscopy* 1999, 55(7): 1395-1405.

79. Dobson KD, McQuillan AJ. In situ infrared spectroscopic analysis of the adsorption of aromatic carboxylic acids to $TiO_2$, $ZrO_2$, $Al_2O_3$, and $Ta_2O_5$ from aqueous solutions. *Spectrochimica Acta Part A: Molecular and Biomolecular Spectroscopy* 2000, 56(3): 557-565.

80. Baes AU, Bloom PR. Diffuse reflectance and transmission fourier transform infrared (DRIFT) spectroscopy of humic and fulvic acids. *Soil Science Society of America Journal* 1989, 53(3): 695-700.

81. Yohannan Panicker C, Tresa Varghese H, Philip D. FT-IR, FT-Raman and SERS spectra of vitamin C. *Spectrochimica Acta Part A: Molecular and Biomolecular Spectroscopy* 2006, 65(3–4): 802-804.

82. Hvoslef J, Klæboe P. Vibrational spectroscopic studies of L-ascorbic acid and sodium ascorbate. *Acta Chemica Scandinavica* 1971, 25: 3043-3053.

83. Márquez A, Berger T, Feinle A, Hüsing N, Himly M, Duschl A, Diwald O. Bovine serum albumin adsorption on TiO2 colloids: the effect of particle agglomeration and surface composition. *Langmuir* 2017, 33(10): 2551-2558.

84. Grdadolnik J, Maréchal Y. Bovine serum albumin observed by infrared spectrometry. I. methodology, structural investigation, and water uptake. *Biopolymers* 2001, 62(1): 40-53.

85. Tajmir-Riahi HA. Coordination chemistry of vitamin C. Part I. Interaction of L-ascorbic acid with alkaline earth metal ions in the crystalline solid and aqueous solution. *Journal of Inorganic Biochemistry* 1990, 40(2): 181-188.

86. Berg RW. Investigation of L(+)-ascorbic acid with Raman spectroscopy in visible and UV light. *Applied Spectroscopy Reviews* 2015, 50(3): 193-239.

87. Eita M. In situ study of the adsorption of humic acid on the surface of aluminium oxide by QCM-D reveals novel features. *Soft Matter* 2011, 7(2): 709-715.

88. Dixon MC. Quartz crystal microbalance with dissipation monitoring: Enabling real-time characterization of biological materials and their interactions. *Journal of Biomolecular Techniques : JBT* 2008, 19(3): 151-158.

89. Johannsmann D. Viscoelastic, mechanical, and dielectric measurements on complex samples with the quartz crystal microbalance. *Physical Chemistry Chemical Physics* 2008, 10(31): 4516-4534.

90. McNamara TP, Blanford CF. A sensitivity metric and software to guide the analysis of soft films measured by a quartz crystal microbalance. *Analyst* 2016, 141(10): 2911-2919.

91. Zhang B, Wang Q. Quartz crystal microbalance with dissipation. *Nanotechnology research methods for foods and bioproducts*. Wiley-Blackwell, 2012, pp 181-194.

92. Zhao J, Wang Z, Ghosh S, Xing B. Phenanthrene binding by humic acid–protein complexes as studied by passive dosing technique. *Environmental Pollution* 2014, 184: 145-153.

93. Armanious A, Aeppli M, Sander M. Dissolved organic matter adsorption to model surfaces: adlayer formation, properties, and dynamics at the nanoscale. *Environmental Science & Technology* 2014, 48(16): 9420-9429.

94. Tomaszewski JE, Schwarzenbach RP, Sander M. Protein encapsulation by humic substances. *Environmental Science & Technology* 2011, 45(14): 6003-6010.

95. Noda I, Ozaki Y. Practical computation of two-dimensional correlation spectra. *Two-Dimensional Correlation Spectroscopy – Applications in Vibrational and Optical Spectroscopy*. John Wiley & Sons, Ltd, 2005, pp 39-46.

96. Nowack B, Bucheli TD. Occurrence, behavior and effects of nanoparticles in the environment. *Environmental Pollution* 2007, 150(1): 5-22.

97. Godinez IG, Darnault CJG. Aggregation and transport of nano-$TiO_2$ in saturated porous media: effects of pH, surfactants and flow velocity. *Water Research* 2011, 45(2): 839-851.

98. Li S, Sun W. A comparative study on aggregation/sedimentation of $TiO_2$ nanoparticles in mono- and binary systems of fulvic acids and Fe(III). *Journal of Hazardous materials* 2011, 197: 70-79.

# Chapter 4 Mechanistic study of oil adsorption onto PVP-coated magnetic nanoparticles: An integrated experimental and molecular dynamics study to inform remediation

## 4.1 Abstract

Nanotechnology has recently sparked considerable interest as a cleanup technique for oil remediation.[1-6] Although several studies have been reported in this area,[7-10] the mechanisms of the surface processes involved in the adsorption of oil onto nanoparticles (NPs) are still not clearly elucidated. Here, we combine molecular dynamics (MD) simulations and experimental data using ATR-FTIR spectroscopy to show that polyvinylpyrrolidone (PVP) polymer interacts physically with magnetite cluster via van der Waals with an average binding strength of –9.2 kcal/mol. The results indicate that the adsorption of crude oil onto PVP-coated magnetic NPs is thermodynamically favorable with an adsorption free energy of –3.6 kcal/mol. However, crude oil adsorption reduces in the presence of fulvic acid (FA), which is attributed to the ability of FA to partially displace PVP in seawater and form a new coating layer on the magnetite surface. Our work highlights the implications of molecular interactions and environmental conditions on the adsorption of crude oil onto NPs, which is critical for the effective design of nano-based oil remediation strategies.

## 4.2 Introduction

The application of nanoparticles (NPs) for oil removal from oil spills and wastes has been widely studied[11, 12] due to the limitations in traditional clean up techniques.[13-15] The majority of studies have however been conducted under simple laboratory conditions (*e.g.*, ultra-pure water) and the behavior and performance of NPs under real conditions have rarely been investigated.[16, 17] In order to assess the practical application of NPs for oil remediation, studies under relevant environmental conditions must be explored to evaluate the effectiveness of NP-based remediation

techniques. Moreover, the mechanisms of the surface processes involved in the adsorption of oil onto magnetic NPs must be elucidated under such environmentally relevant conditions. Atomistic simulations can provide unique insight of the molecular interactions between NPs and crude oil to elucidate adsorption mechanisms, which is critical for the effective design of nano-based remediation strategies. Molecular dynamics (MD) simulations have been extensively used to evaluate intermolecular binding and adsorption mechanisms between different NPs and various adsorbates.[18-21] MD simulations can provide microscopic-level description of NP-adsorbent interactions to rationalize experimental findings. For instance, Bürger et al. adopted MD simulations to establish that the adsorption of amino acids onto Fe-terminated magnetite-(111)-surface was energetically favorable and was predominately due to electrostatic interactions.[20]

In the present study, we use Attenuated Total Reflection Fourier Transform Infrared (ATR–FTIR ) spectroscopy and MD simulations to investigate the surface processes involved in using NPs for the successful removal of oil from the aqueous phase.[22-25] A combination of experimental studies and computational modeling is useful for probing mechanisms at different scales to improve data quality and depth and provide confidence in data. This approach is expected to provide insight on the nature and strength of PVP interaction with $Fe_3O_4$ cluster, as well as crude oil adsorption onto magnetite NPs under realistic environmental conditions.

## 4.3 Methods

### 4.3.1 Experimental.

*Materials*. The preparation of synthetic seawater follows the EPA recommended seawater composition: Milli–Q water, sodium chloride (NaCl, Fisher Chemicals, ACS grade), sodium sulfate ($Na_2SO_4$, Fisher Chemicals, ACS grade), potassium chloride (KCl, Fisher Chemicals, ACS grade), potassium bromide (KBr, Aldrich, 99%), sodium tetraborate decahydrate

($Na_2B_4O_7 \cdot 10H_2O$, 99%+), magnesium chloride hexahydrate ($MgCl_2 \cdot 6H_2O$, Fisher Chemicals, ACS grade), calcium chloride dehydrate ($CaCl_2 \cdot 2H_2O$, MP Biomedicals, 99%), strontium chloride hexahydrate ($SrCl_2 \cdot 6H_2O$, Avantor, ACS grade), and sodium bicarbonate ($NaHCO_3$, Fisher Chemicals, ACS grade). All solutions containing organic compounds were prepared using synthetic seawater. In this study, crude oil, a representative of Deepwater Horizon oil spill (reference MC 252 surrogate oil, sample ID: A0068H, AECOM Environment) was used. Also, Suwannee River fulvic acid (International Humic Substances Society) was used to represent natural organic macromolecules present in ocean water.

*NPs synthesis.* PVP-coated magnetic NPs were synthesized using a modified hydrothermal method previously reported.[7] In summary, 0.18 mmol of PVP (Mw 10 kDa, Sigma-Aldrich) was added to 6.25 ml ultrapure water while the solution was stirred at 80 ± 5 ºC. 1 mmol of $FeCl_2.4H_2O$ (98%, Alfa Aesar) and 4 mmol of $FeCl_3 \bullet 6H_2O$ (>98%, BDH) were added to the solution and stirred while the temperature was kept constant. Next, 0.12 mmol PVP was dissolved and finally 6.25 mL ammonium hydroxide (28-30%, BDH) was added to the solution dropwise at room temperature while the solution was stirred. The suspension was mixed for 25 min at 90± 5 ºC and the precipitate was washed once with deionized water and separated by magnetic decantation to remove impurities. The NPs were re-dispersed in water again via sonication and stored for later use. The details of NPs characterization including atomic force microscopy (AFM), thermogravimetric analysis (TGA), Fourier transform infrared spectrometry (FTIR), dynamic light scattering (DLS), and X-ray powder diffraction (XRD) data have been published previously.[7, 8]

*Adsorption experiments.* ATR–FTIR spectra were recorded using a horizontal ATR cell with an AMTIR element (Pike Technologies Inc.). The cell was placed inside a Nicolet iS10 FTIR spectrometer equipped with an MCT–A detector. The NP film was made by drying 1 mL of the

as-synthesized $Fe_3O_4$ NP solution on an AMTIR crystal in a dry air environment overnight. Different solutions were then added to the cell with the NP film. A glass cover was placed over the flow cell followed by spectral collection. All spectra were collected by acquiring 1000 scans at an instrument resolution of 4 $cm^{-1}$ in the spectral range extending from 750 to 4000 $cm^{-1}$. For solution phase spectra, 1 mL seawater was added on the AMTIR crystal with a NP film. A glass cover was placed over the flow cell and a background spectrum was immediately collected. Next, the seawater was carefully removed after collecting a background, and 1 mL of FA (10 ppm, 20 ppm or 50 ppm) was added onto the same film. The spectra were collected after 2-hour adsorption. Crude oil mainly consists of saturated and unsaturated hydrocarbons and is immiscible in polar solvents such as water. In order to promote the adsorption of crude oil on $Fe_3O_4$ NPs, a crude oil suspension was rotated with dispersed NPs. For the spectrum of a dry PVP-$Fe_3O_4$ NP film after crude oil adsorption, 10 mL PVP coated NP solution was centrifuged for 10 min at 10,000 rpm to separate the NPs from the solution. Then, 10 mL of crude oil suspension (1.7 g/L) was added to the NPs after removing the supernatant. The solutions were sonicated for 30 min and placed onto a Cole-Parmer rotator for 48 hrs. After the adsorption, the NPs were re-dispersed in 10 mL Milli-Q water. 1mL of the NP solution was added onto an AMTIR crystal dry overnight in a dry air environment. In the case of FA–PVP–Fe3O4 NPs, the NPs were exposed to FA solution prior to crude oil adsorption. For the spectrum of a dry FA-PVP-$Fe_3O_4$ NP film after crude oil adsorption, the NPs were separated from 10 mL of stock solution by centrifugation and exposed to 10 mL of 50 ppm FA for 24 hrs. prior to crude oil adsorption. After adsorption process of FA, the NPs were re–dispersed in crude oil solution for 48 hrs. Afterwards, the NPs were centrifuged and dispersed in 10 mL Milli–Q water. 1 mL suspension of NPs in water was placed onto an AMTIR crystal drying overnight. The spectrum of dry film was collected to study crude oil adsorption.

4.3.2 Molecular models and simulations

The molecular model of the NP was constructed using the Atomsk modeling tool.[26] Because we are interested in the NP-PVP surface interactions, a cut-out of a 10 nm diameter NP was used in the molecular dynamics simulations to reduce computational time in the simulations. A PVP polymer model was constructed to match the experimental properties by sequencing 90 PVP units to form a PVP polymer chain. Initially, 3 PVP polymer chains were randomly located in a large periodic box and equilibrated to form a PVP polymer with the desired density. In this study, humic acid (HA) is chosen as a representative NOM molecule to investigate its influence on oil adsorption. The HA structure is based on the Temple-Northeastern-Birmingham (TNB) molecular model which consists of carboxyl, phenolic and amine functional groups.[27] The TNB HA has properties similar to Suwanee river NOM which was used in the experiments. All simulations were performed with the LAMMPS[28] computational package and results visualized using visual molecular dynamics.[29] For the simulations involving possible chemical reactions, a magnetite cluster with three $Fe_3O_4$ units with a PVP monomer was solvated in explicit water and simulated using the reaxFF force field[30] developed for amine iron oxide system.[31] The reaxFF force field has been widely used to simulate bond formation and breakage. For all other simulations, the consistent valence force field (CVFF)[32] was used to describe the interactions between the PVP polymer while the NP interactions were described using the clayFF forcefield.[33] The CVFF has been shown to be consistent with the clayFF force field. A PVP-NP complex was solvated in TIP3P water. Sodium, calcium, potassium and chloride ions were added to create a representative hard water and seawater systems. In our experiments, PVP is generally only slightly charged and the NPs are nearly uncharged at neutral pH, therefore, a near neutral pH is maintained in the simulations. The solvated systems were initially minimized for 10,000 steps and equilibrated at a

constant volume for 1 ns. The system was further equilibrated at a constant pressure of 1bar using Berendsen's barostat with the PVP atoms harmonically restrained with a force constant of 10 kcal/mol/Å. All atoms of the NP were fixed during the simulations. A 10 ns production simulation was conducted under the NVT ensemble without restraints on the PVP atoms at constant temperature and volume. The Langevin thermostat was used to maintain a temperature of 300 K in the simulations. The long-range electrostatic interactions were calculated using the particle-particle mesh solver[34] and the cutoff distance for the short-range Lennard-Jones interactions was set to 10 Å. All bonds involving hydrogen atoms were restrained to their equilibrium value using the SHAKE algorithm. Periodic boundary conditions were applied in all directions. The velocity Verlet scheme was adopted to propagate the equation of motions with a time step of 2 fs. In the umbrella sampling simulations, a harmonic restraint of 20 kcal/mol/Å was applied to restrain the center-to-center distances of the PVP and the respective adsorbates. The intermolecular distances were varied from the minimum separation to distances where interactions were negligible in 0.1 nm increments. Umbrella sampling windows were simulated for 1 ns saving data at 10 ps interval for analysis.

## 4.4 Results and Discussions

ATR–FTIR spectroscopy was employed to probe a PVP coated $Fe_3O_4$ NP film to study the interaction between PVP and $Fe_3O_4$ NPs, crude oil and PVP-coated NPs and investigate the stability of the coatings on $Fe_3O_4$ NPs in seawater under different environmental conditions. Here, we studied the adsorption and desorption mechanisms of PVP coatings on $Fe_3O_4$ NPs in seawater. The binding of a PVP monomer onto a magnetite cluster in seawater was simulated to probe the nature and strength of PVP-magnetite interactions. To effectively simulate the occurrence of possible chemical reactions between potential reactive points on the PVP and $(Fe_3O_4)_3$ molecules,

MD simulations coupled with umbrella sampling[35] were conducted to quantity the binding of the carbonyl oxygen in the PVP onto $Fe^{2+}$ and $Fe^{3+}$ atoms in the $(Fe_3O_4)_3$ cluster[36] (Technical details can be found in the Methods section). A mechanistic insight on crude oil interaction with PVP-coated NPs was obtained by conducting simulations to quantify the binding strength of crude oil onto PVP-coated NP in the presence of salt and natural organic matter (NOM) (representative of environmental conditions, where oil remediation would occur).

The result of the ATR–FTIR spectroscopy study is shown in Figure. 4.1a together with the simulation configuration (Figure. 4.1b) and the potential of mean force (PMF) describing the strength of PVP interaction with $Fe_3O_4$ as a function of interatomic distance (Figure. 4.1 c). As indicated in the spectra, the PVP coating (black line in Figure 4.1a) shows a broad absorption from 1200 – 1700 $cm^{-1}$ associated with different vibrational motions. For example, the peak at 1658

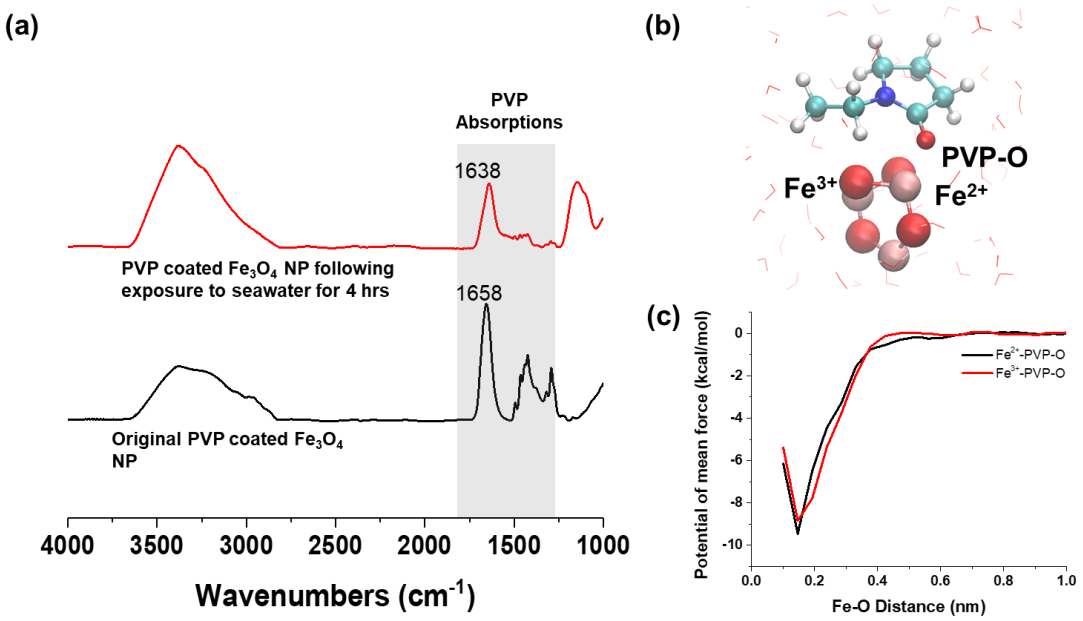


**Figure 4.1** (a) PVP Coating Stability. Baseline corrected ATR-FTIR spectra of a thin film of PVP-coated $Fe_3O_4$ NPs before (black) and after (red) exposure to seawater for 4 hrs. (b) PVP-$Fe_3O_4$ complex in water (c) PMF as a function of the distance between PVP-O and Fe. PVP and $(Fe_3O_4)_3$ are shown in CPK model and water molecules shown as lines.

$cm^{-1}$ is assigned to the stretching mode of the C=O in PVP and multipeaks from 1200 – 1600 $cm^{-1}$ (labeled in the light grey area) represent bending modes of CH or $CH_2$ groups.[37, 38]

It can be observed that, the bending modes of CH or $CH_2$ in PVP molecules[7, 39] in the range 1250 – 1700 $cm^{-1}$ diminishes after exposure to seawater indicating the partial desorption of PVP in seawater. The amount of PVP left on the NP surface following exposure to seawater is estimated to be ~10 % based on the integrated area of the peaks in the spectral area extending from 1250 to 1350 $cm^{-1}$. This frequency of carbonyl stretching in PVP on the NP surface is similar to the reported values for pure PVP, indicating that carbonyl functional groups may interact with metal cations on NP surface through electrostatic attraction or hydrogen bonds with hydroxyl groups on NP oxide surfaces.[40] The other broad absorption ca. 3400 $cm^{-1}$ is the stretching motion of O–H or adsorbed water on NPs, and the bending mode of water adsorbed on NP surfaces near 1638 $cm^{-1}$ is overlapped with PVP carbonyl absorption. It can be seen that absorption at 1658 $cm^{-1}$ shown in the PVP coated $Fe_3O_4$ film changes to ~1638 $cm^{-1}$ after exposure to seawater which is associated with the bending mode of adsorbed water or hydroxyl group on NP surfaces (red curve in Figure 4.1a), suggesting partial desorption of PVP from the NP surface. Thus, PVP is not strongly bound onto NP and partially desorbs from the NP surface when in contact with seawater.

This observation is consistent with the results of the simulations which suggest a physical interaction between PVP and $(Fe_3O_4)_3$ cluster. As shown in the PMF above, PVP-O interacts favorably with $Fe^{2+}$ and $Fe^{3+}$ atoms at a minimum interatomic separation of 0.15 nm with corresponding binding energies of –9.5 and –8.9 kcal/mol, respectively. A negative PMF value indicates attraction while a positive PMF represents repulsion relative to the free energy at a separation of 1.0 nm. As the interatomic distance increases, the PMF becomes flat indicating negligible interaction between Fe and PVP-O atoms. Although the computed PVP-$(Fe_3O_4)_3$

interactions are significant, experimental bond dissociation energies for Fe and PVP-O are on the order of 97.3 kcal/mol[41], which is significantly stronger than the resulting binding energies from the above PMFs. The weak binding of PVP onto $(Fe_3O_4)_3$ cluster suggests that interactions between $(Fe_3O_4)_3$ and PVP atoms are mainly physical, mostly due to Van der Waals interactions.[18] Thus, both experimental and simulation results indicate a weak binding of PVP onto $(Fe_3O_4)_3$ cluster in seawater suggesting that PVP is physically sorbed onto $(Fe_3O_4)_3$ in solution through multiple points of attachment.

Recent experimental studies have shown that PVP-coated NPs can be used to achieve nearly 100% oil removal from water.[7-9] In this study, simulations were performed to understand the mechanisms of oil removal by PVP-coated NP using nonane as a representative hydrocarbon. An initial molecular configuration of the system was built by randomly locating nonane molecule on the surface of a PVP-coated NP as shown in Figure 4.2a.

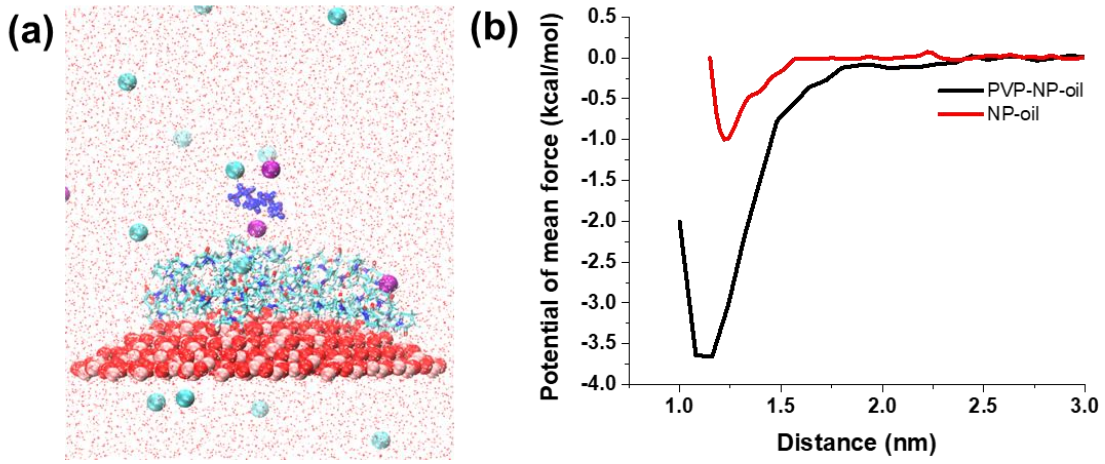


**Figure 4.2** (a) PVP-coated NP with oil in water (b) PMF as a function of the distance between PVP and oil. NP is shown in VDW model, PVP is shown in licorice model, oil is shown in blue licorice model, $Na^+$, $K^+$ and $Cl^-$ ions are shown as spheres and water molecules shown as red dots.

We first simulated nonane interaction with both uncoated and PVP-coated NPs to evaluate binding mechanisms and binding contributions from the different adsorbents. The resulting PMF is shown in Figure 4.2b as a function of the separation distance between PVP and oil. Due to the hydrophilic nature of the surface of the pristine NP, oil interaction with the uncoated NP is less favorable with a binding energy of only –1.0 kcal/mol. However, in the case of the of PVP-coated NP, there is an increased oil interaction, thus, the presence of the PVP coating significantly increased oil binding from –1.0 to –3.6 kcal/mol. The increased adsorption is attributed to the fact that oil sorption is likely driven by hydrophobic effect, with hydrophobic moieties of the PVP coating allowing preferential sorption of hydrocarbons from the oil-water mixture onto the PVP-

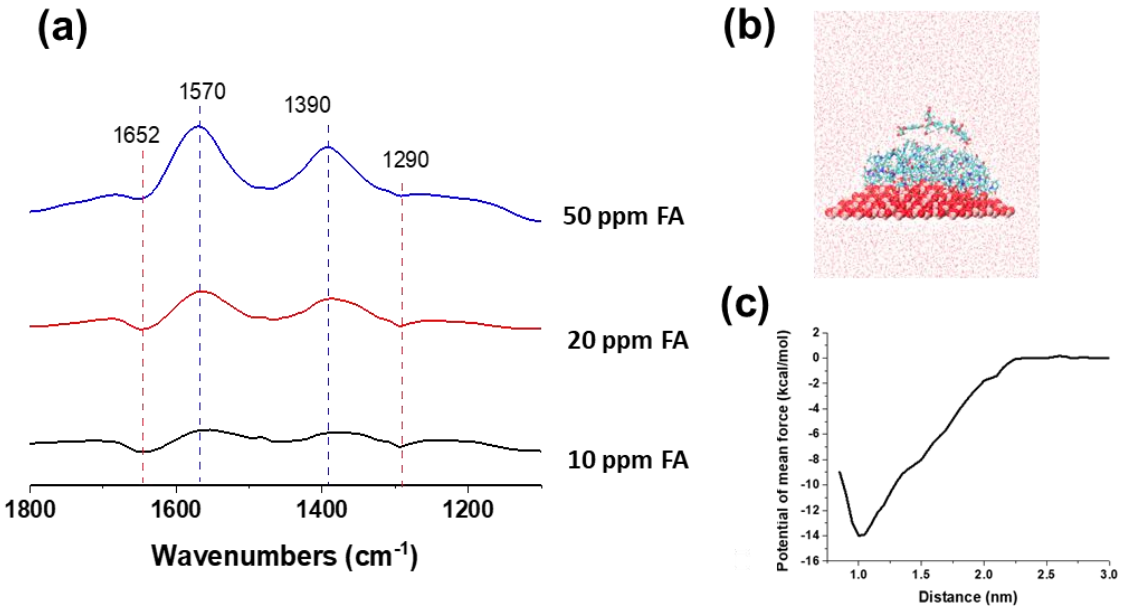


**Figure 4.3** (a) ATR-FTIR spectra of various concentrations of fulvic acid in seawater on PVP- $Fe_3O_4$ NP films. The spectra show that absorptions associated with FA carboxylate groups (at 1390 and 1570 $cm^{-1}$) increase with increasing FA concentrations labeled with blue dash lines. Simultaneously, PVP desorbs from the surface as shown by the negative features at 1290 and 1652 $cm^{-1}$ labeled with red dash lines. (b) PVP-coated NP-NOM complex in water (c) PMF as a function of the distance between NOM and PVP.

coated NPs.[42] It must be noted that due to the neutral pH condition maintained in the simulations, the binding of oil onto the PVP-coated NPs is primarily driven by Van der Waals interactions.

We also performed further experiments and simulations to investigate the effect of NOM on the adsorption of oil onto PVP–coated NPs. In our experiments, Suwannee River FA (SRFA) is chosen as a representative model of NOM with reasonable abundance in aqueous environments.[43] FA has a complex macromolecular structure with conjugated aromatic rings and polar functional groups (e.g. phenol, amide and carboxylic acid groups).[44] The interaction of FA and PVP–$Fe_3O_4$ NPs was investigated via ATR–FTIR by adding 1 mL synthetic seawater solutions containing various concentrations of FA at pH 7.9 on a PVP–$Fe_3O_4$ NP film after 2 hours adsorption. Figure 4.3a shows ATR–FTIR spectra of adsorbed FA on these NP films. As indicated in the figure, the two negative peaks observed in the spectra at 1290 and 1652 $cm^{-1}$ is due to the partial desorption of PVP. The peaks at 1390 and 1570 $cm^{-1}$ correspond to FA carboxylate symmetric and asymmetric stretching, respectively. Humic acid (HA) and FA have been reported to strongly bind onto metal oxide surface regardless of pre-coated molecules.[44, 45] These two types of NOM are able to chemically bind to metal oxide surfaces, via their multifunctional groups e.g. carboxylate and phenol.[44-46] Previous study shows FA strongly adsorbs on metal oxide surfaces, resulting in an irreversible adsorption onto metal oxide surface.[47] Our flowing ATR–FTIR results confirm that FA is able to adsorb on $Fe_3O_4$ NPs and the intensity does not show notable decrease after flowing seawater onto the FA adsorbed $Fe_3O_4$ NP film for 30 min (Figure. B1 in Appendix B). The simulation results indicate a favorable interaction between PVP coating and the simulated HA molecule in seawater (Figure 4.3b). As indicated in Figure 4.3c, HA strongly binds onto the PVP-coated NP surface with a free binding energy of –14.0 kcal/mol. Although the nature of this interaction is physical, with increased HA concentration, HA adsorption onto PVP-coated NP can

become irreversible and be classified as a pseudo-chemical interaction. The favorable interaction between HA and the PVP-coated NP indicates a strong affinity for the adsorption of HA onto $Fe_3O_4$ NPs as observed in the experiments.

The splitting of symmetric and asymmetric stretching of a carboxylate suggests the binding coordination of carboxylate onto a NP surface. The magnitude of splitting in this case around 180 $cm^{-1}$ in the spectra normally indicates a carboxylate is binding to a surface through a bridging mode in which a carboxylate group binds with two adjacent metal ions on the surface.[48, 49] We observed that negative desorption peaks of PVP and positive adsorption peaks border appear in the spectra when FA solution is placed on the PVP-$Fe_3O_4$ NP film. Thus, it is possible that FA adsorbs onto NPs simultaneously with the partial desorption of PVP from the iron oxide surface in seawater.

Our recent study indicates that FA can act as a competitive phase for either PVP or oil and reduce oil interaction with NPs.[8] To further probe the effect of this mechanism on oil adsorption, HA interaction with oil, PVP monomer and PVP-coated NP were simulated to quantify the binding strength for the different cases. As presented in Figure 4.4b, the interaction of HA with oil (snapshot shown in Figure 4.4a) is slightly stronger (–5.1 kcal/mol) than the interaction with PVP

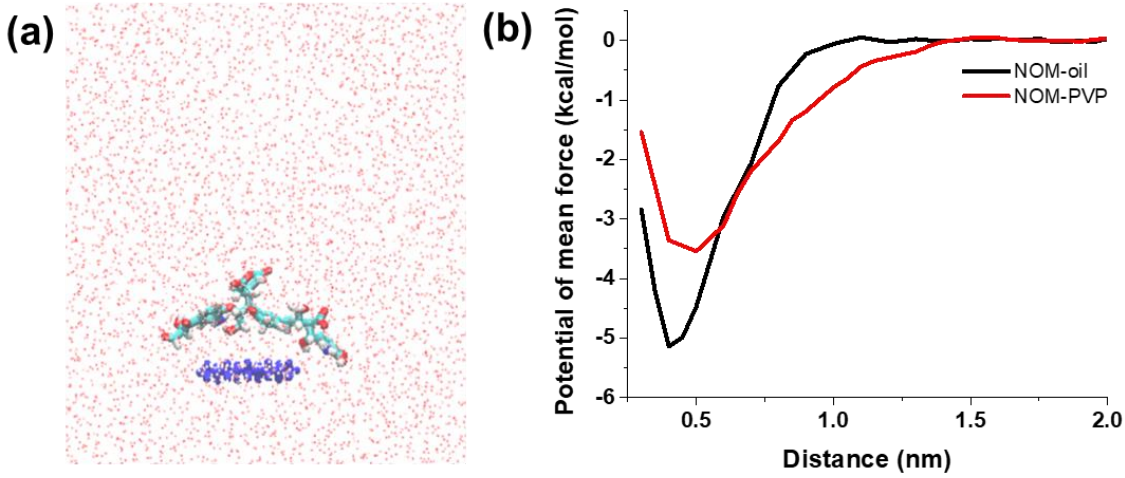


**Figure 4.4** (a) NOM-oil complex in water (b) PMF as a function of the distance between NOM and oil. NOM is shown in licorice model, oil is shown in blue licorice model and TIP3P water molecules shown as points.

(–3.5 kcal/mol) in the aqueous phase. The stronger binding between HA and oil suggest that the formation of HA-oil complexes is likely, which can lead to increased aqueous solubility of oil. The increased oil solubility will likely drive oil away from the surface of the PVP-coated NP to reduce oil removal from the aqueous phase.

The dry films of crude oil adsorbed NPs were investigated via ATR–FTIR spectra shown in Figure. 4.5. The three peaks observed in the 2800 to 3000 $cm^{-1}$ range are associated with C–H stretching vibrations, while the two peaks at 1381 and 1464 $cm^{-1}$ are associated with $CH_2$ and $CH_3$ deformation modes.[50] As observed in Figure 4.5, a comparison of the spectrum for the crude oil suspension in seawater (indicated in blue) with the other two spectra following adsorption indicates an increase in absorbance but no changes in frequency. This suggests that crude oil interacts with NPs mainly via hydrophobic interactions and the adsorption behavior is influenced by the presence of FA. It is evident that coatings on NPs favors adsorption of crude oil. However, the spectrum

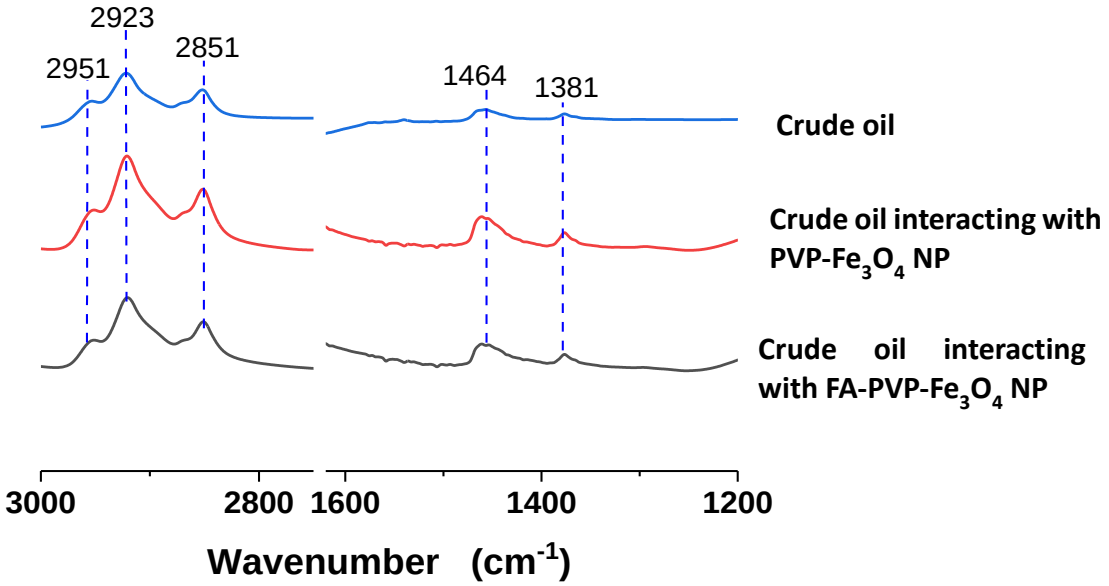


**Figure 4.5** Crude oil adsorption on PVP-$Fe_3O_4$ NPs in absence and presence of FA. ATR–FTIR spectra in the region extending from 1200 to 1610 and 2775 to 3000 $cm^{-1}$ of ~1.7 g/L crude oil solution (blue), a dry NP film after adsorption of crude oil on PVP–$Fe_3O_4$ NPs (red), and a dry NP film after adsorption of crude oil on FA –PVP–$Fe_3O_4$ NPs. These spectra show that FA does not impact crude oil adsorption on the NP surface.

following adsorption of crude oil on FA–PVP–$Fe_3O_4$ NPs shows slightly lower absorbance than the one on PVP–$Fe_3O_4$ NPs, indicating that the presence of FA may reduce the adsorption of oil in agreement with previous results.[7, 8] The favorable interaction between FA and PVP–$Fe_3O_4$ NPs makes FA a strong competitive adsorbate to potentially block oil adsorption onto NPs. It is possible that FA is more favorable to competitively adsorb onto the active sites than oil molecules inhibiting oil adsorption onto the NPs. Moreover, the slightly basic pH of seawater promotes deprotonation of the FA molecule, which can lead to increased polarity in the surface chemistry of the NP and result in reduced nonpolar hydrophobic interaction of oil molecules with the NPs.

The different surface processes involved in the adsorption of oil onto PVP-coated $Fe_3O_4$ NPs are presented in the schematic shown in Figure 4.6. As illustrated, the PVP coating on $Fe_3O_4$ NP is not stable in seawater and consequently, desorbs partially from the surface of the $Fe_3O_4$ NP. Thus, PVP partially desorbs from the surface in the presence of salt and FA, forming a new layer. In the presence of FA, FA molecules are able to displace PVP and form a new coating layer on the NP surface. It is worth noting that some PVP molecules may not be directly displaced by FA but through intermolecular interaction with FA due to steric effect on some sites. This results in co-

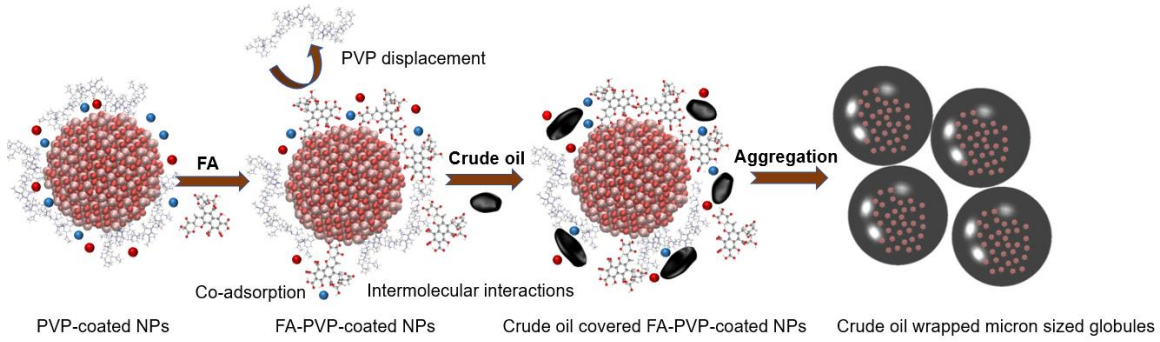


**Figure 4.6** Schematic of surface processes for PVP coated $Fe_3O_4$ NPs in the presence of FA and crude oil. The processes occur in an ion-rich environment representing by blue and dark red dots. Initial PVP is unstable in seawater and can be readily displaced by FA to form new FA-PVP coatings. The adsorbed crude oil on new coating surface aggregate into micron size globules with the help of the ions.[7]

adsorption and intermolecular interaction, which enables crude oil to be readily adsorbed onto the new surface through intermolecular interaction with FA. Moreover, as observed in our previous study[7], the crude oil covered NPs would further aggregate by forming micron sized globules in the presence of ions, which can result in increased crude oil adsorption. The mechanisms associated with NPs aggregation in being investigated via molecular dynamics simulations in our current studies. The results of an integrated experimental and MD simulations study have shown favorable adsorption of crude oil onto PVP-coated magnetic NPs in the presence of NOM. The results indicate that PVP is physically sorbed onto the surface of $(Fe_3O_4)_3$ cluster through multiple points of attachment via physical Van der Waals interactions. In the presence of FA, the PVP coating on the magnetic NPs is partially displaced, resulting in the formation of a new coating layer, which consequently reduces oil adsorption. The reduced oil adsorption is attributed to reduced non-polar hydrophobic interactions between oil molecules and the magnetic NPs surface. Thus, the presence of FA influences crude oil adsorption onto NPs via an interplay of co-adsorption and intermolecular interactions.

Chapter 4, in full, has been submitted for publication of the material as it may appear in Nature Nanotechnology, 2020, Linkel K. Boateng, Seyyedali Mirshahghassemi, Haibin Wu, Vicki H. Grassian, Joseph R.V. Flora, Jamie R. Lead. The dissertation author was the investigator and author of this paper. The dissertation author conducted the spectroscopic measurements and analysis. Dr. Linkel Boateng and Dr. Flora conducted the computational simulations. Dr. Seyyedali Mirshahghassemi provided the magnetite NPs for the research. I also acknowledge U of SC Research Cyberinfrastructure for the computational time used for the research.

4.5 References


1. Zhu Q, Pan Q, Liu F. Facile Removal and Collection of Oils from Water Surfaces through Superhydrophobic and Superoleophilic Sponges. *The Journal of Physical Chemistry C* 2011, 115(35): 17464-17470.

2. Calcagnile P, Fragouli D, Bayer IS, Anyfantis GC, Martiradonna L, Cozzoli PD, Cingolani R, Athanassiou A. Magnetically driven floating foams for the removal of oil contaminants from water. *ACS Nano* 2012, 6(6): 5413-5419.

3. Zhu Q, Tao F, Pan Q. Fast and selective removal of oils from water surface via highly hydrophobic core-shell Fe2O3@C nanoparticles under magnetic field. *ACS Applied Materials & Interfaces* 2010, 2(11): 3141-3146.

4. Duan B, Gao H, He M, Zhang L. Hydrophobic Modification on Surface of Chitin Sponges for Highly Effective Separation of Oil. *ACS Applied Materials & Interfaces* 2014, 6(22): 19933-19942.

5. Gu JJ, Jiang W, Wang FH, Chen MD, Mao JY, Xie T. Facile removal of oils from water surfaces through highly hydrophobic and magnetic polymer nanocomposites. *Applied Surface Science* 2014, 301: 492-499.

6. Zhu Q, Chu Y, Wang Z, Chen N, Lin L, Liu F, Pan Q. Robust superhydrophobic polyurethane sponge as a highly reusable oil-absorption material. *Journal of Materials Chemistry A* 2013, 1: 5386-5393.

7. Mirshahghassemi S, Lead JR. Oil Recovery from Water under Environmentally Relevant Conditions Using Magnetic Nanoparticles. *Environmental Science & Technology* 2015, 49(19): 11729-11736.

8. Mirshahghassemi S, Cai B, Lead JR. Evaluation of polymer-coated magnetic nanoparticles for oil separation under environmentally relevant conditions: effect of ionic strength and natural organic macromolecules. *Environmental Science: Nano* 2016, 3(4): 780-787.

9. Mirshahghassemi S, Ebner AD, Cai B, Lead JR. Application of high gradient magnetic separation for oil remediation using polymer-coated magnetic nanoparticles. *Separation and Purification Technology* 2017, 179: 328-334.

10. Mirshahghassemi S, Cai B, Lead JR. A Comparison between the Oil Removal Capacity of Polymer-Coated Magnetic Nanoparticles in Natural and Synthetic Environmental Samples *Environmental Science & Technology* 2019, 53: 4426-4432.

11. Su C. Environmental implications and applications of engineered nanoscale magnetite and its hybrid nanocomposites: A review of recent literature. *Journal of Hazardous Materials* 2016.

12. Lei W, Portehault D, Liu D, Qin S, Chen Y. Porous boron nitride nanosheets for effective water cleaning. *Nature Communications* 2013, 4: 1777.

13. National Commission on the BP Deepwater Horizon Oil Spill and Offshore Drilling, Deep Water: the Gulf Oil Disaster and the Future of Offshore Drilling. UNT Digital Library: Washington, D.C., 2014.

14. The Federal Interagency Solutions Group, Oil Budget Calculator Science and Engineering Team, Oil Budget Calculator, Deepwater Horizon-Technical Document. http://www.noaanews.noaa.gov/ stories2010/PDFs/OilBudgetCalc_Full_HQ-Print_111110.pdf . 2010.

15. Fritz DE. I*n Situ* Burning of Spilled Oil in Freshwater Inland Regions of the United States. *Spill science & technology bulletin* 2003, 8: 331-335.

16. Jiang G, Hu R, Wang X, Xi X, Wang R, Wei Z, Li X, Tang B. Preparation of superhydrophobic and superoleophilic polypropylene fibers with application in oil/water separation. *The Journal of The Textile Institute* 2013, 104(8): 790-797.

17. Song S, Yang H, Zhou C, Cheng J, Jiang Z, Lu Z, Miao J. Underwater superoleophobic mesh based on BiVO4 nanoparticles with sunlight-driven self-cleaning property for oil/water separation. *Chemical Engineering Journal* 2017, 320: 342-351.

18. Grasso G, Deriu MA, Prat M, Rimondini L, Verne E, Follenzi A, Danani A. Cell Penetrating Peptide Adsorption on Magnetite and Silica Surfaces: A Computational Investigation. *The Journal of Physical Chemistry B* 2015, 119: 8239-8246.

19. Park OK, Tiwary CS, Yang Y, Bhowmick S, Vinod S, Zhang Q, Colvin VL, Asif SAS, Vajtai R, Penev ES, Yakobsona BI, Ajayan PM. Magnetic field controlled graphene oxide-based origami with enhanced surface area and mechanical properties. *Nanoscale* 2017, 9: 6991-6997.

20. Bürger A, Magdans U, Gies H. Adsorption of amino acids on the magnetite-(111)-surface: a force field study. *Journal of Molecular Modeling* 2013, 19: 851–857.

21. Yue J, Jiang X, Yu A. Molecular Dynamics Study on Au/Fe3O4 Nanocomposites and Their Surface Function toward Amino Acids. . *The Journal of Physical Chemistry B* 2011, 115: 11693–11699.

22. Peijnenburg W, Baalousha M, Chen JW, Chaudry Q, Von der kammer F, Kuhlbusch TAJ, Lead J, Nickel C, Quik JTK, Renker M, Wang Z, Koelmans AA. A Review of the Properties and Processes Determining the Fate of Engineered Nanomaterials in the Aquatic Environment. *Critical Reviews in Environmental Science and Technology* 2015, 45: 2084-2134.

23. Loosli F, Le Coustumer P, Stoll S. Effect of electrolyte valency, alginate concentration and pH on engineered TiO2 nanoparticle stability in aqueous solution. *Science of the Total Environment* 2015, 535: 28-34.

24. Afshinnia K, Gibson I, Merrifield R, Baalousha M. The concentration-dependent aggregation of Ag NPs induced by cystine. *Science of the Total Environment* 2016, 557-558: 395-403.

25. Al-Hamadani YAJ, Chu KH, Son A, Heo J, Her N, Jang M, Park CM, Yoon Y. Stabilization and dispersion of carbon nanomaterials in aqueous solutions: A review. *Separation and Purification Technology* 2015, 156 (Part 2): 861-874.

26. Hirel P. Atomsk: A tool for manipulating and converting atomic data files. *Computer Physics Communications* 2015, 197: 212-219.

27. Sein LT, Varnum JM, Jansen SA. Conformational Modeling of a New Building Block of Humic Acid: Approaches to the Lowest Energy Conformer. *Environmental Science & Technology* 1999, 33(4): 546-552.

28. Plimpton S. Fast Parallel Algorithms for Short-Range Molecular Dynamics. *Journal of Computational Physics* 1995, 117: 1-19.

29. Humphrey W, Dalke A, Schulten K. VMD: visual molecular dynamics. *Journal of molecular graphics* 1996, 14(1): 33-38.

30. van Duin ACT, Dasgupta S, Lorant F, Goddard WA. ReaxFF: A Reactive Force Field for Hydrocarbons. *The Journal of Physical Chemistry A* 2001, 105(41): 9396-9409.

31. Chia CL. Classical and ReaxFF Molecular Dynamics Simulations of Fuel Additives at the Solid-fluid Interface. Doctoral thesis, University of Manchester, Manchester, 2018.

32. Kitson DH, Hagler AT. Theoretical studies of the structure and molecular dynamics of a peptide crystal. *Biochemistry* 1988, 27(14): 5246-5257.

33. Cygan RT, Liang J-J, Kalinichev AG. Molecular Models of Hydroxide, Oxyhydroxide, and Clay Phases and the Development of a General Force Field. *The Journal of Physical Chemistry B* 2004, 108(4): 1255-1266.

34. Hockney RW, Eastwood JW. *Computer simulation using particles*. Taylor & Francis Group, 1988.

35. Torrie GM, Valleau JP. Nonphysical sampling distributions in Monte Carlo free-energy estimation: Umbrella sampling. *Journal of Computational Physics* 1977, 23(2): 187-199.

36. Im JK, Boateng LK, Flora JRV, Her N, Zoh KD, Son A, Yoon Y. Enhanced ultrasonic degradation of acetaminophen and naproxen in the presence of powdered activated carbon and biochar adsorbents. *Separation and Purification Technology* 2014, 123: 96-105.

37. Song Y-J, Wang M, Zhang X-Y, Wu J-Y, Zhang T. Investigation on the role of the molecular weight of polyvinyl pyrrolidone in the shape control of high-yield silver nanospheres and nanowires. *Nanoscale Research Letters* 2014, 9(1): 17.

38. Pandey G, Singh S, Hitkari G. Synthesis and characterization of polyvinyl pyrrolidone (PVP)-coated $Fe_3O_4$ nanoparticles by chemical co-precipitation method and removal of Congo red dye by adsorption process. *International Nano Letters* 2018, 8(2): 111-121.

39. Száraz I, Forsling W. PVP and azelaic acid adsorption on γ-alumina studied by FT-IR spectroscopy. *Vibrational Spectroscopy* 2002, 29(1): 15-20.

40. Borodko Y, Habas SE, Koebel M, Yang P, Frei H, Somorjai GA. Probing the Interaction of Poly(vinylpyrrolidone) with Platinum Nanocrystals by UV−Raman and FTIR. *The Journal of Physical Chemistry B* 2006, 110(46): 23052-23059.

41. Luo Y-R. *Comprehensive handbook of chemical bond energies*. CRC press, 2007.

42. Song JE, Phenrat T, Marinakos S, Xiao Y, Liu J, Wiesner MR, Tilton RD, Lowry GV. Hydrophobic Interactions Increase Attachment of Gum Arabic- and PVP-Coated Ag Nanoparticles to Hydrophobic Surfaces. *Environmental Science & Technology* 2011, 45(14): 5988-5995.

43. Jackson tA. Humic matter in natural waters and sediments. *Soil Science* 1975, 119(1): 56-64.

44. Jayalath S, Larsen SC, Grassian VH. Surface adsorption of Nordic aquatic fulvic acid on amine-functionalized and non-functionalized mesoporous silica nanoparticles. *Environmental Science: Nano* 2018, 5(9): 2162-2171.

45. Wu H, Gonzalez-Pech NI, Grassian VH. Displacement reactions between environmentally and biologically relevant ligands on $TiO_2$ nanoparticles: insights into the aging of nanoparticles in the environment. *Environmental Science: Nano* 2019.

46. Jayalath S, Wu H, Larsen SC, Grassian VH. Surface Adsorption of Suwannee River Humic Acid on $TiO_2$ Nanoparticles: A Study of pH and Particle Size. *Langmuir* 2018, 34(9): 3136-3145.

47. Gu B, Schmitt J, Chen Z, Liang L, McCarthy JF. Adsorption and desorption of natural organic matter on iron oxide: mechanisms and models. *Environmental Science & Technology* 1994, 28(1): 38-46.

48. Dobson KD, McQuillan AJ. In situ infrared spectroscopic analysis of the adsorption of aliphatic carboxylic acids to $TiO_2$, $ZrO_2$, $Al_2O_3$, and $Ta_2O_5$ from aqueous solutions. *Spectrochimica Acta Part A: Molecular and Biomolecular Spectroscopy* 1999, 55(7): 1395-1405.

49. Dobson KD, McQuillan AJ. In situ infrared spectroscopic analysis of the adsorption of aromatic carboxylic acids to $TiO_2$, $ZrO_2$, $Al_2O_3$, and $Ta_2O_5$ from aqueous solutions. *Spectrochimica Acta Part A: Molecular and Biomolecular Spectroscopy* 2000, 56(3): 557-565.

50. Petrov AA, Shtof IK. Investigation of structure of crude oil emulsion stabilizers by means of infrared spectroscopy. *Chemistry and Technology of Fuels and Oils* 1974, 10(8): 654-657.

# Chapter 5 Impact of Surface Adsorbed Biologically and Environmentally Relevant Ligands on $TiO_2$ Nanoparticle Reactivity

## 5.1 Abstract

Several studies have shown that environmentally and biologically relevant coatings on nanoparticle (NP) surfaces can significantly alter the physicochemical properties (e.g. dissolution and aggregation) of particles yet there remain some questions on how these coatings impact reactivity. In this study, we investigated the molecular-level details of surface adsorption and surface reactivity of $TiO_2$ NPs using *in-situ* Attenuated Total Reflectance–Fourier Transform Infrared spectroscopy (ATR–FTIR) in the presence of bovine serum albumin (BSA) protein and fulvic acid (FA), which are selected as representative biologically and environmentally relevant molecules. Our results show that both BSA and FA adsorb strongly onto $TiO_2$ NP surfaces at neutral pH. However, the photochemical behavior of $TiO_2$ with these two adsorbed coatings show large differences compared to bare $TiO_2$ and differences between each other. In the absence of any coatings, the photooxidation of solution phase benzoate by to hydroxyl benzoate as the major product is observed yet this reaction is completely inhibited when $TiO_2$ is coated with BSA and partially inhibited when $TiO_2$ is coated with FA. Additionally, we find that BSA can strongly scavenge ROS generated under irradiation by quenching the formation of electron-hole pairs. In contrast, FA behavior shows photoinduced hydrophilicity of the $TiO_2$ coated surface and the generation of ROS. These differences are attributed to the stronger interaction of BSA with the surface compared to FA. This study provides important insights into the impacts of environmentally and biologically relevant coatings and how they may modify the reactivity of the NPs in the environment.

## 5.2 Introduction

Due to the abundant use of NPs utilized in industry, large quantities of these NPs can end up being released into the environment as a pollutant.[1] Metal oxide nanoparticles (NPs) have been used in consumer products on a large scale. Previous research has indicated that released metal oxide NPs may exhibit some toxicity.[2, 3] With the increased use of metal oxide NPs, concerns about the safety and toxicity of nanomaterials have arisen. $TiO_2$ NPs are one of the most widely used in consumer products[4] due to their unique properties,[5, 6] high biocompatibility, and high abundance.[7-10] Yet there remains some questions about the potential harm of $TiO_2$ NPs to both the environment and to biological organisms as such there has been interest in the fate and reactivity of $TiO_2$ NPs.[11-14]

As a chemically stable material, the toxicity of $TiO_2$ NPs is primarily caused by reactive oxygen species (ROS) generated at the surface by photochemical processes.[11, 15] However, the reactivity of $TiO_2$ NPs can be altered in the presence of surface coatings.[16-19] For $TiO_2$ NPs released in the environment, these NPs can undergo different surface transformation processes such as adsorption, desorption and displacement.[20, 21] For example, the adsorption of natural organic matter (NOM) onto released $TiO_2$ NPs can impact their physiochemical properties including agglomeration, stability and mobility.[22-27] Fulvic acid (FA) is a representative molecule for NOM due to its high solubility at all pH values and wide distribution in soil, sediments, and water in the environment.[28-30] FA represents a family of natural compounds derived from the decomposition of plants and animals. Previous studies have shown that the interaction of FA with nanomaterial surfaces can involve strong chemical bonds, Van der Waals interactions and/or electrostatic interactions depending on the nature of the surface, solution phase pH and ionic strength.[31] Among the different interaction mechanisms by which NOM adsorbs onto NP surfaces, the dominant

interaction is surface ligand exchange between the NP surface and functional groups on the surface which can result in irreversible adsorption leaving a strongly adsorbed coating on the surface.[32] In addition to NOM coatings, biologically relevant molecules found in the environment can also adsorb onto NP surfaces. These biological molecules include proteins and peptides.[21, 33, 34] Among the numerous types of proteins, BSA is used as a model protein for serum albumin.[35] Adsorbed proteins can impact he properties of NPs (including aggregation, dissolution, reactivity and toxicity).[36] Thus, it is clear that the role surface coatings of environmentally and biologically relevant ligands play are key to understanding NPs in the environment. [37-39]

The reactivity of $TiO_2$ NPs involves the generation of reactive oxygen species (ROS) including hydroxyl radical ($OH^{\bullet}$), superoxide ($O_2^{\bullet -}$), and hydrogen peroxide ($H_2O_2$).[40] Different reactions to form these species are represented in Equations 1-8 below:

$$\mathbf{TiO_2} + \boldsymbol{h\nu} \rightarrow \mathbf{h}^{+}_{\boldsymbol{vb}} + \mathbf{e}^{-}_{\boldsymbol{vb}} \qquad (\mathbf{5.1})$$

$$\mathbf{h}^{+}_{\boldsymbol{vb}} + \mathbf{H_2O} \rightarrow \mathbf{OH^{\bullet}} + \mathbf{H^{+}} \qquad (\mathbf{5.2})$$

$$\mathbf{e}^{-}_{\boldsymbol{vb}} + \mathbf{O_2} \rightarrow \mathbf{O_2^{-\bullet}} \qquad (\mathbf{5.3})$$

$$\mathbf{H_2O} \rightarrow \mathbf{H^{+}} + \mathbf{OH^{-}} \qquad (\mathbf{5.4})$$

$$\mathbf{2OH^{\bullet}} \rightarrow \mathbf{H_2O_2} \qquad (\mathbf{5.5})$$

$$\mathbf{O_2^{-\bullet}} + \mathbf{H^{+}} \rightarrow \mathbf{HO_2^{\bullet}} \qquad (\mathbf{5.6})$$

$$\mathbf{HO_2^{\bullet}} + \mathbf{H^{+}} \rightarrow \mathbf{H_2O_2} \qquad (\mathbf{5.7})$$

$$\mathbf{H_2O_2} + \mathbf{e}^{-}_{\boldsymbol{vb}} \rightarrow \mathbf{OH^{\bullet}} + \mathbf{OH^{-}} \qquad (\mathbf{5.8})$$

$TiO_2$ NPs first form $e^-/h^+$ pairs, i.e. the formation of a hole and an excited electron by absorbing photons above the bandgap (Step (1)). As seen in the mechanism, water is oxidized to hydroxyl radicals as shown in Step (2). Hydroxyl radicals can interact to form hydrogen peroxide (Step (5)). Through a series of steps (Steps (3), (4) and (6)) oxygen in the system is reduced to superoxide which can then react with protons resulting in the generation of hydrogen peroxide (Step (7)). Additionally, hydrogen peroxide can be reduced to hydroxyl radical and hydroxide ion (Step (8)).

These ROS are mainly responsible for the photocatalytic properties of $TiO_2$ NPs in different applications including dye degradation.[41-45] These reactions can also cause phototoxcity to organisms in the enviroment.[11, 12, 46, 47] How surface coatings play a crucial role in the formation of ROS is important to understand. A previous study by Long *et al.* suggests that NOM coatings (such as humic acid, HA) on $TiO_2$ NPs can serve as a scavenger to quench holes, consequently weakening the capability of these NPs for the photochemical degradation of phenol.[48] In addition, a study focused on the denaturation of adsorbed proteins indicates that the protein corona, to some degree, prevents phototoxicity.[33, 49] However, these studies have not been able to reveal the detailed molecular based mechanisms occur on the surface.

Herein, we employed the use of mass spectrometry and ATR–FTIR spectroscopy to further explore photochemical reactions *in-situ*. ATR–FTIR spectroscopy is a technique that allows for *in-situ* monitoring of adsorbed species and chemical processes by measuring spectral changes of specific functional groups. Although the adsorption of ligands on nanomaterials has been extensively studied by ATR–FTIR spectroscopy,[20, 50-54] there are few reports about the mechanisms and roles of environmentally and biologically relevant coatings in reactions and their impact on the photoactivity of $TiO_2$ NPs in the environment.

## 5.3 Experimental Methods

### 5.3.1 Materials

$TiO_2$ NPs were purchased from Aldrich (vendor reported size 21nm, ≥99.5%). Solutions of sodium benzoate (BA, ≥99.5%, Sigma-Aldrich), Suwannee River fulvic acid (FA, International Humic Substances Society, Minneapolis, MN) and bovine serum albumin (BSA, ≥ 98%, Sigma-Aldrich) were prepared to maintain a stable pH of 7 for all experiments.. Sodium hydroxide (NaOH, 1N; Fisher Scientific) and hydrochloric acid (HCl, 1N; Fisher Scientific) were used to adjust pH. All the solutions were prepared with Milli-Q water.

### 5.3.2 ATR–FTIR Spectroscopy

ATR–FTIR spectra were recorded using a 500 μL horizontal ATR flow cell with an AMTIR window (Pike Technologies Inc.) in a Nicolet iS 10 FTIR Spectrometer equipped with an MCT–A detector. Spectra were collected with 264 scans at 4 $cm^{-1}$ resolution in the AMTIR window range (4000 – 750 $cm^{-1}$). The $TiO_2$ NP thin film was prepared by drying 1 mL of 1g/L $TiO_2$ in Milli–Q water on the AMTIR crystal in a dry air flow overnight. For adsorption, 0.5 g/L BSA, and 0.1 g/L fulvic acid solutions were used to fully cover the $TiO_2$ NP surface. The solution of BSA or FA was flowed over a $TiO_2$ NP film for two hours at a fixed flow rate (~0.4 mL/min) to cover the $TiO_2$ surface (adsorption step). *In-situ* photochemical reactions followed three sequential steps: (1) adsorption of BSA or FA, (2) introduction of sodium benzoate, (3) exposure to broadband irradiation. For the IR time course measurements, spectra were collected at an interval of 5 min. An LCS–100 solar simulator (model 94011A, Oriel, Newport) equipped with an AM1.5G filter and water filter is used to irradiate the sample.

For experiments with sodium benzoate, 10 mM sodium benzoate solution was introduced into the ATR cell with the $TiO_2$ NP film for two hours to equilibrate in the dark prior to exposure to light.

### 5.3.3 Batch Reactor Photochemical Experiments

$TiO_2$ NP powder was first mixed with 0.1 mg $ml^{-1}$ FA or 0.5 mg $ml^{-1}$ BSA solution to coat the surface with a loading amount of 2 g $L^{-1}$ for 12 hrs. The coated $TiO_2$ NPs were then separated from the suspension by centrifuging for 10 mins at 10,000 rpm. The precipitate was washed with water to remove any excessive solution remaining on the surface. The samples were transferred to a vacuum desiccator to dry, then ca. 20 mg of coated $TiO_2$ powder was added to a 20 mL glass vial with 10 mL of 2 mM BA solution. The vial was covered with foil and transferred into a bath sonicator to sonicate for 10 mins. The well-mixed suspensions were then exposed to light generated by a solar simulator with vigorous stirring for 6 h. After reaction, the suspensions were transferred to 15 mL centrifuge tubes and centrifuged for 10 mins at 10,000 rpm. The resulting supernatant was filtered through an MCE membrane (Millex–GS, 0.22 um) and kept refrigerated for further mass spectrometric analysis.

### 5.3.4 Mass Spectrometry Analyses of Photooxidation Products

The supernatant collected from the batch reactor were analyzed by a high-resolution hybrid linear ion trap mass spectrometer equipped with a heated electrospray ionization source (HESI–HRMS, Thermo Orbitrap Elite) using direct infusion mode. Prior to experiments, the samples were diluted by a factor of 10 with acetonitrile. Data were collected in negative ionization mode over the mass range of 50–2000 Da, with the spray voltage set at 2.60 kV, capillary temperature at 325 °C and S-lens at 60%.

## 5.4 Results and Discussion

5.4.1 ATR–FTIR Spectroscopy of BSA and FA Adsorption on TiO2 NPs

ATR–FTIR spectroscopy was employed to study ligand adsorption and photochemical reactions of ligands on $TiO_2$ NPs as well as the photochemical oxidation of BA on $TiO_2$ NPs with coatings at pH 7. As shown in Figure 5.1, ATR–FTIR spectra are recorded as a function of time in the presence of BSA and FA, in 5.1(a) and 5.1(b), respectively, on a $TiO_2$ surface. These spectra were referenced to a water-$TiO_2$ film at the same pH. As can be seen in the spectra, there is an increase in intensity of several peaks in the spectral range extending from 900 to 2000 $cm^{-1}$ as a function of time. The peak assignments for BSA and FA have been made previously and these are listed in Table 5.1. For the adsorbed BSA spectra (Figure 5.1a), the amide I band appears at 1651

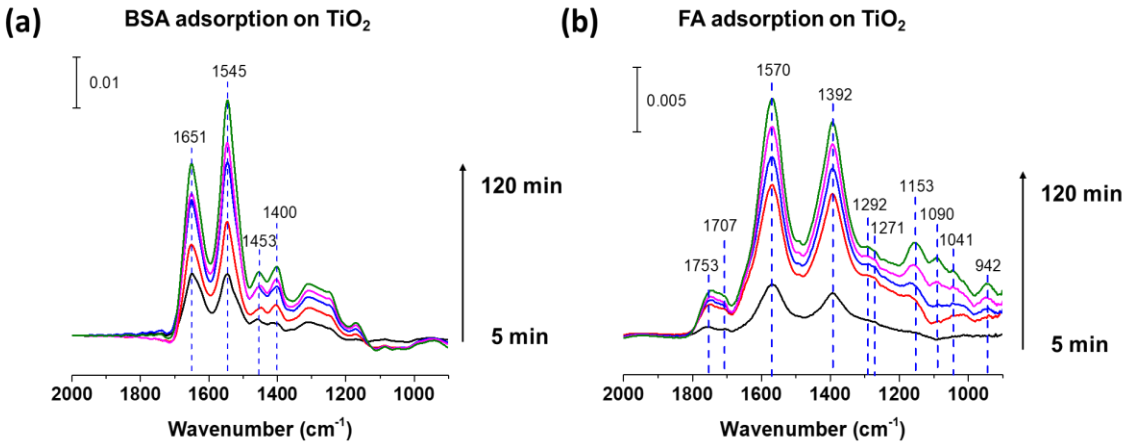


**Figure 5.1** ATR–FTIR spectra of the molecular adsorption on $TiO_2$ NP film, (a) 0.5 mg/ml BSA, (b) 0.1 mg/ml FA, respectively, as a function of time. The adsorption spectra shown were collected at 5 min (black), 30 min (red), 60 min (blue), 90 (magenta), 120 min (green).

$cm^{-1}$.[55] The N–H bending and C–N stretching of the amide II band appears at a vibrational frequency around 1545 $cm^{-1}$. The other two absorption features at 1453 and 1400 $cm^{-1}$ are due to C–H bending and the amide III band, respectively. For FA adsorption, there are multiple functional groups of FA involved in the interaction with $TiO_2$ including: carbonyls, amides, carboxylates, phenols, polysaccharides, and alcohol hydroxyls.[20, 56] In the adsorbed FA spectra (Figure 5.1b), the dominant absorption bands correspond to the asymmetric and symmetric carboxylate

vibrations appear at 1570 and 1392 $cm^{-1}$, respectively. In addition to the strong asymmetric and symmetric vibrations of carboxylate, the absorption band at 1292 $cm^{-1}$ is assigned to the bending

**Table** 5.1 Assignment of the vibrational frequencies ($cm^{-1}$)

| Biological and/or Chemical Species | Vibrational Mode | Adsorbed Species [this work ($cm^{-1}$)] | Literature ($cm^{-1}$) [21, 29, 52, 57-61] |
|---|---|---|---|
| BSA | amide I | 1651 | 1695 – 1630 |
| | amide II | 1545 | 1550 |
| | δ (C-H) | 1453 | 1500-1400 |
| | amide III and/or υ (C-O)/ υ (C-O-C)/ υ (C-C) | 1400 | 1400 – 1000 |
| FA | υ (C=O) | 1753,1707 | 1720, 1640 |
| | $\upsilon_{asym}$ ($COO^-$) | 1570 | 1590 – 1550 |
| | δ (C-H) | 1451 | 1450 |
| | $\upsilon_{sym}$(COO-)/OH def | 1392 | 1350 |
| | δ (O-C=O) | 1292 | 1292 |
| | υ (phenol C-OH) | 1271 | 1270 |
| | υ (C-C, C-O) | 1153, 1090, 1041, 942 | 1200 –1000 |
| Benzoate | υ (C=C) | 1600, 1557, 1497 | 1660 – 1450 |
| | $\upsilon_{sym}$(COO-)/OH def | 1391 | 1400 – 1391 |
| | δ (C-H) | 1434 | 1450 |

of the –COO–Ti groups.[20, 21] All of these vibrational bands indicate that FA primarily binds to the $TiO_2$ NP surface via the carboxylate group. Other characteristic absorption bands include C=O stretching at 1753 and 1707 $cm^{-1}$.

### 5.4.2 ATR–FTIR Spectra Monitoring Photochemical Processes on $TiO_2$ NPs

Figure 5.2 shows ATR–FTIR spectra of pure water on a $TiO_2$ NP film as a function of time. The water bending mode can be seen at 1636 $cm^{-1}$ and the increase of this peak suggests water adsorption upon irradiation, indicating photoinduced superhydrophilicity on $TiO_2$ NPs.[62] It should note that the region below 1200 $cm^{-1}$ also grows with irradiation. The prominent peaks located at 1100 and 1084 $cm^{-1}$ are attributed to adsorbed superoxide on the surface.[63-65] Another peak at 980 $cm^{-1}$ is possibly due to a terminal **Ti ≡ O** that is believed to be an intermediate state in photocatalytic processes.[66] Given the broad absorption below 900 $cm^{-1}$, it is likely that $H_2O_2$, which exhibits an IR vibrational frequency around 870 $cm^{-1}$, forms in addition to superoxide. Thus,

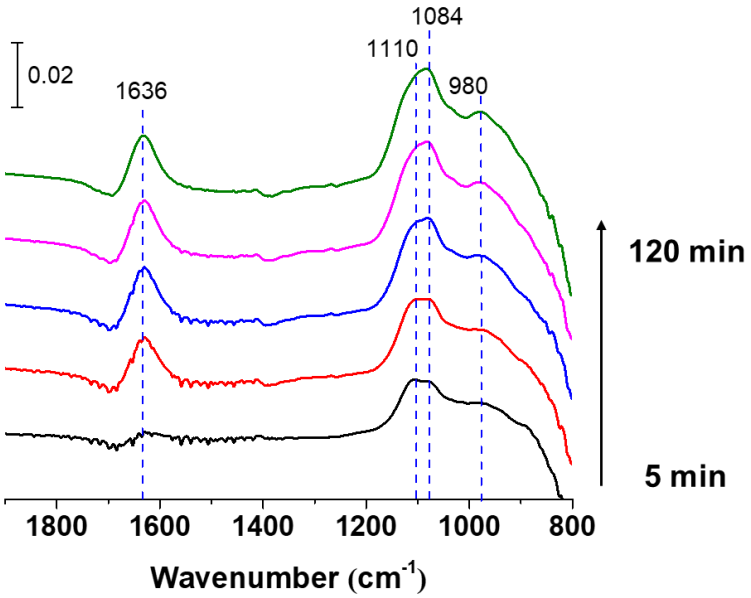


**Figure 5.2** ATR-FTIR spectra following broadband irradiation of pure water on TiO2 NPs. The spectra shown were collected at 5 min (black), 30 min (red), 60 min (blue), 90 min (magenta), 120 min (green) and are referenced to the initial dark spectrum of the H2O--$TiO_2$ film.

$TiO_2$ has a surface that is very reactive to the generation of ROS in water including $H_2O_2$ and superoxide radicals.

### 5.4.3 ATR–FTIR Spectra Monitoring Photochemical Processes of Coating Molecules on $TiO_2$ NPs

The photocatalytic behavior of $TiO_2$ coated by BSA and FA was investigated *in-situ* by ATR–FTIR. The corresponding solution remained above the film when irradiated with light. The resulting IR spectra are shown in Figure 5.3. As can be seen, the intensity of each spectrum increased with irradiation time due to background and $TiO_2$ surface changes induced by photons.[67, 68] No vibrational frequency shifts are seen for the major peaks of BSA (Figure 5.3a). Interestingly, a new peak at 1761 $cm^{-1}$ appears to grow at later irradiation times. Although this peak has not been reported in previous work,[33, 34] it is likely that this comes from photooxidation of BSA on the $TiO_2$ surface. It is also worth noting that the intensity of the amide I band at 1651 $cm^{-1}$ increases significantly with irradiation time. In previous studies, it has been suggested that this was caused by changes in secondary structure under irradiation.[33] As shown previously,[21] BSA has a strong binding affinity for the $TiO_2$ surface; therefore, the generated ROS or excited holes from $TiO_2$ may

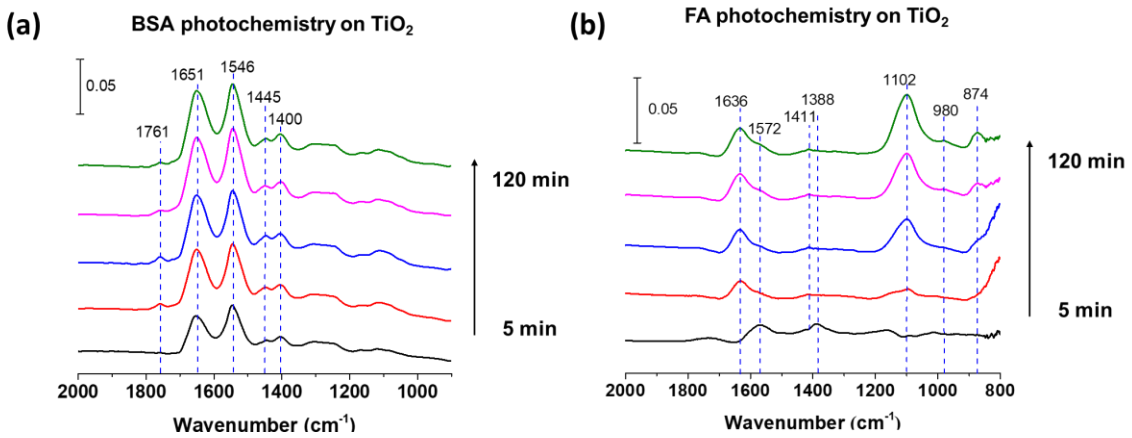


**Figure 5.3** ATR–FTIR spectra of photochemical process of coated $TiO_2$ NPs, (a) BSA coated $TiO_2$, (b) FA coated $TiO_2$. The spectra shown were collected at 5 min (black), 30 min (red), 60 min (blue), 90 (magenta), 120 min (green).

first react with the adsorbed BSA molecules, which shows spectral changes of BSA induced by irradiation.

Adsorbed FA is also able to quench the generation of trapped holes so that the production of $OH^{\bullet}$ is inhibited but to a much lesser extent.[30, 37, 69, 70] In contrast to BSA coated $TiO_2$ NPs, the spectra of adsorbed FA under irradiation change dramatically with time (Figure 5.3b). The first spectrum, collected at 5 min after irradiation, shows the characteristic vibrations of adsorbed FA on $TiO_2$ NPs which include the asymmetric and symmetric vibrations of $COO^-$ at 1572 and 1388 $cm^{-1}$, respectively. As irradiation time increases, the symmetric peak shifts to 1411 $cm^{-1}$ after 30 min, while the asymmetric peak does not change vibrational frequency but instead merges with a peak at 1636 $cm^{-1}$ that is adsorbed water on the $TiO_2$ surface. It is plausible that the adsorbed molecules change their binding modes upon irradiation due to $TiO_2$ surface changes[71] and photo-degradation.[72, 73] It is worth noting the three new peaks in the low vibrational frequency range below 1200 $cm^{-1}$ (1102, 980, and 874 $cm^{-1}$) are likely from surface ROS intermediates generated by irradiation. The peak at 874 $cm^{-1}$ is assigned to hydrogen peroxide (reported IR frequency for hydrogen peroxide is 877 $cm^{-1}$).[74] The other two peaks at 1102 and 980 $cm^{-1}$ are possibly from an adsorbed superoxide intermediate with $Ti^{4+}$ and **Ti ≡ O**,respectively.[65, 66] Therefore, these peaks provide evidence for the formation of ROS on the FA-$TiO_2$ coated surface. FA also has a high degree of conjugation in its structure with the presence of aromatics and olefinic groups, this can enable an electron transfer pathway, which helps to enhance oxygen reduction.[75] The photoinduced surface change affects the binding mode of FA on the $TiO_2$ surface and can give rise to surface regions whereby water can adsorb on the surface. This can be seen in the IR spectra, where

photoinduced water adsorption and oxygen reduction products such as superoxide and hydrogen peroxide were observed.

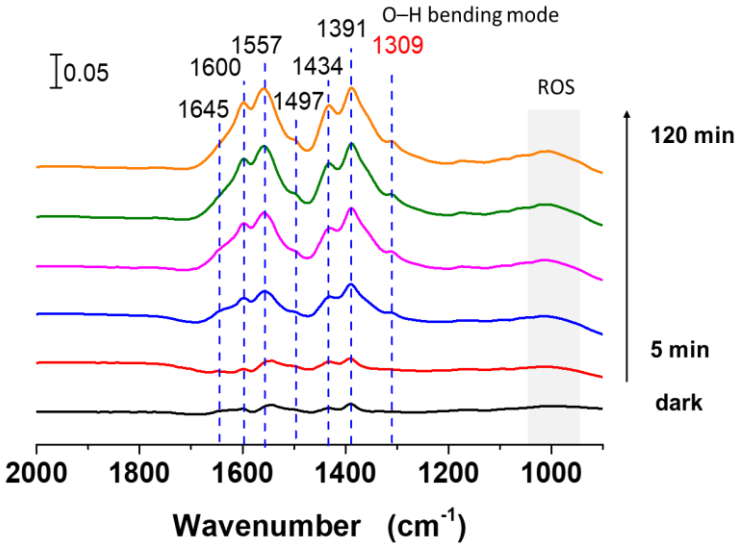


**Figure 5.4** ATR-FTIR spectra of the photochemical process of 10 mM sodium benzoate on $TiO_2$ NPs. The spectra shown were collected at initial spectrum in the dark (black), 5 min (red), 30 min (blue), 60 min (magenta), 90 min (green), 120 min (orange).

5.4.4 ATR–FTIR Spectra Monitoring Photochemical Processes of BA on $TiO_2$ NPs.

Hydroxyl groups are hard to detect in solution and here we use sodium benzoate as a probe molecule since benzoate can react with hydroxyl radicals to produce a series of product compounds. Sodium benzoate in solution was introduced into the ATR cell over coated and uncoated $TiO_2$ films in the dark. The photochemical reaction for benzoate solution on bare $TiO_2$ NPs was first investigated and the spectra are shown in Figure 5.4. The first spectrum was collected without light irradiation (initial solution). The characteristic peaks of benzoate are located in the region from 1600 to 1391 $cm^{-1}$: they are primarily from the symmetric stretching vibration of carboxylate (1391 $cm^{-1}$), bending of C–H (1434 $cm^{-1}$) and the breathing modes of the benzene ring (1600, 1557, and 1497 $cm^{-1}$).[61] The asymmetric stretching of carboxylate is likely overlapping with these peaks. The peak at 1645 $cm^{-1}$ is attributed to the bending mode of adsorbed water on the $TiO_2$ surface. As seen in Figure 5.4, the intensity of the peaks increases with irradiation time. It is

interesting that a new shoulder peak at 1309 $cm^{-1}$ appears after irradiation, which is close to the bending mode of O–H in hydroxyl benzoate.[76, 77] This suggests that benzoate on bare $TiO_2$ is oxidized to hydroxyl benzoate. In order to confirm this, mass spectrometry was used. Figure 5.5a shows the mass spectra of benzoic acid when reacted with bare $TiO_2$ NPs under irradiation

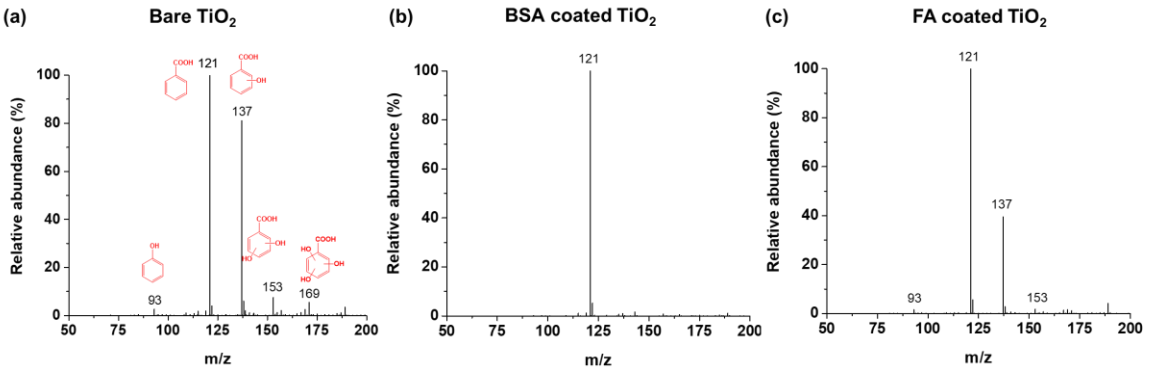


**Figure 5.5** Mass spectra of benzoate reacted with (a) bare $TiO_2$, (b) BSA-coated $TiO_2$ and (c) FA-coated $TiO_2$.

conditions. A pronounced peak at *m/z* 137, with the formula of $C_7H_5O_3^-$, dominates the spectrum of benzoic acid reacted with bare $TiO_2$. Additionally, m/z 93 ($C_6H_5O^-$), 153 ($C_7H_5O_4^-$), and 169 ($C_7H_5O_5^-$) are also observed. Figure 5.6 displays a plausible mechanism for the formation of these products. It is well known that ROS such as hydroxyl radical can be generated on the $TiO_2$ surface under UV conditions.[40] Therefore, the formation of these products may arise from the oxidation of BA by the generated hydroxyl radicals. The reaction of BA with hydroxyl radicals is initiated via an electron transfer step that generates a carboxyphenyl radical intermediate. This radical can react with $H_2O$ to form hydroxyl benzoic acid (m/z 137) or undergo decarboxylation to produce a phenyl radical resulting in the formation of phenol (m/z 93). Upon further oxidation, the carboxyphenyl

radical intermediate can also be converted to dihydroxy (m/z 153) and trihydroxy benzoic acid (m/z 169), in addition to other products.

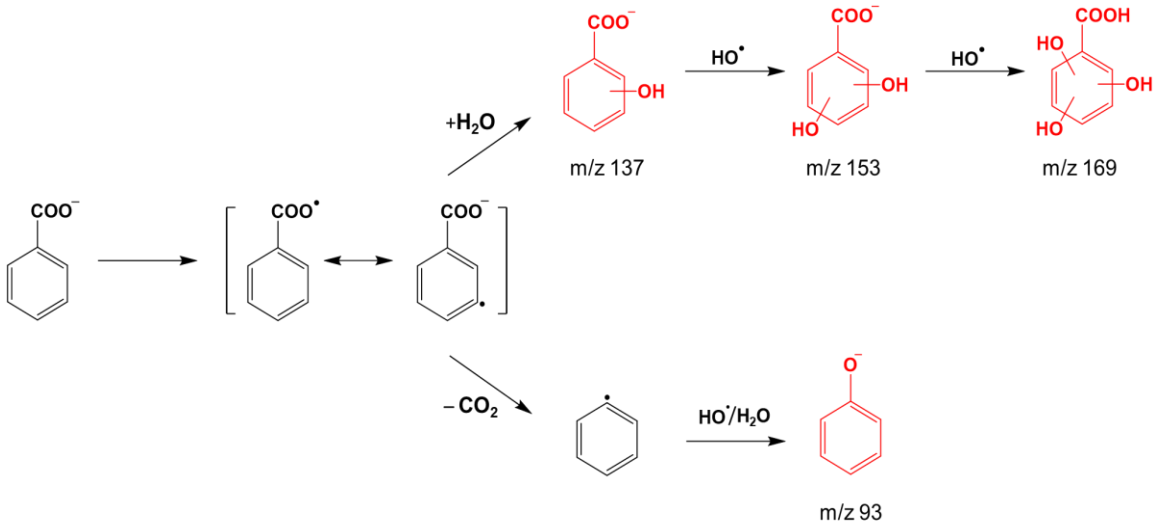


**Figure 5.6** The proposed pathway of benzoate oxidation

In order to understand the effects of coating molecules on photochemical processes in the presence of BA, BA solutions were first introduced onto BSA- or FA-coated NP films in the dark. The ATR–FTIR dark spectra are provided in supporting information (Figure C1), i.e. the adsorption of BA on pre-coated NPs. All spectra preserve the initial IR characteristic absorptions. It is clear that there are no observed peak shifts due to displacement reactions by BA. Therefore, these data suggest that BA in this process interacts with the surface coatings and not directly with the $TiO_2$ surface. Benzoic acid has been reported to interact with tryptophan residues in BSA via Van der Waals forces and electrostatic interactions with the positively charged amino acid.[78, 79] Compared to BSA-only coated spectra, the peak at 1761 $cm^{-1}$ is weaker in presence of benzoate (Figure 5.7a). Additionally, a peak at 1100 $cm^{-1}$ is seen following irradiation which may be due to benzoate. Overall, BSA coating strongly inhibits the oxidation of benzoate by hydroxyl radicals. When the FA-coated surface was exposed to the benzoate solution as shown in Figure 5.7b, the first spectrum closely resembles that of the FA-only coated surface spectra, which suggests again

that benzoate has little interaction with the $TiO_2$ surface. The possible surface ROS intermediates generated by irradiation appear in the same range as discussed in the case of FA-only coated surface. There are, however, some small spectral differences from the presence of benzoate. A new peak at 1268 $cm^{-1}$ is observed in the spectra, which is possibly from the O–H stretching mode in hydroxybenzoic acid.[76] These new peaks suggest that benzoate is oxidized to hydroxybenzoate on the FA coated surface.

The mass spectrometry data further corroborates the results of ATR–FTIR discussed above.

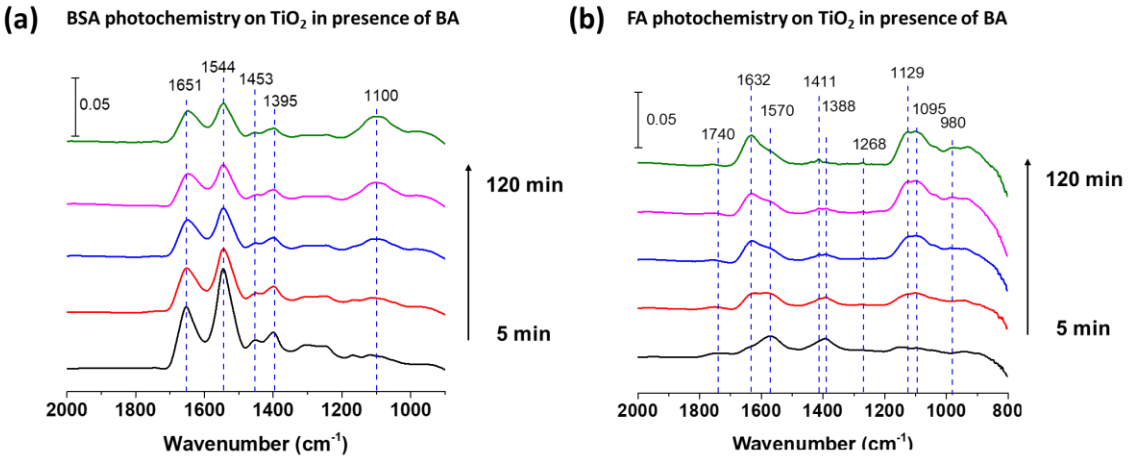


**Figure 5.7** ATR-FTIR spectra of photochemical process of coated $TiO_2$ NPs in presence of 2 mM sodium benzoate, (a) BSA coated $TiO_2$, (b) FA coated $TiO_2$. The spectra shown were collected at 5 min (black), 30 min (red), 60 min (blue), 90 (magenta), 120 min (green).

As shown in Figure 5.5b, there is only one pronounced peak for benzoate at *m/z* 121 on BSA coated surface. However, m/z 93 ($C_6H_5O^-$), and 153 ($C_7H_5O_4^-$) are also observed on FA coated surface (Figure 5.5c) in addition to the dominant peak at *m/z* 137 for hydroxybenzoate. The products for FA coated $TiO_2$ are less than that of bare $TiO_2$, indicating that FA prohibits $OH^{\bullet}$ production. Moreover, these peaks disappear in the reaction of BA with BSA-coated $TiO_2$, suggesting that BSA has a much stronger inhibition effect on the production of hydroxyl radicals than FA.

## 5.5 Conclusions

BSA and FA, as representative ligands of biological and environmental significance, were chosen to study their effects on the generation of ROS under irradiation of $TiO_2$ nanoparticles through *in-situ* ATR–FTIR and mass spectrometry. The photochemical *in-situ* IR measurements on bare $TiO_2$ NPs exhibit generation of ROS on NP surface. However, ROS were not observed on BSA coated NP surfaces. Although, BSA was exhibited some evidence of oxidation. In contrast to BSA, ROS is observed to be generated on FA coated $TiO_2$ NP surfaces and FA binding modes are suspected to change caused by photoinduced surface changes. Based on our study, the interaction between coating molecules and surfaces of nanomaterials show significant impacts on the generation of ROS and holes which are highly relevant to the reactivity of $TiO_2$ NPs. Upon further study, benzoate could be used to detect OH radicals that are not visible in IR spectra. Benzoate does not show the sign of oxidation on BSA coated surface, but it is oxidized on FA coated surface under irradiation. Along with these *in-situ* spectroscopic measurements, mass spectrometry is also utilized to analyze the products on these three surfaces i.e. bare, BSA coated and FA coated surface. These results indicate that the presence of benzoate alters the interaction of BSA with $TiO_2$ surfaces with other amino residues instead of the one without benzoate, thus prohibiting oxidation of benzoate by hydroxyl radicals. Interestingly benzoate can partially react with ROS on FA-coated $TiO_2$ NPs. Therefore, the ability for ROS generation on $TiO_2$ NPs with different coatings follows this sequence: bare $TiO_2$ > FA–$TiO_2$ > BSA–$TiO_2$. This study shows the importance of biological and environmental ligands on modulating the reactivity of $TiO_2$ nanoparticles in the environment.

## 5.6 Acknowledgements

This work is supported by the National Science Foundation under grant number CHE1606607. Any opinions, findings, and conclusions or recommendations expressed in this

material are those of the authors and do not necessarily reflect the views of the National Science Foundation.

Chapter 5 is in preparation for submission: Haibin Wu, Liubin Huang, Amber Rose, Vicki H. Grassian. “Impact of Surface Adsorbed Biologically and Environmentally Relevant Ligands on $TiO_2$ Nanoparticle Reactivity”.

5.7 References


1. Garner KL, Suh S, Keller AA. Assessing the risk of engineered nanomaterials in the environment: development and application of the nanofate model. *Environmental Science & Technology* 2017, 51(10): 5541-5551.

2. Wongrakpanich A, Mudunkotuwa IA, Geary SM, Morris AS, Mapuskar KA, Spitz DR, Grassian VH, Salem AK. Size-dependent cytotoxicity of copper oxide nanoparticles in lung epithelial cells. *Environmental Science: Nano* 2016, 3(2): 365-374.

3. Brunner TJ, Wick P, Manser P, Spohn P, Grass RN, Limbach LK, Bruinink A, Stark WJ. In vitro cytotoxicity of oxide nanoparticles: comparison to asbestos, silica, and the effect of particle solubility. *Environmental Science & Technology* 2006, 40(14): 4374-4381.

4. Smijs TG, Pavel S. Titanium dioxide and zinc oxide nanoparticles in sunscreens: focus on their safety and effectiveness. *Nanotechnology, science and applications* 2011, 4: 95-112.

5. Daghrir R, Drogui P, Robert D. Modified $TiO_2$ for environmental photocatalytic applications: a review. *Industrial & Engineering Chemistry Research* 2013, 52(10): 3581-3599.

6. Wang Y, Wang Q, Zhan X, Wang F, Safdar M, He J. Visible light driven type II heterostructures and their enhanced photocatalysis properties: a review. *Nanoscale* 2013, 5(18): 8326-8339.

7. Li Z, Yang R, Yu M, Bai F, Li C, Wang ZL. Cellular level biocompatibility and biosafety of ZnO nanowires. *The Journal of Physical Chemistry C* 2008, 112(51): 20114-20117.

8. Ji Z, Jin X, George S, Xia T, Meng H, Wang X, Suarez E, Zhang H, Hoek EMV, Godwin H, Nel AE, Zink JI. Dispersion and stability optimization of $TiO_2$ nanoparticles in cell culture media. *Environmental Science & Technology* 2010, 44(19): 7309-7314.

9. Ramani M, Mudge MC, Morris RT, Zhang Y, Warcholek SA, Hurst MN, Riviere JE, DeLong RK. Zinc oxide nanoparticle-poly i:C RNA complexes: implication as therapeutics against experimental melanoma. *Mol Pharm* 2017, 14(3): 614-625.

10. Singh S, D'Britto V, Bharde A, Sastry M, Dhawan A, Prasad BLV. Bacterial synthesis of photocatalytically active and biocompatible $TiO_2$ and ZnO nanoparticles. *International Journal of Green Nanotechnology: Physics and Chemistry* 2010, 2(2): 80-99.

11. Tong T, Shereef A, Wu J, Binh CTT, Kelly JJ, Gaillard J-F, Gray KA. Effects of material morphology on the phototoxicity of nano-$TiO_2$ to bacteria. *Environmental Science & Technology* 2013, 47(21): 12486-12495.

12. Zhu X, Zhou J, Cai Z. $TiO_2$ nanoparticles in the marine environment: impact on the toxicity of tributyltin to abalone (haliotis diversicolor supertexta) embryos. *Environmental Science & Technology* 2011, 45(8): 3753-3758.

13. Simonin M, Richaume A, Guyonnet JP, Dubost A, Martins JMF, Pommier T. Titanium dioxide nanoparticles strongly impact soil microbial function by affecting archaeal nitrifiers. *Scientific Reports* 2016, 6(1): 33643.

14. Shakiba S, Hakimian A, Barco LR, Louie SM. Dynamic intermolecular interactions control adsorption from mixtures of natural organic matter and protein onto titanium dioxide nanoparticles. *Environmental Science & Technology* 2018, 52(24): 14158-14168.

15. Liu N, Chang Y, Feng Y, Cheng Y, Sun X, Jian H, Feng Y, Li X, Zhang H. {101}–{001} surface heterojunction-enhanced antibacterial activity of titanium dioxide nanocrystals under sunlight irradiation. *ACS Applied Materials & Interfaces* 2017, 9(7): 5907-5915.

16. Zhou Z, Son J, Harper B, Zhou Z, Harper S. Influence of surface chemical properties on the toxicity of engineered zinc oxide nanoparticles to embryonic zebrafish. *Beilstein journal of nanotechnology* 2015, 6: 1568-1579.

17. Praetorius A, Scheringer M, Hungerbühler K. Development of environmental fate models for engineered nanoparticles—a case study of $TiO_2$ nanoparticles in the rhine river. *Environmental Science & Technology* 2012, 46(12): 6705-6713.

18. Labille J, Feng J, Botta C, Borschneck D, Sammut M, Cabie M, Auffan M, Rose J, Bottero J-Y. Aging of $TiO_2$ nanocomposites used in sunscreen. Dispersion and fate of the degradation products in aqueous environment. *Environmental Pollution* 2010, 158(12): 3482-3489.

19. van Ravenzwaay B, Landsiedel R, Fabian E, Burkhardt S, Strauss V, Ma-Hock L. Comparing fate and effects of three particles of different surface properties: nano-$TiO_2$, pigmentary $TiO_2$ and quartz. *Toxicology Letters* 2009, 186(3): 152-159.

20. Jayalath S, Wu H, Larsen SC, Grassian VH. Surface adsorption of suwannee river humic acid on $TiO_2$ nanoparticles: a study of pH and particle size. *Langmuir* 2018, 34(9): 3136-3145.

21. Wu H, Gonzalez-Pech NI, Grassian VH. Displacement reactions between environmentally and biologically relevant ligands on $TiO_2$ nanoparticles: insights into the aging of nanoparticles in the environment. *Environmental Science: Nano* 2019, 6(2): 489-504.

22. Gallego-Urrea JA, Perez Holmberg J, Hassellöv M. Influence of different types of natural organic matter on titania nanoparticle stability: effects of counter ion concentration and pH. *Environmental Science: Nano* 2014, 1(2): 181-189.

23. Loosli F, Le Coustumer P, Stoll S. Effect of natural organic matter on the disagglomeration of manufactured $TiO_2$ nanoparticles. *Environmental Science: Nano* 2014, 1(2): 154-160.

24. Domingos RF, Tufenkji N, Wilkinson KJ. Aggregation of titanium dioxide nanoparticles: role of a fulvic acid. *Environmental Science & Technology* 2009, 43(5): 1282-1286.

25. Domingos RF, Rafiei Z, Monteiro CE, Khan MAK, Wilkinson KJ. Agglomeration and dissolution of zinc oxide nanoparticles: role of pH, ionic strength and fulvic acid. *Environmental Chemistry* 2013, 10(4): 306-312.

26. Chen G, Liu X, Su C. Distinct effects of humic acid on transport and retention of $TiO_2$ rutile nanoparticles in saturated sand columns. *Environmental Science & Technology* 2012, 46(13): 7142-7150.

27. Chowdhury I, Cwiertny DM, Walker SL. Combined factors influencing the aggregation and deposition of nano-$TiO_2$ in the presence of humic acid and bacteria. *Environmental Science and Technology* 2012, 46(13): 6968-6976.

28. Yoon TH, Johnson SB, Brown GE. Adsorption of Suwannee river fulvic acid on aluminum oxyhydroxide surfaces: an in situ ATR–FTIR study. *Langmuir* 2004, 20(14): 5655-5658.

29. Baes AU, Bloom PR. Diffuse reflectance and transmission fourier transform infrared (DRIFT) spectroscopy of humic and fulvic acids. *Soil Science Society of America Journal* 1989, 53(3): 695-700.

30. Wu W, Shan G, Xiang Q, Zhang Y, Yi S, Zhu L. Effects of humic acids with different polarities on the photocatalytic activity of nano-$TiO_2$ at environment relevant concentration. *Water Research* 2013, 122: 78-85.

31. Philippe A, Schaumann GE. Interactions of dissolved organic matter with natural and engineered inorganic colloids: a review. *Environmental Science & Technology* 2014, 48(16): 8946-8962.

32. Yang K, Lin D, Xing B. Interactions of humic acid with nanosized inorganic oxides. *Langmuir* 2009, 25(6): 3571-3576.

33. Bouhekka A, Bürgi T. In situ ATR-IR spectroscopy study of adsorbed protein: visible light denaturation of bovine serum albumin on $TiO_2$. *Applied Surface Science* 2012, 261: 369-374.

34. Bouhekka A, Bürgi T. Photodegradation of adsorbed bovine serum albumin on $TiO_2$ anatase investigated by in-situ ATR-IR spectroscopy. *Acta Chim Slov* 2012, 59: 841–847.

35. Nasser F, Lynch I. Secreted protein eco-corona mediates uptake and impacts of polystyrene nanoparticles on Daphnia magna. *Journal of Proteomics* 2016, 137: 45-51.

36. Boehmler DJ, O'Dell ZJ, Chung C, Riley KR. Bovine serum albumin enhances silver nanoparticle dissolution kinetics in a size- and concentration-dependent manner. *Langmuir* 2020, 36(4): 1053-1061.

37. Long M, Brame J, Qin F, Bao J, Li Q, Alvarez PJJ. Phosphate changes effect of humic acids on $TiO_2$ photocatalysis: from inhibition to mitigation of electron–hole recombination. *Environmental Science & Technology* 2017, 51(1): 514-521.

38. Drosos M, Ren M, Frimmel FH. The effect of NOM to $TiO_2$: interactions and photocatalytic behavior. *Applied Catalysis B: Environmental* 2015, 165: 328-334.

39. Kim J, Doudrick K. Emerging investigator series: protein adsorption and transformation on catalytic and food-grade $TiO_2$ nanoparticles in the presence of dissolved organic carbon. *Environmental Science: Nano* 2019, 6(6): 1688-1703.

40. Nosaka Y, Nosaka AY. Generation and detection of reactive oxygen species in photocatalysis. *Chemical Reviews* 2017, 117(17): 11302-11336.

41. Deepagan VG, You DG, Um W, Ko H, Kwon S, Choi KY, Yi G-R, Lee JY, Lee DS, Kim K, Kwon IC, Park JH. Long-circulating Au-$TiO_2$ nanocomposite as a sonosensitizer for ROS-mediated eradication of cancer. *Nano Letters* 2016, 16(10): 6257-6264.

42. Liao Y, Brame J, Que W, Xiu Z, Xie H, Li Q, Fabian M, Alvarez PJ. Photocatalytic generation of multiple ROS types using low-temperature crystallized anodic $TiO_2$ nanotube arrays. *Journal of Hazardous materials* 2013, 260: 434-441.

43. Ma H-Y, Zhao L, Guo L-H, Zhang H, Chen F-J, Yu W-C. Roles of reactive oxygen species (ROS) in the photocatalytic degradation of pentachlorophenol and its main toxic intermediates by $TiO_2$/UV. *Journal of Hazardous materials* 2019, 369: 719-726.

44. V LP, Rajagopalan V. A new synergetic nanocomposite for dye degradation in dark and light. *Scientific Reports* 2016, 6(1): 38606.

45. Wang J, Guo Y, Liu B, Jin X, Liu L, Xu R, Kong Y, Wang B. Detection and analysis of reactive oxygen species (ROS) generated by nano-sized $TiO_2$ powder under ultrasonic irradiation and application in sonocatalytic degradation of organic dyes. *Ultrasonics Sonochemistry* 2011, 18(1): 177-183.

46. Ou Y, Lin J-D, Zou H-M, Liao D-W. Effects of surface modification of $TiO_2$ with ascorbic acid on photocatalytic decolorization of an azo dye reactions and mechanisms. *Journal of Molecular Catalysis A: Chemical* 2005, 241(1): 59-64.

47. Sakthivel S, Neppolian B, Shankar MV, Arabindoo B, Palanichamy M, Murugesan V. Solar photocatalytic degradation of azo dye: comparison of photocatalytic efficiency of ZnO and $TiO_2$. *Solar Energy Materials and Solar Cells* 2003, 77(1): 65-82.

48. Cho Y, Choi W. Visible light-induced reactions of humic acids on $TiO_2$. *Journal of Photochemistry and Photobiology A: Chemistry* 2002, 148(1): 129-135.

49. Garvas M, Testen A, Umek P, Gloter A, Koklic T, Strancar J. Protein corona prevents $TiO_2$ phototoxicity. *PLoS One* 2015, 10(6): e0129577.

50. Mudunkotuwa IA, Grassian VH. Biological and environmental media control oxide nanoparticle surface composition: the roles of biological components (proteins and amino acids), inorganic oxyanions and humic acid. *Environ Sci: Nano* 2015, 2(5): 429-439.

51. Mudunkotuwa IA, Minshid AA, Grassian VH. ATR–FTIR spectroscopy as a tool to probe surface adsorption on nanoparticles at the liquid-solid interface in environmentally and biologically relevant media. *Analyst* 2014, 139(5): 870-881.

52. Mudunkotuwa IA, Grassian VH. Citric acid adsorption on $TiO_2$ nanoparticles in aqueous suspensions at acidic and circumneutral pH: surface coverage, surface speciation, and its impact on nanoparticle−nanoparticle interactions. *Journal of the American Chemical Society* 2010, 132(42): 14986-14994.

53. Bian SW, Mudunkotuwa IA, Rupasinghe T, Grassian VH. Aggregation and dissolution of 4 nm ZnO nanoparticles in aqueous environments: influence of pH, ionic strength, size, and adsorption of humic acid. *Langmuir* 2011, 27(10): 6059-6068.

54. Mudunkotuwa IA, Rupasinghe T, Wu C-M, Grassian VH. Dissolution of ZnO nanoparticles at circumneutral pH: a study of size effects in the presence and absence of citric acid. *Langmuir* 2012, 28(1): 396-403.

55. Abrosimova KV, Shulenina OV, Paston SV. FTIR study of secondary structure of bovine serum albumin and ovalbumin. *Journal of Physics: Conference Series* 2016, 769(1): 012016.

56. Chen W, Qian C, Liu X, Yu H. Two-dimensional correlation spectroscopic analysis on the interaction between humic acids and $TiO_2$ nanoparticles. *Environmental Science & Technology* 2014, 48(19): 11119-11126.

57. Dobson KD, McQuillan AJ. In situ infrared spectroscopic analysis of the adsorption of aliphatic carboxylic acids to $TiO_2$, $ZrO_2$, $Al_2O_3$, and $Ta_2O_5$ from aqueous solutions. *Spectrochimica Acta Part A: Molecular and Biomolecular Spectroscopy* 1999, 55(7): 1395-1405.

58. Dobson KD, McQuillan AJ. In situ infrared spectroscopic analysis of the adsorption of aromatic carboxylic acids to $TiO_2$, $ZrO_2$, $Al_2O_3$, and $Ta_2O_5$ from aqueous solutions. *Spectrochimica Acta Part A: Molecular and Biomolecular Spectroscopy* 2000, 56(3): 557-565.

59. Márquez A, Berger T, Feinle A, Hüsing N, Himly M, Duschl A, Diwald O. Bovine serum albumin adsorption on $TiO_2$ colloids: the effect of particle agglomeration and surface composition. *Langmuir* 2017, 33(10): 2551-2558.

60. Grdadolnik J, Maréchal Y. Bovine serum albumin observed by infrared spectrometry. I. Methodology, structural investigation, and water uptake. *Biopolymers* 2001, 62(1): 40-53.

61. Buchholz M, Xu M, Noei H, Weidler P, Nefedov A, Fink K, Wang Y, Wöll C. Interaction of carboxylic acids with rutile $TiO_2$(110): IR-investigations of terephthalic and benzoic acid adsorbed on a single crystal substrate. *Surface Science* 2016, 643: 117-123.

62. Takeuchi M, Sakamoto K, Martra G, Coluccia S, Anpo M. Mechanism of photoinduced superhydrophilicity on the $TiO_2$ photocatalyst surface. *The Journal of Physical Chemistry B* 2005, 109(32): 15422-15428.

63. Shao M-h, Liu P, Adzic RR. Superoxide anion is the intermediate in the oxygen reduction reaction on platinum electrodes. *Journal of the American Chemical Society* 2006, 128(23): 7408-7409.

64. Hayyan M, Hashim MA, AlNashef IM. Superoxide ion: generation and chemical implications. *Chemical Reviews* 2016, 116(5): 3029-3085.

65. Gong Y, Zhou M, Andrews L. Spectroscopic and theoretical studies of transition metal oxides and dioxygen complexes. *Chemical Reviews* 2009, 109(12): 6765-6808.

66. Gong Y, Zhou M, Tian SX, Yang J. Interconvertible side-on- and end-on-bonded oxo−superoxo titanium ozonide complexes. *The Journal of Physical Chemistry A* 2007, 111(28): 6127-6130.

67. Shibata T, Irie H, Tryk DA, Hashimoto K. Effect of residual stress on the photochemical properties of $TiO_2$ thin films. *The Journal of Physical Chemistry C* 2009, 113(29): 12811-12817.

68. Soria J, Sanz J, Sobrados I, Coronado JM, Maira AJ, Hernández-Alonso MD, Fresno F. FTIR and NMR study of the adsorbed water on nanocrystalline anatase. *The Journal of Physical Chemistry C* 2007, 111(28): 10590-10596.

69. Adams LK, Lyon DY, Alvarez PJJ. Comparative eco-toxicity of nanoscale $TiO_2$, $SiO_2$, and ZnO water suspensions. *Water Research* 2006, 40(19): 3527-3532.

70. Rashid M, Price NT, Gracia Pinilla MÁ, O'Shea KE. Effective removal of phosphate from aqueous solution using humic acid coated magnetite nanoparticles. *Water Research* 2013, 123: 353-360.

71. Sakai N, Fukuda K, Shibata T, Ebina Y, Takada K, Sasaki T. Photoinduced hydrophilic conversion properties of titania nanosheets. *The Journal of Physical Chemistry B* 2006, 110(12): 6198-6203.

72. Hustert K, Moza PN. Photochemical degradation of dicarboximide fungicides in the presence of soil constituents. *Chemosphere* 1997, 35(1): 33-37.

73. Hung ST, Mak MKS. Titanium dioxide photocatalysed degradation of organophosphate in a system simulating the natural aquatic environment. *Environmental Technology* 1993, 14(3): 265-269.

74. Giguère PA. The infra-red spectrum of hydrogen peroxide. *The Journal of Chemical Physics* 1950, 18(1): 88-92.

75. Lei P, Wang F, Zhang S, Ding Y, Zhao J, Yang M. Conjugation-grafted-$TiO_2$ nanohybrid for high photocatalytic efficiency under visible light. *ACS Applied Materials & Interfaces* 2014, 6(4): 2370-2376.

76. Brandán SA, Márquez López F, Montejo M, López González JJ, Ben Altabef A. Theoretical and experimental vibrational spectrum study of 4-hydroxybenzoic acid as monomer and dimer. *Spectrochimica Acta Part A: Molecular and Biomolecular Spectroscopy* 2010, 75(5): 1422-1434.

77. Trivedi M, Branton A, Trivedi D, Shettigar H, Bairwa K, Jana S. Fourier transform infrared and ultraviolet-visible spectroscopic characterization of biofield treated salicylic acid and sparfloxacin. *Natural Products Chemistry & Research* 2015, 3(5).

78. Nishijo J, Morita N, Asada S, Nakae H, Iwamoto E. Interaction of theophylline with bovine serum albumin and competitive displacement by benzoic acid. *CHEMICAL & PHARMACEUTICAL BULLETIN* 1985, 33(7): 2648-2653.

79. Yu J, Liu J-Y, Xiong W-M, Zhang X-Y, Zheng Y. Binding interaction of sodium benzoate food additive with bovine serum albumin: multi-spectroscopy and molecular docking studies. *BMC Chemistry* 2019, 13(1): 95.

# Chapter 6 CuS Nanoparticles in Humid Environments: Adsorbed Water Enhances the Transformation of CuS to $CuSO_4$

## 6.1 Abstract

Covellite copper sulfide nanoparticles (CuS NPs) have attracted immense research interest due to their widespread use in a range of biological and energy applications. As such, it is crucial to understand transformations of these nanomaterials and how these transformations influence the behavior of these nanoparticles in environmental and biological systems. This study specifically focuses on understanding the role of water vapor and adsorbed water in the transformation of CuS NP surfaces to $CuSO_4$ in humid environments. Surface sulfide ions are oxidized to sulfate by oxygen in the presence of water vapor, as detected by atomic force microscopy infrared spectroscopy (AFM-IR) and in-situ attenuated total reflectance Fourier transform infrared spectroscopy (ATR–FTIR). These results show that the transformation of CuS to $CuSO_4$ is highly dependent on relative humidity. Sulfide to sulfate conversion is not observed to any great extent at low RH (< 20%) whereas there is significant conversion at higher RH (> 80%). X-ray photoelectron spectroscopy (XPS) analysis confirms that sulfide is irreversibly oxidized to sulfate. Furthermore, it shows that initially Cu ions possess the original oxidation state as the original covellite, i.e. $Cu^+$, but then these are oxidized to $Cu^{2+}$ at high RH. The formation of $CuSO_4$ has also been confirmed by HRTEM. These analyses show that adsorbed water on the NP surfaces enhances the conversion of sulfide to sulfate and the oxidation of surface copper from $Cu^+$ to $Cu^{2+}$ in the presence of molecular oxygen.

## 6.2 Introduction

With the rapid development of nanotechnology in the past decades, nanomaterials have been widely applied in many aspects, e.g. catalysts, cosmic products, drug delivery media, sensor

or electrode materials.[1-4] Among various types of nanomaterials, copper sulfide nanomaterials have been attracting research attention due to its unique properties and applications in chemical sensors and catalysis.[2, 5-7] Copper sulfide represents a family of chemical compounds including two prominent forms: chalcocite ($Cu_2S$) and covellite (CuS). Covellite is known as the relatively more stable structure when exposed to oxidizing conditions at atmospheric pressure.[8] Additionally, covellite nanoparticles (NP) have tunable localized surface plasmon resonances (LSPR) in the near-infrared region.[9] Therefore, in addition to the applications as sensor and electrode materials, covellite NPs have received significant attention as a potential material for imaging and photothermal therapies.[10-12]

Although the toxicity of covellite NPs is limited by its low solubility in water,[13, 14] given the wide biological and catalytic applications, these NPs experience an array of different reactive conditions, such as within biological organisms and/or release into the environment which can impact is solubility through the adsorption of chelating ligands and surface transformations. Thus, there are concerns about potential toxicity generated from surface transformations of covellite NPs.

Water vapor has been reported to be reactive with some semiconductors by promoting surface oxidation, such as NiS.[15] However, few studies directly address covellite NP oxidation in presence of molecular oxygen and water vapor. Herein, we investigated surface transformations of covellite NPs at different RHs. These transformations were observed through *ex-situ* (AFM–IR spectroscopy and XPS) and *in-situ* methods (ATR–FTIR spectroscopy) as a function of relative humidity (RH). The results indicate these transformations are promoted in the presence of water, forming $CuSO_4$ at high RH levels. The physiochemical properties of CuS NPs are highly dependent on the surface states coatings.[16-20] Thus, formation of a $CuSO_4$ surface layer can alter the physiochemical properties of the nanoparticle, e.g. it can lead to increased solubility and

enhanced dissolution when exposed to the same biological and environmental ileu in which the original CuS NPs are considered inert. As reported in previous studies, Cu ions are cytotoxins, able to damage DNA and proteins.[21-25] As such, transformations of CuS nanoparticle surfaces have a range of potential consequences from its use in different applications to its toxicity.

## 6.3 Experimental Details

### 6.3.1 Synthesis of Covellite Nanoparticles

A typical method is employed by mixing 0.456g copper (II) nitrate • hexahydrate (Sigma Aldrich), 0.6 g thiourea (Acros Organics), and 20mL of ethylene glycol (Fisher Scientific) in a 50 mL three neck flask. The system is under initial vacuum and then nitrogen gas is introduced to minimize exposure to air. The the temperature was raised to 110 ºC and kept for ten minutes. A mixture of 5mL of 1M sodium hydroxide and 5 mL ethylene glycol was injected into the flask. The solution was then held for an additional five minutes before cooling down to room temperature. The CuS NPs were separated by centrifuging for 10 mins at 10,000 rpm. The NPs were washed four times by water quickly to remove the excessive ions and precursors. The as-synthesized CuS NPs were immediately transferred a vacuum desiccator to avoid potential further oxidation by air.

### 6.3.2 CuS Nanoparticle Characterization

The crystalline lattice was analyzed by powder X-ray diffraction (PXRD). XRD was performed on a Bruker AXS D8 FOCUS diffractometer equipped with Cu-K radiation ($\lambda$ = 1.54180 Å). The low-resolution transmission electron microscopy images were obtained by using TECNAI G2 SPHERA transmission electron microscopy (TEM) operated at 80 kV. High-resolution TEM (HRTEM) images were carried out on a JEOL JEM-2800 (HR) electron microscope operated at 200 kV.

### 6.3.3 AFM-PTIR Spectroscopy

Samples were analyzed using a nanoIR2 (Anasys Instruments - Bruker, Santa Barbara, CA) microscopy system equipped with a tunable mid-IR optical parametric oscillator laser (OPO). AFM imaging of conducted under ambient conditions at 298 K and a relative humidity (RH) of ~40% at ambient pressure. Images were collected at a scan rate of 0.5 Hz using gold-coated silicon nitride probes (tip radius ≤ 30 nm) 0.07 – 0.4 N $m^{-1}$ spring constant and 13 ± 4 kHz resonant frequency in contact mode. Photothermal infrared (PTIR) spectra were collected at different locations across the surface with a nominal spatial resolution of < 30 nm, a spectral resolution of 8 $cm^{-1}$, co-averaging 128 laser pulses per wavenumber. All spectra shown are taken on a single point with no smoothing filters applied. Background corrections were done by substrate subtraction using a spectrum taken on the bare gold roughly 100 nm away. Chemical maps were taken by keeping the laser at a fixed wavelength, with a scan rate of 0.1 Hz, averaging 8 times per pixel.

### 6.3.4 X-Ray Photoelectron Spectroscopy

X-ray photoelectron spectroscopy (XPS) measurements were performed by using an AXIS Supra by Kratos Analytical. The binding energy was calibrated against adventitious carbon 1s peak at 284.5 eV.

### 6.3.5 ATR–FTIR Spectroscopy

ATR–FTIR spectra were recorded using a 500 µl horizontal ATR flow cell with an AMTIR element (Pike Technologies Inc.). A Nicolet 6700 FTIR spectrometer equipped with an MCT-A detector was used. Each spectrum was collected with 264 scans at an instrument resolution of 4 $cm^{-1}$ in the AMTIR spectral range (750 to 4000 $cm^{-1}$). CuS NPs, 3 mg, were dispersed in 1 mL

methanol and dropped on the AMTIR element. The slurry was dried in a nitrogen atmosphere overnight.

## 6.4 Results and Discussion

### 6.4.1 Characterization of CuS Nanoparticles

The morphology of the as-synthesized NPs was characterized by TEM. The NPs are seen to be aggregated as shown in Figure 6.1a with individual particles size of around 8 nm. The fine crystalline structure of the CuS NPs is analyzed by PXRD, as shown in Figure 6.1c. The standard data for covellite (JCPDS no. 06-0464) is also shown as blue bars in Figure 6.1c for comparison. The diffraction peaks are indexed to different planes: (101), (102), (103), (006), (106), (110), (108) and (116) plane. All of these different planes agree well with the standard data assigned to covellite phase. The overlapped peaks (103) and (006) are weaker than the one (110) suggests that

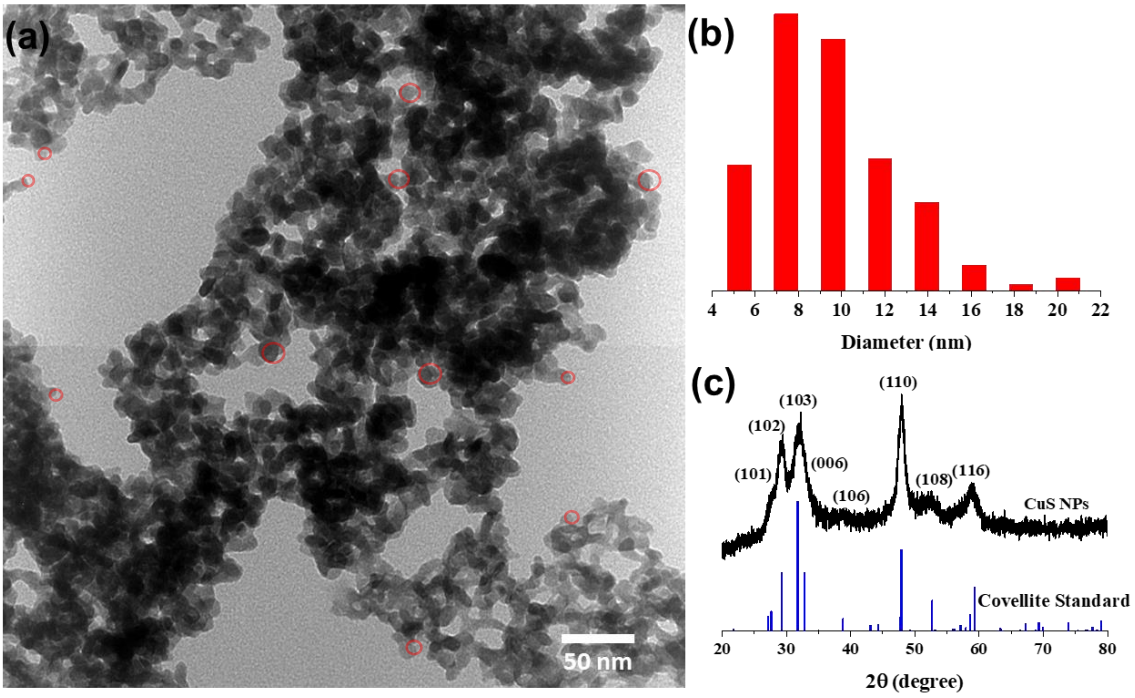


**Figure 6.1** (a) TEM image of the as-synthesized covellite nanoparticles. (b) Size distribution of the individual nanoparticles within the observed aggregates were determined by measuring the diameter of distinct particles which were typically at the edge of the larger aggregate (e.g. see red circles within the image). (c) powder X-ray diffraction data of as-synthesized covellite NPs to standard diffraction data for the covellite phase.

preferential growth of CuS NPs is along with <110> directions, also indicating polysulfide in CuS.[26]

6.4.2 ATR–FTIR Spectroscopy

The ATR–FTIR spectra shown in Figure 6.2 provides evidence for surface transformations and oxidation by monitoring the appearance of new vibrational bands as the CuS nanoparticles are exposed to oxygen at different relative humidity. The oxidation product of interest is $SO_4^{2-}$ which displays vibrational frequencies in the spectral range from around 900 to 1100 $cm^{-1}$, as labeled in Figure 6.2. As shown in these spectra, the peaks in this region do not become apparent at low RH 2% but do show up at RH 39 and 87%. The fundamental vibration frequencies of an isolated sulfate ion, $SO_4^{2-}$, with $T_d$ symmetry, is around 971–993 and 1070 –1190 $cm^{-1}$ for the symmetric stretching and asymmetric stretching modes, respectively.[27-29] The surface oxidized spectra are more complicated that simple isolated sulfate ion due to various interactions with the surface leading to

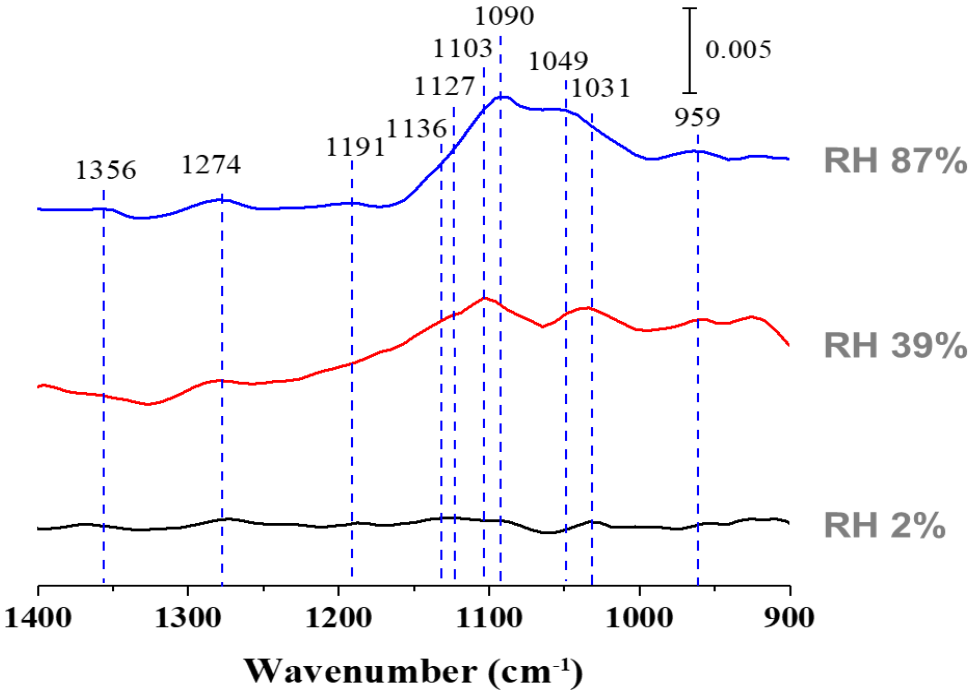


**Figure 6.2** ATR-FTIR spectra of oxidized covellite after 2 hrs. at RH 2%, RH 39% and RH 87%, respectively.

both a decrease in symmetry of the ion and different bonding mode coordinating to the surface. [27, 30] Previous literatures proposed sulfate may interact with a surface i.e. hematite or fluorite by forming inter-sphere complex with surface cations, which display the $C_{3v}$ (monodentate with three absorption bands) and $C_{2v}$ (bidentate with four absorption bands) symmetry. Thus, the peaks in this region are consistent with the formation of sulfate. For example, A broad peak centered around 959 $cm^{-1}$ appearing at high RH values is assigned to symmetric stretching vibration for adsorbed species. The lower value for the symmetric stretching than the isolated ion suggests that sulfate may interact with water or $OH^-$ and Cu ions on the surface (i.e. S–O ••• OH/$H_2O$ ••• $Cu^+$) that is similar the interaction found in $Cu_x(OH)_ySO_4$ compounds.[29, 30] The asymmetric stretching of S–O shows multiple peaks depending on the coordination environment. For example, peaks near at 1049, 1136, and 1191 $cm^{-1}$ may be assigned to a bidentate complex, and the bands at 1031 and 1127 $cm^{-1}$ to a monodentate complex.[28, 30, 31] A previous study about adsorbed sulfate on surface

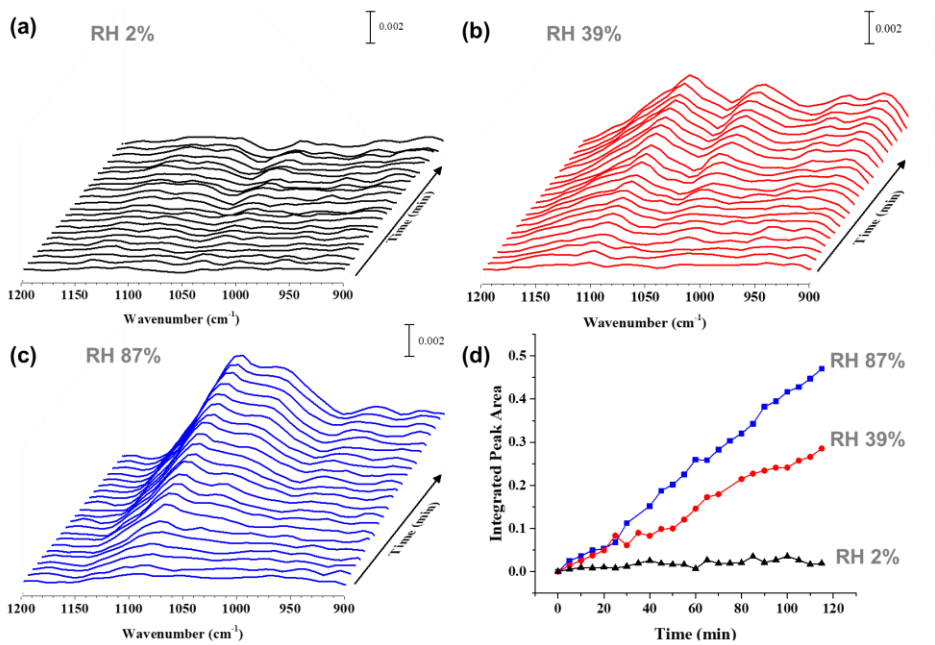


**Figure 6.3** (a) (b) (c) ATR-FTIR spectra of CuS under ambient conditions as a function of time at different RH: 2%, 39% and 87%, respectively. (d) Integrated peak area of sulfate absorption bands (1050 to 1170 $cm^{-1}$). Each spectrum was recorded every five minutes for a total time of 120 minutes.

indicates that the peak at 1360 $cm^{-1}$ might be caused by the formation of polysulfate onto the surface.[30] Additionally, the peak at 1274 $cm^{-1}$ may reflect the formation adsorbed sulfate–water structure.[30, 32] In order to determine if adsorbed water may cause the oxidation of sulfide, a control experiment was carried out under nitrogen atmosphere. The comparison suggests that molecular oxygen acts as the oxidant but not water in the oxidation process.

The time dependence of the surface oxidation process was observed in situ by ATR–FTIR spectroscopy as shown in Figure 6.3. At low RH, 2%, there is no change in the vibrational spectra. However, the intensity of sulfate peaks increases with oxidation time at higher RHs. The integrated peak areas from 1050 to 1170 $cm^{-1}$ are plotted as a function of time at the different RH. These data

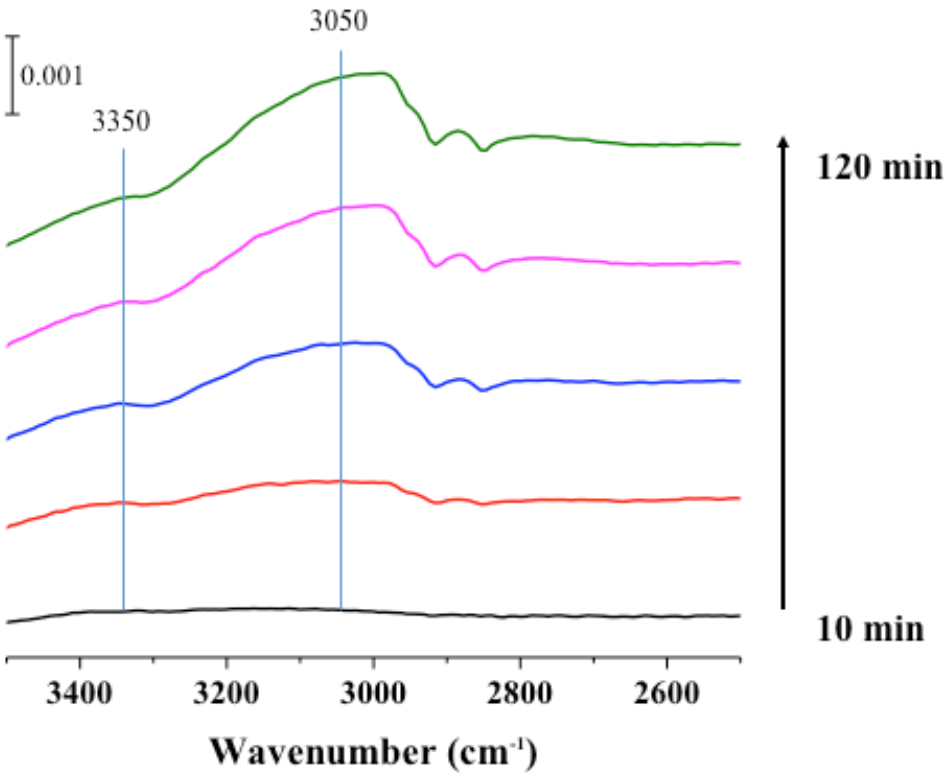


**Figure 6.4** ATR-FTIR spectra in the spectral region extending from 2500 to 3600 $cm^{-1}$ as a function of time following. This is the same experiment shown in Figure 6.2 but for a different spectral region. It can be seen that as the surface transforms a broad peak grows in during at RH 87% in this higher wavenumber region. This is associated with adsorbed water on the surface.

show that the rate of sulfate formation is ca. 1.5 times faster at 87% versus 39% RH whereas there is no formation at 2% RH.

In order to better understand the interaction of water with the surface, the spectral region from 2600 to 3500 $cm^{-1}$ was monitored during reaction at 87% RH as shown in Figure 6.4. As the time proceeds, a very broad band appears in the spectra. It is interesting that the strongest broad peak is at low wavenumbers that that typically found for the O–H stretch of adsorbed water. However, reports of low frequency bands even as low as 2980 $cm^{-1}$ have been attributed to O–H stretching mode of $Cu(H_2O)_n^+$, indicating that water molecules bond to surface Cu ions.[33] In addition, there is a broad peak around 3350 $cm^{-1}$ which is closer in frequency to the O–H stretching vibration of water molecules not directly bonded to surface metal ions but instead interacting with the surface and other adsorbed water through hydrogen bonding interactions. Overall, these data suggest that water adsorbs on the surface and participates in the oxidation of sulfide to sulfate. This transformation is irreversible as the sulfate peaks do not decrease over time in the absence of oxygen and relative humidity. Our results are in agreement with the previous simulation that the adsorption and oxidation of iron sulfide surfaces can be enhanced due to adsorbed water.[34]

### 6.4.3 X-Ray Photoelectron Spectroscopy in Cu 2p and S 2p Regions

A study by Evans Jr. *et al*. indicates that covellite has an unique crystalline structure of hexagonal close-packing: Cu atoms occupy two different sites - tetrahedral and triangular coordination; S atoms form disulfide groups and single sulfide ions, as shown in Figure 6.5a.[35] $Cu_3S$ and $CuS_3$ layers resemble through disulfide bridge. The valence of Cu and S in covellite has been the subject of debate for years.[18, 36-41] Covellite is normally described as mixed valance state of Cu and S. Previous studies proposed that the appropriate oxidation formalism for CuS is proposed to be $(Cu^+)_3S^{2-}(S_2)^-$, in which oxidation state of Cu in covellite CuS is $Cu^+$ rather than

$Cu^{2+}$ and S has various valences such $S^{2-}$ and $S_2^-$.[36, 37] However, other studies carried by $^{63}Cu$ NMR indicates Cu possesses mixed valence states with $Cu^+$ and $Cu^{2+}$.[39, 42-44] Furthermore, simulations have propose a structure with no integer valences for the copper ions.[45] Here we employ X-ray photoelectron spectroscopy to analyze the surface chemical states of covellite NPs. Figure 6.5b depicts the Cu 2p and S 2p regional XPS spectra of the freshly synthesized covellite NPs under

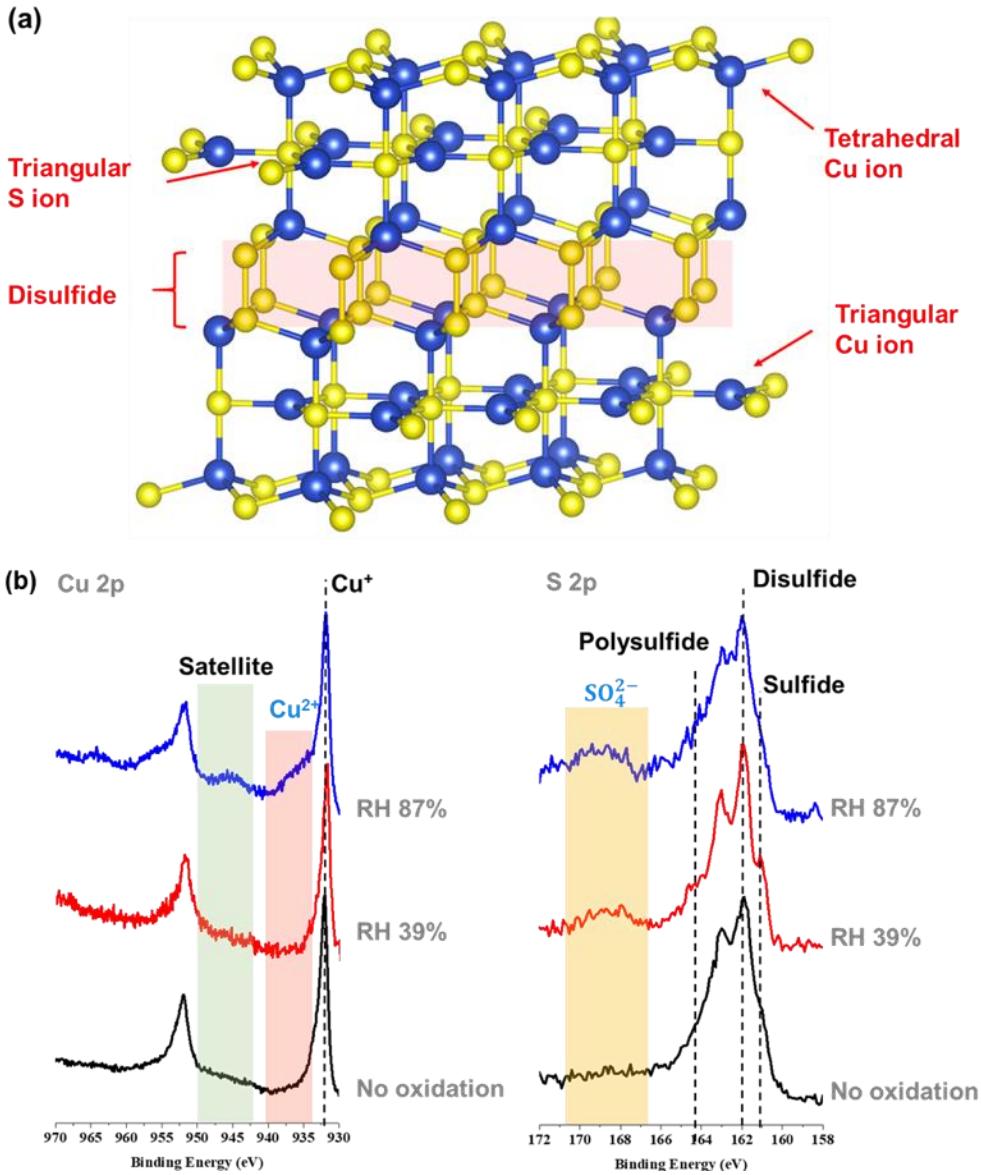


**Figure 6.5** (a) crystal model of covellite, (b) High-resolution XPS characterization of covellite samples under various condition: Cu 2p region (left) and S 2p region (right). The blue spheres represent Cu and the yellow spheres represent sulfur. The binding models are visualized by VESTA.

different conditions. According to XPS results shown in Figure 6.5b, the freshly synthesized covellite NPs do not show noticeable oxidation even though sample transfer process exposed to room air for a short time. In contrast, the samples exposed to pure oxygen in presence of water vapor display sulfide oxidation as evident by sulfate at 168 eV in the S 2p region.[46] The peaks at 161.8 and 163.0 eV are regarded as S 2p1/2 in sulfide compounds,[47] and the other peak of S at 164.2 eV is very close to polysulfide 2p1/2 in chalcogenides caused by high Cu-deficiency in the near surface region.[18, 26, 48, 49] The XPS in the Cu 2p region displays two intense doublet peaks at 932.0 and 951.9 that are assigned to 2p3/2 and 2p1/2 consistent with Cu in covellite, respectively.[36] As shown in Figure 6.5b, Cu peaks at 932.0 eV have asymmetric tails which is caused by kinetic energy losses in the interaction of photoelectrons with free charge carriers and is no evidence for $Cu^{2+}$ as described previously. [18] It is also important to note that shake-up satellite peaks at around 945 and 965 eV originating from Cu (II) [50, 51] are not observed in XPS spectra for freshly synthesized sample and sample oxidized at RH 39%, indicating $Cu^{+}$ is mainly the main format in covellite NPs instead of $Cu^{2+}$.[4, 52] For the sample, oxidized at RH 87%, the Cu 2p spectrum indicates a peak showing around 936 eV for the compound of $CuSO_4$ as labeled in the Figure 6.5b, while this is not noticeable for the freshly synthesized sample, the sample oxidized under RH 39% does show evidence for $Cu^{2+}$. It is evident that at high RH surface copper ions in covellite are also oxidized and the product that forms is $CuSO_4$, however at lower relative humidity, RH 39%, the formation of an unusual $Cu_2SO_4$ surface species is suggested, possibly an intermediate prior to formation of $CuSO_4$ that is seen for higher RH.

6.4.4 Imaging Techniques: Atomic Force Microscopy Coupled to Infrared Spectroscopy and High-Resolution Transmission Electron Microscopy

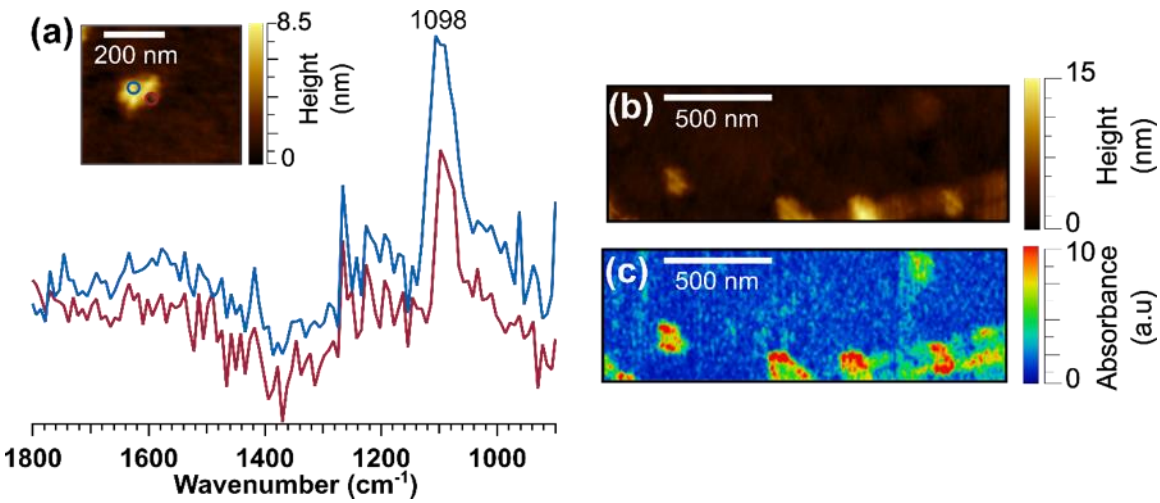


**Figure 6.6** (a) PTIR spectroscopy for particles, with an inset showing the corresponding AFM height image of oxidized covellite NPs exposed to pure oxygen for 24 hrs at RH 87% with height images. (b) AFM height image and (c) chemical map of the sulfate rich regions of the particle taken at 1098 $cm^{-1}$.

Additional insights into the transformation of nanoparticles can be obtained through imaging techniques. Figure 6.6 shows the PTIR spectra and the corresponding AFM image of the 87% RH oxidized CuS NPs deposited on a gold substrate utilizing AFM-PTIR spectroscopy. Individual NPs are expected to be ca. 8 nm in diameters, and the AFM spectra show that the nanoparticles remain highly aggregated when deposited onto the surface but mostly in two dimensions, x-y plane not in the z-direction which is a measurement of the height. PTIR spectra taken on the center and edge of a particle show a single peak at 1098 $cm^{-1}$. As both CuS and the underlying gold substrate do not have any vibrational modes in the mid-infrared spectral region, this peak can be attributed to the $\nu_{as}(SO_4^{2-})$ from oxidation of the CuS NPs. Although AFM-IR is not a surface selective technique, we expect the aggregates to contain the oxidized material, and subsequently provide enough sulfate ions for signal detection. Chemical maps taken at 1098 $cm^{-1}$ show the spatial distribution of the sulfate absorbing regions, which are highest at the center of the

aggregate. The presence of these sulfate modes provides further evidence that these sulfate containing NPs are formed irreversibly under elevated humidity. The presence of these sulfate modes provides further evidence that these sulfate containing NPs are formed irreversibly under elevated humidity.

In order to further confirm the formation of $CuSO_4$ at high RH, the reacted sample was imaged by HRTEM. Figure 6.7a shows the HRTEM image of the oxidized sample at RH 87%.

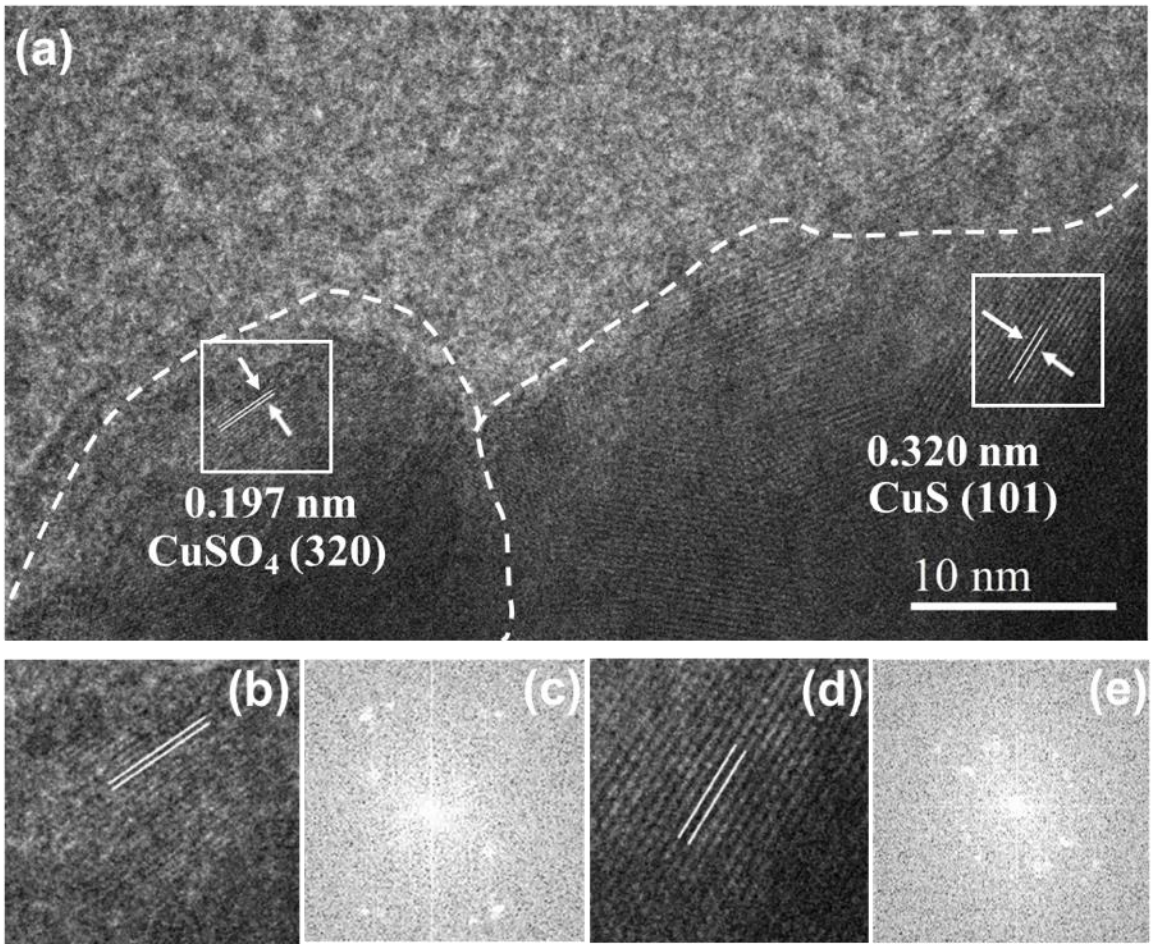


**Figure 6.7** (a) High resolution TEM image of covellite NPs after oxidation at RH 87%, (b) the selected $CuSO_4$ phase, (c) the FFT pattern of the selected $CuSO_4$ phase, (d) the selected CuS phase, (e) the FFT pattern of the selected CuS phase.

The corresponding FFT pattern of HRTEM fringes also indicate with two distinct crystal phases. The d-spacing values are 0.197 nm and 0.320 nm, respectively. The former one is very close to

the value for crystal facet (320) of $CuSO_4$ (PDF 15-0775) and the latter is for (101) of covellite (PDF 15-0775). Therefore, the new features rather than CuS is likely caused by the formation of $CuSO_4$.

### 6.4.5 Surface Transformations and Oxidation of CuS in Humid Environments

Surface transformations of CuS, covellite, NPs are shown in humid environments when exposed to air. Simulations show that oxygen preferentially adsorbs on sulfide surfaces compared to water[53] with molecular oxygen reversibly adsorbing onto covellite NP surfaces when covered by organic surfactants (e.g. oleylamine),[17] whereas the molecular oxygen reacts with surface sulfide in the form of sulfate at the early oxidation stage without ligand protection as seen here. In addition to sulfide oxidation, oxygen can also chemically bond to the copper ion center on the sulfide surface.[34, 53] Oxygen acts as an electron acceptor and able to oxidize both $Cu^+$ and sulfide ions. Furthermore, the reduced oxygen ion is reported to generate reactive oxygen species with the help from $Cu^+$.[54] Therefore, we propose the following mechanism for the formation of $\mathbf{Cu^{2+}}$ and $\mathbf{SO_4^{2-}}$.

$$\mathbf{H_2O \rightarrow H^+ + OH^-} \tag{6.1}$$

$$\mathbf{H_2O + S^{2-} \rightarrow HS^- + OH^-} \tag{6.2}$$

$$\mathbf{O_2 + 2HS^- \rightarrow H_2O_2 + S_2^{2-}} \tag{6.3}$$

$$\mathbf{O_2 + Cu^+ \rightarrow O_2^- + Cu^{2+}} \tag{6.4}$$

$$\mathbf{O_2^- + 2H^+ + Cu^+ \rightarrow H_2O_2 + Cu^{2+}} \tag{6.5}$$

$$\mathbf{H_2O(ad) + Cu^{2+} \rightarrow H^+(ad) + OH^{\bullet}}\text{(ad)} \ \mathbf{+Cu^+} \tag{6.6}$$

$$\mathbf{2OH^{\bullet}(ad) \rightarrow H_2O_2} \tag{6.7}$$

$$\mathbf{H_2O_2 + 2S^{2-}/S_2^{2-} \rightarrow 4H_2O + SO_4^{2-}} \qquad (6.8)$$

Several important features can be gleaned from the proposed mechanism. First, there is the formation of reactive oxygen species (ROS) including superoxide, hydroxyl free radical and hydrogen peroxide. The ROS can further oxidize sulfide and disulfide to sulfate. Second, ROS in Step 5 reacts with protons from water molecules to yield $Cu^{2+}$ and hydrogen peroxide. Thus, in a water-free environment the oxidation processis inhibited resulting in little transformation of the sulfide surface. It is interesting that the adsorption of water is enhanced on the oxidized surface as seen in the infrared spectra. This indicates an increase in the adsorption energy.[34]

Transformation processes under different RHs are summarized in Figure 6.8 in a simplified schematic. As depicted in Figure 6.8, the covellite surface dissolves into copper, sulfide and disulfide ions in the water layer, while under dry condition (e.g. ~RH 2%), this does not occur

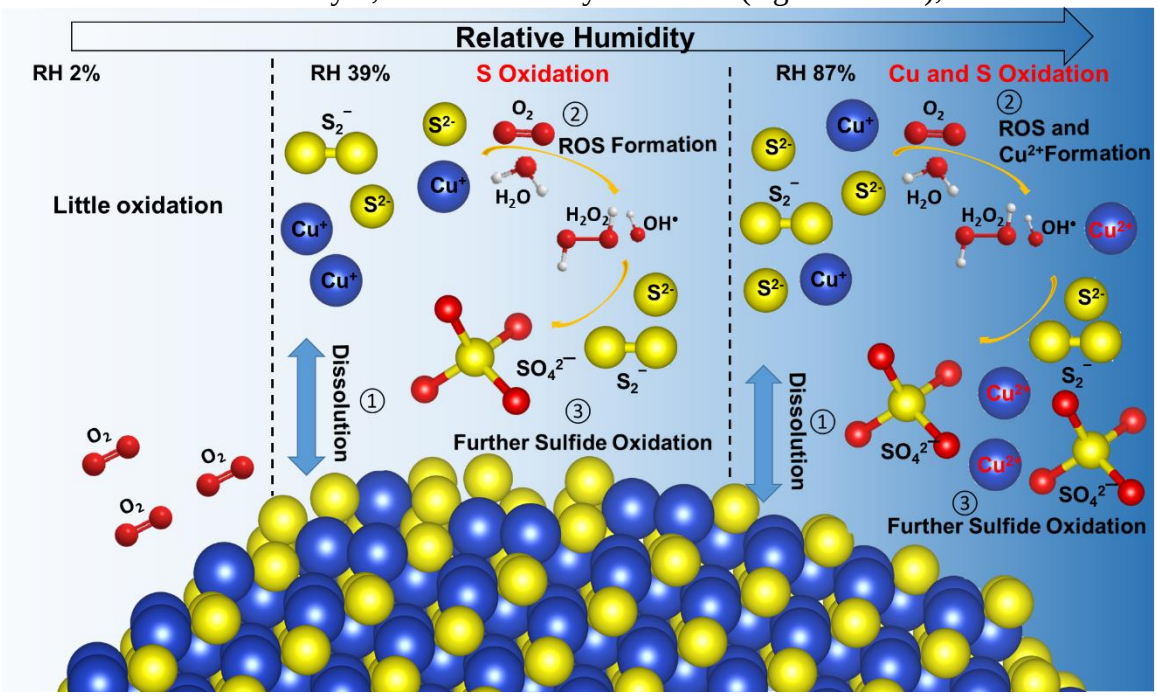


**Figure 6.8** Simplified schematic of the surface during the transformation of CuS nanoparticles under different relative humidity. The transformation processes are composed of three main steps: (1) CuS dissolution in adsorbed water, (2) ROS formation initiated by oxygen in presence of water, (3) further sulfide oxidation by ROSs. At RH 87%, $Cu^{+}$ also transforms to $Cu^{2+}$.

since little water adsorbs onto NP surfaces. The dissolved sulfide ions may hydrolyze to HS– that is are oxidized by oxygen gas through a two electron reaction of oxygen species involving formation reactive oxygen species as intermediates.[55] Moreover, water also serves as a hard base to stabilize relatively hard acid $Cu^{2+}$ rather than softer $Cu^{+}$ in CuS.[18] Additionally, previous studies of sulfide oxidation show that active metal centers on surface can promote adsorbed water to form hydroxyl free radicals.[34, 53, 56, 57, 58] The generation of ROS enhances the oxidation and speeds up these surface transformations. Overall, water is thought to play three key roles: (1) water serves as a medium for the dissolution of CuS; (2) water provides protons for the initial oxidation step by oxygen as shown in the reaction mechanism; (3) water attached to metal centers can dissociate into ROS as an intermediate to accelerate surface oxidation. Thus, water is able to accelerate the oxidation, so that CuS is oxidized to $CuSO_4$ at high RH i.e. 87%. Interestingly, at RH 39%, there is no $Cu^{+}$ oxidation observed. Therefore, this suggests that $Cu_2SO_4$ is on the nanoparticle surface and perhaps an intermediate to $CuSO_4$ at higher RH. Taken together he results imply the surface of covellite CuS NPs is vulnerable to air oxidation in humid environments.

## 6.5 Conclusions

In summary, the transformation of covellite NP surfaces under ambient conditions at different RHs has been systematically investigated. These results show that the synthesized NP surface is more reactive toward oxygen in the presence of water. High RH increases the oxidation rate and with the formation of $CuSO_4$ formation at 87% RH Interestingly, the transformation of $Cu^{+}$ to $Cu^{2+}$ is not observed at intermediate relative humidity of 39%, while sulfate does form suggesting that $Cu_2SO_4$ may be an intermediate in the reaction to $CuSO_4$. Adsorbed water is proposed to be a medium for this reaction to occur by favoring the surface dissolution of CuS to the corresponding ions and provide protons to yield ROS by oxygen. The conversion of CuS to

$CuSO_4$ found in this study will provide insights and an understanding of the potential impact this chemistry may have in biological and environmental systems.

## 6.6 Acknowledgements

This work is supported by the National Science Foundation under grant number CHE1606607. XPS was performed at the UC Irvine Materials Research Institute (IMRI) using instrumentation funded in part by the National Science Foundation Major Research Instrumentation Program under grant no. CHE-1338173. HR-TEM was also performed at the UC Irvine Materials Research Institute (IMRI).

Chapter 6 is in preparation for submission: Haibin Wu, Victor Or, Sabrina Gonzalez-Calzada, Vicki H. Grassian. "CuS Nanoparticles in Humid Environments: Adsorbed Water Enhances the Transformation of CuS to $CuSO_4$".

## 6.7 References


1. Park JY, Kim SJ, Yim K, Dae KS, Lee Y, Dao KP, Park JS, Jeong HB, Chang JH, Seo HK, Ahn CW, Yuk JM. Pulverization-Tolerance and Capacity Recovery of Copper Sulfide for High-Performance Sodium Storage. *Advanced Science* 2019, 6(12): 1900264.

2. Thiele P, Neumann J, Westphal A, Ludwig R, Bonsa A-M, Appelhagen A, Malcher P, Köckerling M. Electrical Energy Storage by a Magnesium-Copper-Sulfide Rechargeable Battery. *Journal of the Electrochemical Society* 2017, 164(4): A770-A774.

3. Wu H, Chen W. Synthesis and reaction temperature-tailored self-assembly of copper sulfide nanoplates. *Nanoscale* 2011, 3(12): 5096-5102.

4. Wu H, Chen W. Copper Nitride Nanocubes: Size-Controlled Synthesis and Application as Cathode Catalyst in Alkaline Fuel Cells. *Journal of the American Chemical Society* 2011, 133(39): 15236-15239.

5. Lee H, Yoon SW, Kim EJ, Park J. In-Situ Growth of Copper Sulfide Nanocrystals on Multiwalled Carbon Nanotubes and Their Application as Novel Solar Cell and Amperometric Glucose Sensor Materials. *Nano Letters* 2007, 7(3): 778-784.

6. Wu Y, Wadia C, Ma W, Sadtler B, Alivisatos AP. Synthesis and Photovoltaic Application of Copper(I) Sulfide Nanocrystals. *Nano Letters* 2008, 8(8): 2551-2555.

7. Kar P, Farsinezhad S, Zhang X, Shankar K. Anodic Cu2S and CuS nanorod and nanowall arrays: preparation, properties and application in $CO_2$ photoreduction. *Nanoscale* 2014, 6(23): 14305-14318.

8. Roberts WMB, Buchanan AS. The effects of temperature, pressure, and oxygen on copper and iron sulphides synthesised in aqueous solution. *Mineralium Deposita* 1971, 6(1): 23-33.

9. Comin A, Manna L. New materials for tunable plasmonic colloidal nanocrystals. *Chemical Society Reviews* 2014, 43(11): 3957-3975.

10. Gao W, Sun Y, Cai M, Zhao Y, Cao W, Liu Z, Cui G, Tang B. Copper sulfide nanoparticles as a photothermal switch for TRPV1 signaling to attenuate atherosclerosis. *Nature Communications* 2018, 9(1): 231.

11. Brannigan RP, Dove AP. Synthesis, properties and biomedical applications of hydrolytically degradable materials based on aliphatic polyesters and polycarbonates. *Biomaterials Science* 2017, 5(1): 9-21.

12. Wang S, Riedinger A, Li H, Fu C, Liu H, Li L, Liu T, Tan L, Barthel MJ, Pugliese G, De Donato F, Scotto D'Abbusco M, Meng X, Manna L, Meng H, Pellegrino T. Plasmonic Copper Sulfide Nanocrystals Exhibiting Near-Infrared Photothermal and Photodynamic Therapeutic Effects. *ACS Nano* 2015, 9(2): 1788-1800.

13. Gramp JP, Sasaki K, Bigham JM, Karnachuk OV, Tuovinen OH. Formation of Covellite (CuS) Under Biological Sulfate-Reducing Conditions. *Geomicrobiology Journal* 2006, 23(8): 613-619.

14. Bhagat M, Burgess JE, Antunes APM, Whiteley CG, Duncan JR. Precipitation of mixed metal residues from wastewater utilising biogenic sulphide. *Minerals Engineering* 2004, 17(7): 925-932.

15. Legrand Daniel L, Nesbitt HW, Bancroft GM. X-ray photoelectron spectroscopic study of a pristine millerite (NiS) surface and the effect of air and water oxidation. *American Mineralogist* 1998, 83(12): 1256.

16. Xie Y, Carbone L, Nobile C, Grillo V, D'Agostino S, Della Sala F, Giannini C, Altamura D, Oelsner C, Kryschi C, Cozzoli PD. Metallic-like Stoichiometric Copper Sulfide Nanocrystals: Phase- and Shape-Selective Synthesis, Near-Infrared Surface Plasmon Resonance Properties, and Their Modeling. *ACS Nano* 2013, 7(8): 7352-7369.

17. Wei T, Liu Y, Dong W, Zhang Y, Huang C, Sun Y, Chen X, Dai N. Surface-Dependent Localized Surface Plasmon Resonances in CuS Nanodisks. *ACS Applied Materials & Interfaces* 2013, 5(21): 10473-10477.

18. Xie Y, Riedinger A, Prato M, Casu A, Genovese A, Guardia P, Sottini S, Sangregorio C, Miszta K, Ghosh S, Pellegrino T, Manna L. Copper Sulfide Nanocrystals with Tunable Composition by Reduction of Covellite Nanocrystals with $Cu^+$ Ions. *Journal of the American Chemical Society* 2013, 135(46): 17630-17637.

19. Ludwig J, An L, Pattengale B, Kong Q, Zhang X, Xi P, Huang J. Ultrafast Hole Trapping and Relaxation Dynamics in p-Type CuS Nanodisks. *The Journal of Physical Chemistry Letters* 2015, 6(14): 2671-2675.

20. Shamraiz U, Hussain RA, Badshah A. Fabrication and applications of copper sulfide (CuS) nanostructures. *Journal of Solid State Chemistry* 2016, 238: 25-40.

21. Pham AN, Xing G, Miller CJ, Waite TD. Fenton-like copper redox chemistry revisited: Hydrogen peroxide and superoxide mediation of copper-catalyzed oxidant production. *Journal of Catalysis* 2013, 301: 54-64.

22. Turnbull S, Tabner BJ, Brown DR, Allsop D. Copper-dependent generation of hydrogen peroxide from the toxic prion protein fragment PrP106–126. *Neuroscience Letters* 2003, 336(3): 159-162.

23. de Schamphelaere KAC, Janssen CR. A Biotic Ligand Model Predicting Acute Copper Toxicity for Daphnia magna: The Effects of Calcium, Magnesium, Sodium, Potassium, and pH. *Environmental Science & Technology* 2002, 36(1): 48-54.

24. Grosell M, Blanchard J, Brix KV, Gerdes R. Physiology is pivotal for interactions between salinity and acute copper toxicity to fish and invertebrates. *Aquatic Toxicology* 2007, 84(2): 162-172.

25. Jonas RB. Acute Copper and Cupric Ion Toxicity in an Estuarine Microbial Community. *Applied and Environmental Microbiology* 1989, 55(1): 43.

26. Yang Z, Li H, Feng S, Li P, Liao C, Liu X, Zhao J, Yang J, Lee P-H, Shih K. Multiform Sulfur Adsorption Centers and Copper-Terminated Active Sites of Nano-CuS for Efficient Elemental Mercury Capture from Coal Combustion Flue Gas. *Langmuir* 2018, 34(30): 8739-8749.

27. Jubb AM, Allen HC. Sulfate Adsorption at the Buried Fluorite–Solution Interface Revealed by Vibrational Sum Frequency Generation Spectroscopy. *The Journal of Physical Chemistry C* 2012, 116(16): 9085-9091.

28. Kunimatsu K, Samant MG, Seki H. In-situ FT-IR spectroscopic study of bisulfate and sulfate adsorption on platinum electrodes: Part 1. Sulfuric acid. *Journal of Electroanalytical Chemistry and Interfacial Electrochemistry* 1989, 258(1): 163-177.

29. SECCO EA. Spectroscopic properties of SO4 (and OH) in different molecular and crystalline environments. I. Infrared spectra of $Cu_4(OH)_6SO_4$, $Cu_4(OH)_4OSO_4$, and $Cu_3(OH)_4SO_4$. *Canadian Journal of Chemistry* 1987, 66: 329-336.

30. Hug SJ. In Situ Fourier Transform Infrared Measurements of Sulfate Adsorption on Hematite in Aqueous Solutions. *Journal of Colloid and Interface Science* 1997, 188(2): 415-422.

31. Jubb AM, Verreault D, Posner R, Criscenti LJ, Katz LE, Allen HC. Sulfate adsorption at the buried hematite/solution interface investigated using total internal reflection (TIR)-Raman spectroscopy. *Journal of Colloid and Interface Science* 2013, 400: 140-146.

32. Su Z, Climent V, Leitch J, Zamlynny V, Feliu JM, Lipkowski J. Quantitative SNIFTIRS studies of (bi)sulfate adsorption at the Pt(111) electrode surface. *Physical Chemistry Chemical Physics* 2010, 12(46): 15231-15239.

33. Iino T, Ohashi K, Inoue K, Judai K, Nishi N, Sekiya H. Infrared spectroscopy of Cu+(H2O)n and Ag+(H2O)n: Coordination and solvation of noble-metal ions. *The Journal of Chemical Physics* 2007, 126(19): 194302.

34. Li Y, Chen J, Chen Y, Zhao C, Zhang Y, Ke B. Interactions of Oxygen and Water Molecules with Pyrite Surface: A New Insight. *Langmuir* 2018, 34(5): 1941-1952.

35. Howeard T. Evans J, Konnert JA. Crystals tructurer efinemenot f covellite. *American Mineralogist* 1976, 61: 996-1000.

36. Goh SW, Buckley AN, Lamb RN. Copper(II) sulfide? *Minerals Engineering* 2006, 19(2): 204-208.

37. Liang W, Whangbo MH. Conductivity anisotropy and structural phase transition in Covellite CuS. *Solid State Communications* 1993, 85(5): 405-408.

38. Freymeyer NJ, Cunningham PD, Jones EC, Golden BJ, Wiltrout AM, Plass KE. Influence of Solvent Reducing Ability on Copper Sulfide Crystal Phase. *Crystal Growth & Design* 2013, 13(9): 4059-4065.

39. Saito S-h, Kishi H, Nié K, Nakamaru H, Wagatsuma F, Shinohara T. $^{63}$Cu NMR studies of copper sulfide. *Physical Review B* 1997, 55(21): 14527-14535.

40. Luther GW, Theberge SM, Rozan TF, Rickard D, Rowlands CC, Oldroyd A. Aqueous Copper Sulfide Clusters as Intermediates during Copper Sulfide Formation. *Environmental Science & Technology* 2002, 36(3): 394-402.

41. Pattrick RAD, Mosselmans JFW, Charnock JM, England KER, Helz GR, Garner CD, Vaughan DJ. The structure of amorphous copper sulfide precipitates: An X-ray absorption study. *Geochimica et Cosmochimica Acta* 1997, 61(10): 2023-2036.

42. Mazin II. Structural and electronic properties of the two-dimensional superconductor CuS with 1 1/3-valent copper. *Physical Review B* 2012, 85(11): 115133.

43. Kumar P, Nagarajan R, Sarangi R. Quantitative X-ray absorption and emission spectroscopies: electronic structure elucidation of $Cu_2S$ and CuS. *Journal of Materials Chemistry C* 2013, 1(13): 2448-2454.

44. Goh SW, Buckley AN, Lamb RN, Rosenberg RA, Moran D. The oxidation states of copper and iron in mineral sulfides, and the oxides formed on initial exposure of chalcopyrite and bornite to air. *Geochimica et Cosmochimica Acta* 2006, 70(9): 2210-2228.

45. Gainov RR, Dooglav AV, Pen'kov IN, Mukhamedshin IR, Mozgova NN, Evlampiev IA, Bryzgalov IA. Phase transition and anomalous electronic behavior in the layered superconductor CuS probed by NQR. *Physical Review B* 2009, 79(7): 075115.

46. Vasquez RP. $CuSO_4$ by XPS. *Surface Science Spectra* 1998, 5(4): 279-284.

47. Siriwardane RV, Poston JA. Interaction of $H_2S$ with zinc titanate in the presence of $H_2$ and CO. *Applied Surface Science* 1990, 45(2): 131-139.

48. Malitesta C, Centonze D, Sabbatini L, Zambonin PG, Bicelli LP, Maffi S. Analytical characterization by X-ray photoelectron spectroscopy of quaternary chalcogenides for cathodes in lithium cells. *Journal of Materials Chemistry* 1991, 1(2): 259-263.

49. Smart RSC, Skinner WM, Gerson AR. XPS of sulphide mineral surfaces: metal-deficient, polysulphides, defects and elemental sulphur. *Surface and Interface Analysis* 1999, 28(1): 101-105.

50. Biesinger MC. Advanced analysis of copper X-ray photoelectron spectra. *Surface and Interface Analysis* 2017, 49(13): 1325-1334.

51. Hayez V, Franquet A, Hubin A, Terryn H. XPS study of the atmospheric corrosion of copper alloys of archaeological interest. *Surface and Interface Analysis* 2004, 36(8): 876-879.

52. Llorente VB, Dzhagan VM, Gaponik N, Iglesias RA, Zahn DRT, Lesnyak V. Electrochemical Tuning of Localized Surface Plasmon Resonance in Copper Chalcogenide Nanocrystals. *The Journal of Physical Chemistry C* 2017, 121(33): 18244-18253.

53. Wei Z, Li Y, Gao H, Zhu Y, Qian G, Yao J. New insights into the surface relaxation and oxidation of chalcopyrite exposed to $O_2$ and $H_2O$: A first-principles DFT study. *Applied Surface Science* 2019, 492: 89-98.

54. Cai R, Kubota Y, Fujishima A. Effect of copper ions on the formation of hydrogen peroxide from photocatalytic titanium dioxide particles. *Journal of Catalysis* 2003, 219(1): 214-218.

55. Luther GW. The Role of One- and Two-Electron Transfer Reactions in Forming Thermodynamically Unstable Intermediates as Barriers in Multi-Electron Redox Reactions. *Aquatic Geochemistry* 2010, 16(3): 395-420.

56. Borda MJ, Elsetinow AR, Strongin DR, Schoonen MA. A mechanism for the production of hydroxyl radical at surface defect sites on pyrite. *Geochimica et Cosmochimica Acta* 2003, 67(5): 935-939.

57. Zhang P, Yuan S, Liao P. Mechanisms of hydroxyl radical production from abiotic oxidation of pyrite under acidic conditions. *Geochimica et Cosmochimica Acta* 2016, 172: 444-457.

58. Usher CR, Paul KW, Narayansamy J, Kubicki JD, Sparks DL, Schoonen MAA, Strongin DR. Mechanistic Aspects of Pyrite Oxidation in an Oxidizing Gaseous Environment: An in Situ HATR−IR Isotope Study. *Environmental Science & Technology* 2005, 39(19): 7576-7584.

# Chapter 7 Conclusions and Future Directions

Nanoparticles, NPs, especially metal oxides and metal sulfides have attracted a great deal of interest for their properties and broad applications. NPs have a unique advantage over larger particles, namely high surface area, surface tension and unique properties due to quantum confinement. These make properties of NPs highly dependent on their surface states, including surface ligands, surface redox processes, surface defects etc.

Furthermore, NPs highly reactive surfaces are involved in surface ligand reaction, ROS generation, surface relaxation and surface redox. These surface chemical processes have a big impact on the behavior of NPs. Therefore, surface transformations have become crucial to the understanding of NPs and their physiochemical properties, including dissolution, reactivity, aggregation and even toxicity. With increased usage, significant amounts of NPs from research and industry have been released into the environment. Once these NPs are released into the environment, they can undergo aging and surface transformation in complex conditions. This dissertation has focused on understanding the molecular level details of surface transformations for two common NPs, titanium dioxide and copper sulfide, under environmentally and biologically relevant conditions and the potential consequences of these transformations on the environment. Furthermore, the principles learned from ligand reactions on $TiO_2$ NPs were successfully used to explain the effect of humic substances on crude oil cleanup with magnetic NPs. This dissertation focused on several scientific questions: *What are the details of the mechanisms for environmentally and biologically relevant ligand reactions on stable oxide nanomaterials at the molecular level?; What impacts do these reactions have on the behaviors of nanoparticles in terms of reactivity and performance in environmental applications? and; How do metal sulfide nanoparticles oxidize in the environment and what environmental factor(s) (such as humidity) significantly contribute to*

*the oxidation?*. These were addressed through four specific projects to understand surface transformations of NPs as described in the chapter summaries below.

## 7.1 Chapter 3 Summary

This chapter focused on ligand reactions on $TiO_2$ NPs including adsorption, desorption and displacement. Ligand reaction experiments included a wide variety of techniques: BET, PXRD, UV-VIS spectrometry, ATR–FTIR, TEM, SEM, dynamic light scattering and QCM-D. The crystalline phase of the $TiO_2$ NPs (P25) was confirmed using PXRD: a mixture of anatase (80%), rutile (13%) and amorphous (7%). The ligand reactions were investigated using ATR–FTIR by flowing the chosen ligand solutions over $TiO_2$ NP films. Among the chosen ligands, ascorbic acid (AA) shows the weakest interaction with $TiO_2$ NPs with reversible adsorption. Citric acid (CA) shows partially reversible adsorption with stronger affinity than AA. Humic acid (HA) and bovine serum albumin (BSA), macromolecules, strongly adsorb on $TiO_2$ NPs resulting in irreversible adsorption. Further study about the displacement between HA and the other three ligands indicates that HA could displace the smaller molecules (AA and CA) and form a coating. On BSA-coated surfaces, co-adsorption of HA occurrs, rather than displacement. This was observed by ATR–FTIR and these spectroscopic results were corroborated by QCM-D. Furthermore, QCM-D results also demonstrates that HA co-adsorbs with BSA by strong intermolecular interactions. Interestingly, HA changes its conformation during the adsorption process, reflected in the continuous increase of the dissipation. The data provided by 2DCOS reflects the sequence of the functional groups involved in the displacement processes. The outersphere complex was thought to be the first stage of displacement: HA interacts with coated molecules first by weak interaction e.g. H-bonding. Next, HA occupies the active sites on the surface by replacing pre-adsorbed molecules. After either displacement or co-adsorption, the newly formed coating layers alter the aggregation and

sedimentation behavior of $TiO_2$ NPs. HA largely enhances the stability of $TiO_2$ NPs suspended in solution, which is important to the transportation of $TiO_2$ NPs released to the environment. This research provides insights to the fate $TiO_2$ NPs with coatings in the environment.

## 7.2 Chapter 4 Summary

This chapter focused on understanding how humic substances influence crude oil adsorption on magnetite NPs which are used for crude oil cleanup in sea water. Coupling of molecular dynamics (MD) simulations and experimental data using ATR–FTIR spectroscopy allowed for better understanding of these processes. The magnetite NPs used were first coated by polyvinylpyrrolidone (PVP) molecules that were used in the synthesis of the NPs. PVP molecules interact with the magnetite surface with an average binding strength of –9.2 kcal/mol, the energy of which matches the Van der Waals interaction. The time dependent ATR–FTIR spectra showed that signal intensity of the PVP coating on the NPs decayed over time, indicating the loss of PVP from the surface. Combining MD simulation and spectroscopy, PVP is thought to weakly interact with surface Fe ions mainly through its carbonyl (C=O) functional groups, resulting in physical adsorption. Furthermore, the MD results indicate that crude oil favorably adsorbs onto PVP-coated magnetic NPs with an adsorption free energy of –3.6 kcal/mol. Interestingly, this adsorption is inhibited to some degree in the presence of fulvic acid (FA), which is attributed to the ability of FA molecules to displace PVP in seawater and form a new coating layer on the surface of the NPs. The displacement ATR–FTIR results suggest FA has a stronger adsorption affinity than PVP and is able to displace PVP from the surface. As a result, under such conditions, FA shows irreversible adsorption. This work provides implications of molecular interactions and environmental conditions on the adsorption of crude oil on NPs, which is crucial for the design of nano-based oil remediation.

## 7.3 Chapter 5 Summary

This chapter focuses on how ligands affect $TiO_2$ nanoparticle reactivity. Ligand adsorption on $TiO_2$ NPs can affect not only their sedimentation behavior but also reactivity. The reactivity of $TiO_2$ NPs is mainly reflected by the generation of ROS, which also cause toxicity towards organisms. Two different ligands of biological and environmental significance, BSA and FA, were chosen to study the effects of ligands on the generation of ROS under irradiation. Benzoic acid was used to detect a highly reactive ROS—hydroxyl radicals. The mass spectrometry results indicate that benzoic acid is oxidized by hydroxyl radicals forming hydroxybenzoic acid, dihydroxybenzoic acid and trihydroxybenzoic acid. Interestingly, the decarboxylation product, phenol, was observed by MS. Bare $TiO_2$ shows a high yield of these products, whereas it is hard to detect the oxidized products from BSA-coated $TiO_2$. The ability for ROS generation on $TiO_2$ NPs with different coatings follows this sequence: bare $TiO_2$ > FA-$TiO_2$ > BSA-$TiO_2$. Photoirradiation ATR–FTIR was used to further investigate the mechanisms. Bare $TiO_2$ NPs in water under irradiation exhibits broad ROS IR features such as peroxide and superoxide. In addition, IR results also corroborated photoinduced hydrophilicity of $TiO_2$, as reported previously, showing an increased water bending peak with time. Under irradiation, spectra of BSA on the $TiO_2$ film exhibit a new peak at high vibrational frequency (~1760 $cm^{-1}$) in addition to IR features of BSA, but no ROS were observed. In contrast, the ROS IR features appear on FA-coated $TiO_2$ NPs. These results suggest that BSA has a strong capability to quench reactive intermediates, but FA can only inhibit ROS generation to some degree. Thus, understanding surface composition and its role in $TiO_2$ reactivity is needed to predict the behavior of $TiO_2$ in environmental and biological systems. Overall reactivity is suppressed but depending on the details of the ligands adsorbed that suppression can be complete or partial in nature.

## 7.4 Chapter 6 Summary

The properties of CuS NPs especially LSPR are highly dependent on its surface states. As such, it is crucial to understand surface transformations, including surface oxidation, of these nanomaterials and their impact on the physiochemical properties in the environment. This chapter focused on understanding of the effects of environmental condition (i.e. relative humidity, RH) on surface transformation process of Cu NPs. This study was carried out in a gas flow ATR–FTIR system by controlling the humid gas flow. The oxidation of sulfide ions to sulfate by oxygen shows a very close relationship with water vapor and adsorbed water. The *in-situ* ATR–FTIR results suggest at high RH, sulfide ions can rapidly convert to sulfate by oxygen, whereas this process cannot occur in the absence of water. Surface transformation was further studied by XPS. The vibrational spectroscopy results were further confirmed by XPS: sulfide is oxidized to sulfate. Interestingly, Cu ions still possess the original oxidation state as the original covellite at ambient RH (~ 40%) but convert to $Cu^{2+}$ at high RH (87%). ROS, as intermediates, are proposed to be involved in the oxidation process, in which water catalyzes the conversion of copper from $Cu^{+}$ to $Cu^{2+}$. Oxygen acts in this process as a final electron acceptor. Meanwhile, water undergoes surface chemistry resulting in the formation of hydroxyl radicals which enhance oxidation processes. Most interesting is the fact that water can also serve as a medium to promote dissolution of CuS. The formation of the final product, $CuSO_4$, after oxidation was observed by microscopic methods including HR-TEM and AFM-IR. This study provided insights about surface transformations of sulfide NPs in different humid environments when released to the environment. Furthermore, the findings also implied stability of sulfide NPs used as device components when exposed to the atmosphere, containing water and oxygen. Moreover, as a proposed mechanism, the

transformation may enhance toxicity not only caused by releasing $Cu^{2+}$ ions but by the formation of ROS.

## 7.5 Future Directions

The transformation of NP surfaces is exceedingly complicated as it is influenced by many environmental factors. The transformation in turn reshapes physiochemical properties of NPs including reactivity, stability, and toxicity. As such, studies about surface changes have become highly significant for the application and safety of NPs. The research in this dissertation presented both insights of how NPs behave in the environment and implications for safety of NPs in applications. However, some areas remain unknown or speculative, and need further study in order to get a more comprehensive understanding about the fate of NPs when released into the environment:

1. In the ligand displacement reactions, conditions were controlled at pH 7.5. However, environmental conditions are more complex than the ones used in the experiment. Environmental factors such as ionic strength and pH should be considered in ligand displacement reactions. Additional work related to the stability and transportation of NPs caused by ligand reactions should be conducted in order to assess the fate of NPs in the environment under these further conditions.
2. Theoretical simulation work will be needed to support the assumption that ROS intermediates are generated in surface transformations. Along with theoretical simulation, electron paramagnetic resonance (EPR) can also be used to explicitly analyze ROS formation.
3. Studies related to toxicity induced by NP surface transformations are needed to evaluate the potential negative effects on human health and the environment. Dissolution

experiments are supposed to provide more information of toxicity induced by surface transformations. Additionally, *In vivo* studies under similar conditions are also recommended to fulfill the goals.

In conclusion, the research presented here provided important insights into the behaviors of NPs caused by interface changes and the effects of different factors on the physiochemical properties of NPs. The future directions of this work will greatly expand understanding of the impact surface transformations on NPs and how these alterations in turn influence the environment, biological systems, and human health.

Appendix A Supporting Information for "Displacement Reactions Between Environmentally and Biologically Relevant Ligands on $TiO_2$ Nanoparticles: Insights into the Aging of Nanoparticles in the Environment"

## A.1 Experimental Details and Additional Experimental Data

*Reagents and Sample Preparation.* $TiO_2$ nanoparticles (vendor reported size 21nm, ≥99.5%) were purchased from Aldrich. Solutions of citric acid, (CA, ≥99.5%, Sigma-Aldrich), ascorbic acid (AA, ACS grade, VWR), humic acid (HA, technical grade, Sigma-Aldrich), and bovine serum albumin (BSA, ≥ 98%, Sigma-Aldrich) were prepared with 25 mM 4-(2-hydroxyethyl)-1-piperazineethanesulfonic acid (HEPES, Fisher Scientific) to maintain a stable pH. Sodium hydroxide (NaOH, 1N; Fisher Scientific;) and hydrochloric acid (HCl, 1N; Fisher Scientific) were used to adjust pH to 7.5. The ionic strength was maintained by sodium chloride (NaCl, Fisher Scientific). All the solutions were made in Milli-Q water.

*Nanoparticle Characterization.* The crystallinity of $TiO_2$ NPs was determined by Powder X-ray diffraction running at 40 kV, 4 mA for Cu Kα (λ = 1.5418 Å) (Bruker D8 Advance diffractometer). The morphology and size of nanoparticles were characterized by transmission electron microscope (FEI Tecnai G2 Sphera TEM) operating at 200 kV shown in Figure A1.

Additionally, scanning electron microscope (Zeiss Sigma 500 SEM) is employed to show the profile of a thin film of $TiO_2$ nanoparticles shown in Figure A2.

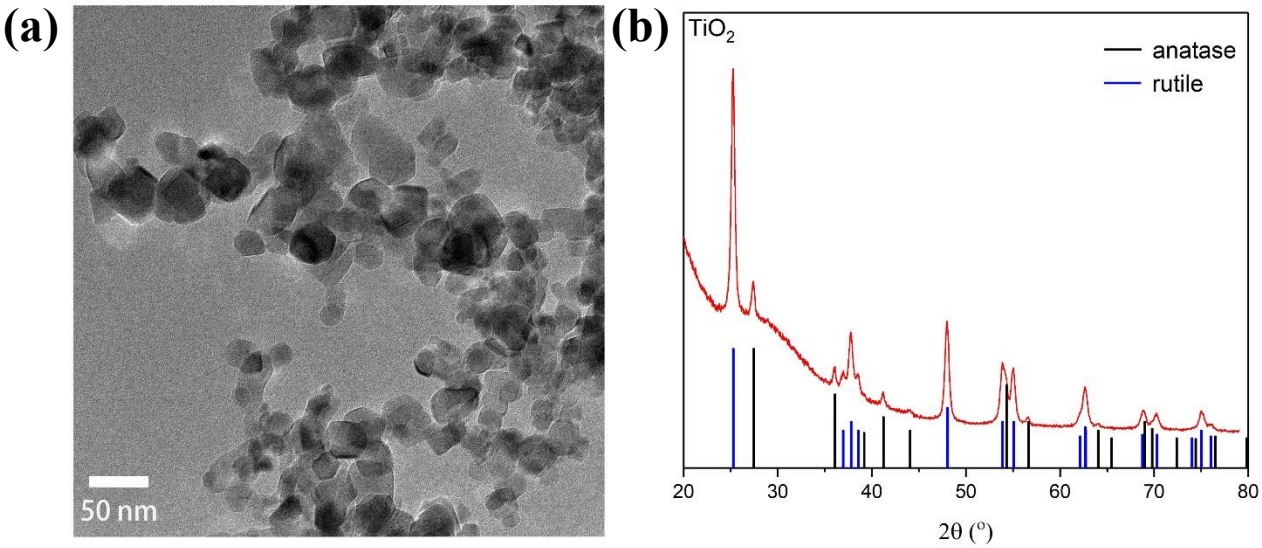


**Figure A1.** Characterization of $TiO_2$ NPs powder. (a) The TEM image shows the morphology of $TiO_2$ NPs. (b) The X-ray diffractogram shows that rutile and anatase crystalline phases are present in the of $TiO_2$ NPs. The blue and black lines represent the diffraction pattern of rutile (PDF#21-1276) and anatase (PDF#21-1272), respectively.

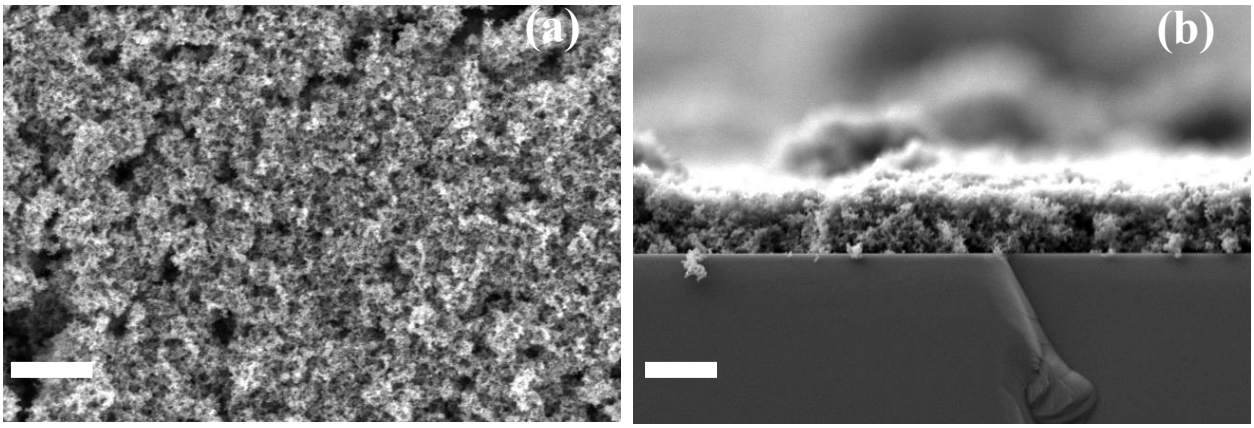


**Figure A2.** SEM images of $TiO_2$ nanoparticles on Si wafer, (a) top view; (b) side view. The scale bars shown in the images are 1 μm.

*Analysis of 2DCOS.* Two-dimensional correlation spectroscopy (2D-COS) was used to analyze the displacement reactions of CA-, AA- and BSA-coated $TiO_2$ NPs with HA. In this work, the time after introducing humic acid was used as the external perturbation for the structural changes of HA and its complexation on $TiO_2$ nanoparticles surfaces during the displacement process. Based on Noda and Ozaki's work,[192] the variation in a discrete set of dynamic spectra is represented by

$$\tilde{\boldsymbol{y}}(\boldsymbol{v},\boldsymbol{t}) = \begin{cases} \boldsymbol{y}(\boldsymbol{v},\boldsymbol{t}) - \bar{\boldsymbol{y}}(\boldsymbol{v}), & \boldsymbol{T_{min}} \leq \boldsymbol{t} \leq \boldsymbol{T_{max}} \\ \mathbf{0}, & \boldsymbol{others} \end{cases}$$

where $\boldsymbol{v}$ is the spectral variable (wavenumber in FTIR spectra); t is a perturbation variable. $\bar{\boldsymbol{y}}(\boldsymbol{v})$ is the time-averaged reference spectrum. The synchronous (Φ) and asynchronous (Ψ) 2D correlation spectral maps can be calculated from discrete dynamic spectra by

$$\tilde{\boldsymbol{y}}\,(\boldsymbol{v}) = \begin{bmatrix} \boldsymbol{y}\,(\boldsymbol{v},\boldsymbol{t_1}) \\ \boldsymbol{y}\,(\boldsymbol{v},\boldsymbol{t_2}) \\ \vdots \\ \boldsymbol{y}\,(\boldsymbol{v},\boldsymbol{t_m}) \end{bmatrix} \qquad (2)$$

$$\boldsymbol{\Phi}(\boldsymbol{v_1},\boldsymbol{v_2}) = \frac{\mathbf{1}}{\boldsymbol{m}-\mathbf{1}}\tilde{\boldsymbol{y}}(\boldsymbol{v_1})^{\mathrm{T}}\tilde{\boldsymbol{y}}(\boldsymbol{v_2}) \qquad (3)$$

$$\boldsymbol{\Psi}(\boldsymbol{v_1},\boldsymbol{v_2}) = \frac{\mathbf{1}}{\boldsymbol{m}-\mathbf{1}}\tilde{\boldsymbol{y}}(\boldsymbol{v_1})^{\mathrm{T}}\boldsymbol{N}\tilde{\boldsymbol{y}}(\boldsymbol{v_2}) \qquad (4)$$

where m is equally spaced point in t between $T_{min}$ and $T_{max}$, and the Hilbert- Noda transformation matrix (N) is given by

$$\mathrm{N}=\frac{\mathbf{1}}{\boldsymbol{\pi}}\begin{bmatrix} 0 & 1 & \frac{1}{2} & \frac{1}{3} & \cdots \\ -1 & 0 & 1 & \frac{1}{2} & \cdots \\ -\frac{1}{2} & -1 & 0 & 1 & \cdots \\ -\frac{1}{3} & -\frac{1}{2} & -1 & 0 & \cdots \\ \cdots & \cdots & \cdots & \cdots & \cdots \end{bmatrix} \qquad (5)$$

*QCM $TiO_2$ Characterization.* X-ray photoelectron spectroscopy confirms a Ti (IV) oxide and the presence shoulder with a binding energy around 532eV in Figure A3b indicates that the $TiO_2$ surface on the sensor is partially hydroxylated.

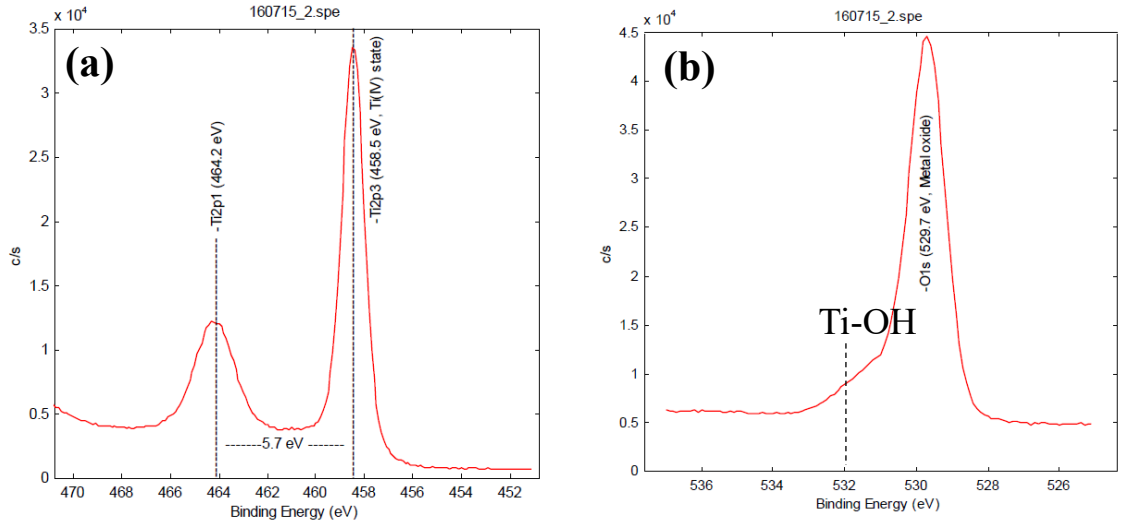


**Figure A3.** Binding energy of $TiO_2$ sensor. (a) high resolution scan in Ti 2p region of the sample, (b) high resolution scan in O 1s region of the sample.

*QCM Overtones.* Frequency and dissipation changes following BSA adsorption and subsequent.

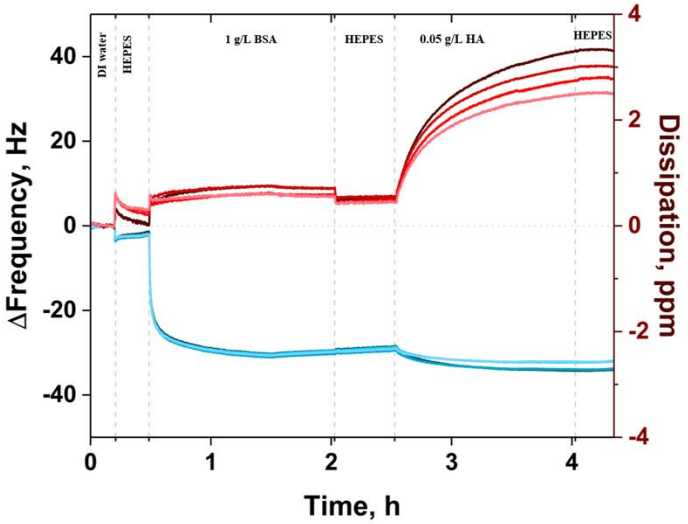


**Figure A4.** Shifts in frequency and dissipation for the displacement process of BSA by HA onto a $TiO_2$ coated surface with QCM–D. Blue and red lines represents changes in frequency and dissipation, respectively. Data are shown for overtones 5,7, 9, and 11.

*Additional Displacement Studies.* In these experiments, HA adsorption was followed by AA, or CA or BSA. FTIR spectra are shown in Figure A5 and a proposed mechanism is shown in Figure A6.

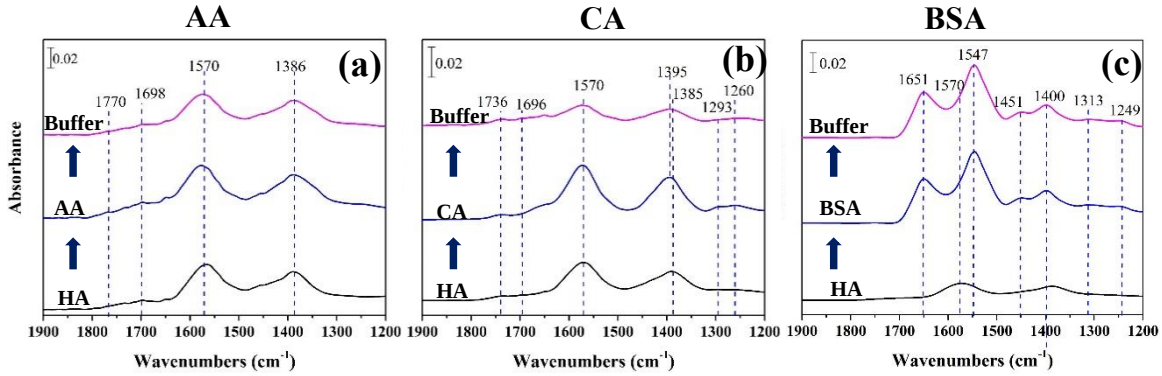


**Figure A5.** Displacement reactions on HA pre-coated $TiO_2$ NPs through ATR-FTIR by AA (a), CA (b), and BSA (c).

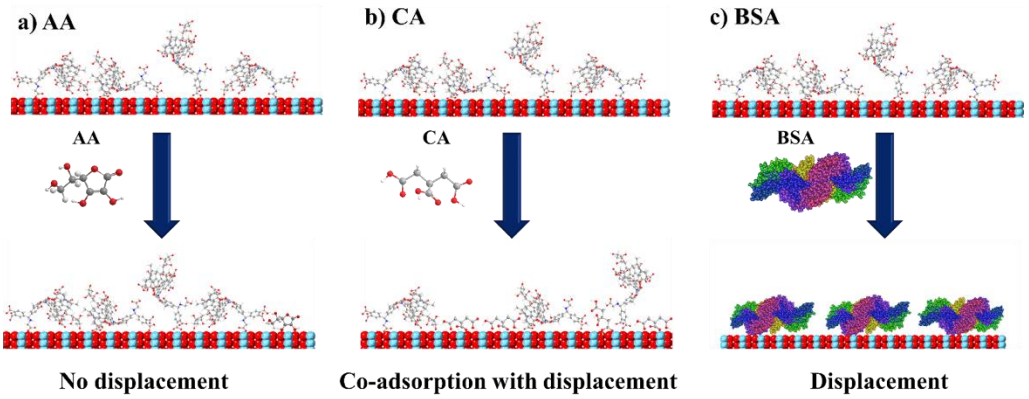


Figure **A6**. A schematic representation of displacement reactions of HA pre-coated $TiO_2$ surface by AA (a), CA (b), and BSA (c), respectively. HA is represented here as a macromolecular structure.

A.2 References

1. I. Noda and Y. Ozaki, in *Two-Dimensional Correlation Spectroscopy – Applications in Vibrational and Optical Spectroscopy*, John Wiley & Sons, Ltd, 2005, DOI: 10.1002/0470012404.ch3, pp. 39-46.

A.3 Acknowledgements

Appendix A is in full reproduced with adoption with permission from Royal Chemical Society: Haibin Wu, Natalia I Gonzalez-Pech, Vicki H Grassian. “Displacement reactions between environmentally and biologically relevant ligands on $TiO_2$ nanoparticles: insights into the aging of nanoparticles in the environment” Environmental Science: Nano, vol 6, 2019. The dissertation author was the primary investigator and first author of this paper.

Appendix B Supporting Information for "Mechanistic study of oil adsorption onto PVP-coated magnetic nanoparticles: An integrated experimental and molecular dynamics study to inform remediation"

B.1 Additional Experimental Data

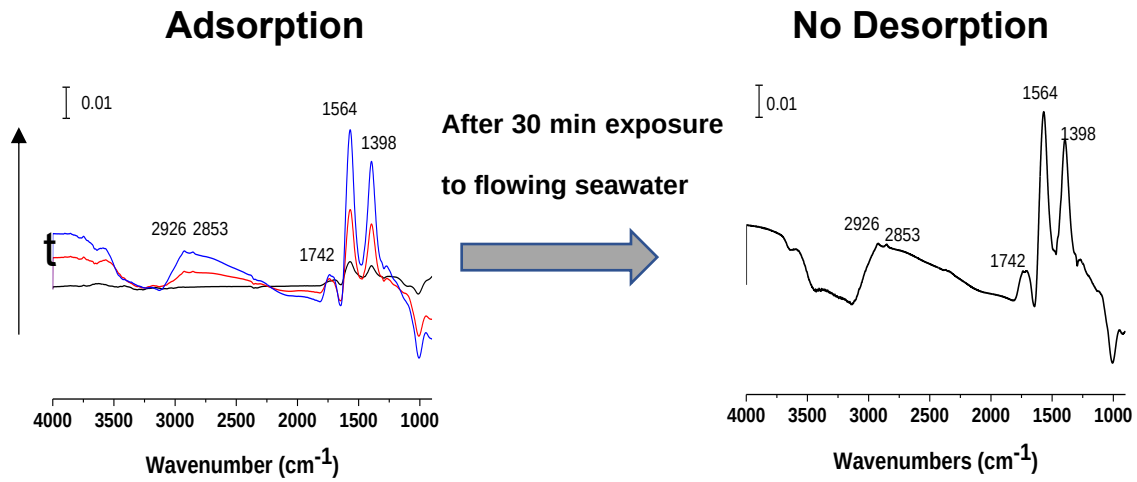


**Figure B1**. ATR-FTIR spectra of sequentially introducing different solutions. NPs for adsorption (a) flowing 10ppm FA, (b) flowing sea water. the black, red and blue lines represent 15 90 and 120 min, respectively.

B.2 Acknowledgements

Appendix B, in full, has been submitted for publication of the material as it may appear in Nature Nanotechnology, 2020, Linkel K. Boateng, Seyyedali Mirshahghassemi, Haibin Wu, Vicki H. Grassian, Joseph R.V. Flora, Jamie R. Lead. The dissertation author was the investigator and author of this paper. The dissertation author conducted the spectroscopic measurements and analysis. Dr. Linkel Boateng and Dr. Flora conducted the computational simulations. Dr. Seyyedali Mirshahghassemi provided the magnetite NPs for the research. I also acknowledge U of SC Research Cyberinfrastructure for the computational time used for the research.

Appendix C Supporting Information for "Surface Adsorbed Biologically and Environmentally Relevant Ligands on $TiO_2$ Nanoparticles Transformations: The Influence on Reactivity of Nanoparticles"

## C.1 Additional Experimental Data

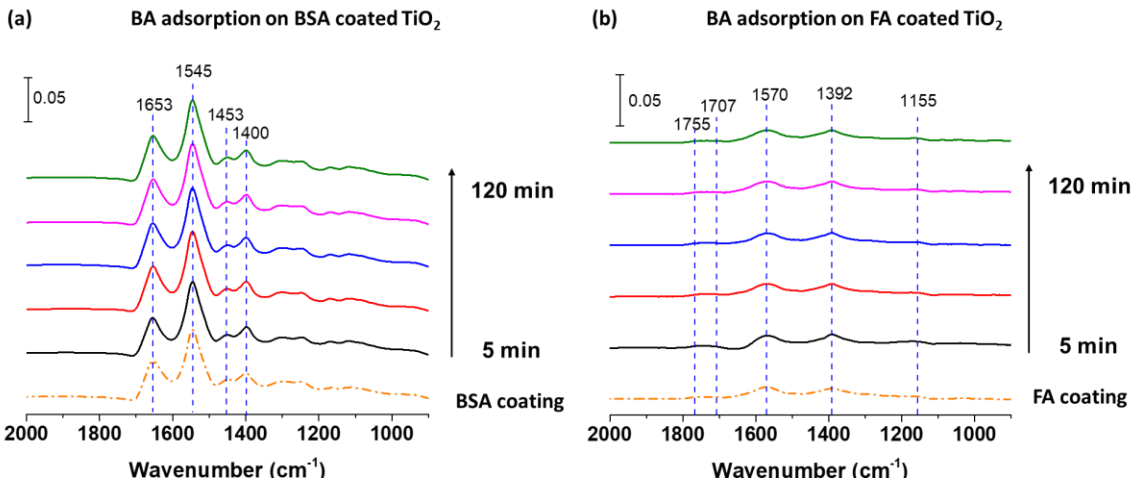


**Figure C1.** *In-situ* ATR-FTIR spectra of BA adsorption on coated $TiO_2$ NPs, (a) BSA coated $TiO_2$, (b) FA coated $TiO_2$. The spectra shown were collected at 5 min (black), 30 min (red), 60 min (blue), 90 (magenta), 120 min (green) and the orange dash line represent coating molecules only on $TiO_2$ NPs.

## C.2 Acknowledgements

Appendix C, in full, has been submitted for publication of the material as it may appear in Enviromental Science: Nano, 2020.